The Dissertation Committee for Amir Toliyat certifies that this is the approved version of the following dissertation:

ENERGY STORAGE SIZING FOR LOW-INERTIA MICROGRIDS, AND LESSONS LEARNED FROM A POTENTIAL MICROGRID

Committee:

Ross Baldick, Supervisor

Alexis Kwasinski, Co-Supervisor

Gary Hallock

Aristotle Arapostathis

Fabian Uriarte

ENERGY STORAGE SIZING FOR LOW-INERTIA MICROGRIDS, AND LESSONS LEARNED FROM A POTENTIAL MICROGRID

by

Amir Toliyat, B.S.; M.S.E

Dissertation

Presented to the Faculty of the Graduate School of

The University of Texas at Austin

in Partial Fulfillment

of the Requirements

for the Degree of

Doctor of Philosophy

The University of Texas at Austin

May 2016

Dedication

To my parents, Hamid and Mina, for their love and support

Acknowledgements

I would like to thank my supervisor, Dr. Alexis Kwasinski, for his encouragement, guidance, and understanding throughout my time as a graduate student. Since accepting me as his student in fall 2009, he has offered me his full support and unwavering patience. I am very fortunate to have worked on the projects he assigned me. Despite his departure from The University of Texas (UT), Dr. Kwasinski—now at The University of Pittsburgh—has remained loyal to his UT students by maintaining communication and often traveling between Pittsburgh and Austin to meet with them. This is a testament to his professionalism and sound character, and I am blessed to have been supervised by him.

I would also like to thank my doctoral committee members Dr. Aristotle Arapostathis, Dr. Ross Baldick, Dr. Gary Hallock, and Dr. Fabian Uriarte for their valuable advice and feedback.

My lab-mates and colleagues are also acknowledged for providing thought-provoking discussions and contributing to a pleasant experience: Seunghyun Chun, Vaidyanathan Krishnamurthy, Chimaobi Onwuchekwa, Sungwoo Bae, Seunghoon Choung, Harsha Kumar, Junseok Song, Ruichen Zhao, Sheng Yang Yu, Juyoung Jung, Hunter Estes, Myungchin Kim, Mahesh Srinivasan, Joonhyun Kim, Youngsung Kwon, Rossen Tzartzev, Greg Dahlberg, Sahil Shanghavi, Alex Sitzman, and Dave Tuttle.

I am very appreciative of the United States Department of Energy and Pecan Street Inc. for supporting my research.

I extend my gratitude to the engineers at Chevron ETC, namely Roy Hamilton, Kurt Concienne, Eric Glaude, Tim Nguyen, and Masoud Haji for giving me the

opportunity to intern with the MEPS team in the summer of 2011. The memorable experiences I had there not only helped me learn about the industry, but also made me realize my own abilities by igniting a self-confidence I had not previously possessed.

I would like to recognize Dr. Fabian Uriarte for his mentorship, particularly during the time I spent at Center for Electromechanics. The collaborations we had regarding the Pecan Street Project, as well as the many discussions about microgrids, software learning, and other topics were very rewarding and helped me become a better researcher.

I am grateful of my mother, Mina, and my father, Hamid, for believing in me and always encouraging me to be the best I can be. My parents have endured great hardship and made a lot of sacrifices for me to have a better future, and I can never thank them enough. They are the best role models I could ask for, and my appreciation for them is boundless. My brother, Mohammad, is also acknowledged and deserves much praise. Despite being the younger brother, he has been able to teach me a lot, and I am extremely proud of him for what he has been able to accomplish in medical school. My wife, Parisa, deserves my sincere gratitude for loving me endlessly and for motivating me to reach my full potential. She empowers me to achieve anything I want and has brought so much joy into my life. Marrying her was the best decision I have ever made.

ENERGY STORAGE SIZING FOR LOW-INERTIA MICROGRIDS, AND LESSONS LEARNED FROM A POTENTIAL MICROGRID

Amir Toliyat, Ph.D.

The University of Texas at Austin, 2016

Supervisor: Ross Baldick

Co-Supervisor: Alexis Kwasinski

The coordinated control of multiple distributed generators in a microgrid and the preservation of adequate system inertia in real-time operations are some of the principal technical challenges for stable microgrid operation. One issue in particular pertains to grid-tied inverters, which, as mandated by present standards, are only permitted to operate at unity power factor, thereby requiring the microgrid's synchronous generators to operate at a low power factor. This behavior accordingly introduces ramifications by limiting the generator's active power output, which would compromise frequency and voltage stability margins.

Consideration is also given to the effect of line impedances, since interconnecting microgrid lines can be described by a variety of X/R ratios that affect the control and flow of active and reactive power. Moreover, the absence of a stiff grid presents control challenges for grid-tied inverters due to the inverters' tendency to regulate the voltage at the point of common coupling.

These same inverters also jeopardize microgrid stability due to their low equivalent inertia as traditional forms of generation (i.e., spinning sources) become

displaced by inertia-less inverters. Because of this low microgrid inertia, fluctuations in the output power of renewable energy sources or changes in local load levels may lead to power quality or frequency/voltage stability concerns. Therefore, energy storage sizing is investigated in this dissertation, as it is closely related to the stability analysis of microgrids.

Furthermore, an existing residential community (in Austin, TX) described by a moderate penetration of photovoltaic sources and electric vehicle charging is considered, and the implications of said community being retrofitted to a microgrid are examined.

Table of Contents

List of Tables

List of Figures

Chapter 1: Introduction

MOTIVATION

When uncomfortable living conditions and billions of dollars in lost business activity are the expected consequences of any sustained power outage, the need for a robust and reliable electrical system becomes increasingly important. The growing emphasis on reliable electric power, cost reduction, and lower carbon emissions has given rise to new ideas and technologies for realizing a more resilient and energy efficient power system.

Dependence on an aging, centralized power system—one in which energy is distributed inefficiently and demand is often not met—has persisted for decades despite well-documented instances [1-4] of its debilitating effects. In the wake of natural and unnatural causes, the vulnerability of the traditional electrical system has increased the urgency of a transition toward more intelligent systems. Crippling economic impacts to businesses (through lost orders and damages to perishable goods) and manufacturers (through downtime, lost production, and equipment damage) make the present-day electrical grid a liability. Naturally, a solution would aim to reduce the dependence on electrical transmission lines that carry bulk power long distances and instead rely on local power generation.

Distributed Generation

Distributed local generation—the generation of electricity from small energy sources geographically apart—provides an alternative to the traditional electric power system and allows for a less centralized means of meeting energy demands. Although some of the enabling technologies are relatively new, the concept itself dates back to the initial phase (circa 1880) of the electric power industry when all energy requirements

were supplied at or near their point of use. During the early days of electricity generation—given that the first power plants only supplied electricity to customers in close proximity of the generation plant—distributed generation was the rule rather than the exception. It was not until later (early 20th century), that the emergence of ac grids enabled long-distance transmission of electricity as well as an increase in the power output of generation units due to economies of scale.

Within the last decade or so, a renewed interest for distributed generation has been set in motion, primarily as a result of five major factors [5]: developments in distributed generation technologies, constraints on the construction of new transmission lines, increased customer demand for highly reliable electricity, the electricity market liberalization, and concerns about climate change. The exponential growth of wind turbine and photovoltaic (PV) usage, together with energy storage options such as batteries, has contributed greatly to this cause while mitigating adverse environmental consequences.

In contrast to generating power centrally, on-site generation via distributed energy resources eliminates interdependencies, inefficiencies, and costs associated with transmission and distribution. According to a report by the Electric Power Research Institute, the U.S. economy loses between $104 billion and $164 billion a year to power outages, and another $15 billion to $24 billion to power quality phenomena [6]. Furthermore, as a result of aging transmission equipment, inconsistent enforcement of reliability guidelines, and growing congestion, roughly 4.2% to 8.9% of electricity is wasted as it is transmitted from a power plant to a typical user [7]. Because the cost of this vast transmission grid is included in customers' electricity bills, the use of on-site power can provide consumers with affordable power and at a higher level of quality.

Another desirable attribute of local power generation is the ability to sell surplus power to the grid, thus yielding income during times of peak demand. The aforementioned disadvantages of the traditional centralized grid and the potential benefits of distributed generation have stimulated the need for user-controlled local electricity grids.

Microgrids

The ultimate end of distributed generation is the establishment of localized grids of electricity known as microgrids. According to the Department of Energy, a microgrid is formally defined as "a group of interconnected loads and distributed energy resources with clearly defined electrical boundaries that acts as a single controllable entity with respect to the grid and can connect and disconnect from the grid to enable it to operate in both grid-connected or island mode."

Microgrids have been prescribed as a solution to increase power supply availability and ensure that critical loads are served during extended outages [8]. An increasing trend toward microgrid adoption has been evidenced in military applications where operation of critical facilities must be sustained regardless of grid outages. Unpredictable access to fuel transportation routes, particularly in the theater of war, further advocates the need to integrate renewable energy sources within the microgrid.

Covering over 100 square miles, the Fort Bragg U.S. Army base in North Carolina hosts one of the largest microgrids in the world. This facility's utility infrastructure works in conjunction with a variety of distributed generation technologies to achieve energy security and reduce overall energy costs. Besides reducing peak demand consumption, Fort Bragg operates on a time-of-use tariff [9], electing to self-

generate when market prices exceed a predetermined threshold. This results in monetary savings when the cost of self-generation is lower than the cost of grid-supplied power.

Another notable microgrid, located at the Illinois Institute of Technology (IIT) main campus, has proven its effectiveness by reducing peak load by 20% [10], eliminating costly outages, minimizing power disturbances, and curbing greenhouse gas emissions. University officials estimate that IIT's microgrid will lead to annual savings of $1 million as a result of forgone costs associated with restoration expenses, lost productivity, and ruined experiments that often cannot be recovered.

The threat of extreme weather events has also stimulated great interest in microgrids [11-14]. In the aftermath of the 2011 Great East Japan Earthquake, a 9.0-magnitude earthquake which inflicted catastrophic damage on the energy supply system for a number of days, the Sendai Microgrid demonstrated its effectiveness by continuing to supply power and heat to customers as it operated in islanded mode. Within a matter of seconds after the earthquake, a series of major voltage fluctuations were present in the main grid, causing a gradual drop in voltage and, ultimately, leading to the outage. Accordingly, the Sendai Microgrid switched to island mode and continuously fed power to customers. Once all microgrid equipment for two-way power flow with the grid was checked and readied for interconnection, the microgrid was reconnected to the utility grid and returned to its normal operating mode [15].

By demonstrating its effectiveness in supplying continuous power, the microgrid saved many lives. Fatal accidents did not occur in the facilities that were being served by the microgrid; that is, the hospital that specialized in internal diseases and the nursing care facility that accommodated patients who relied on ventilators for life support were able to function flawlessly without incurring any loss of life. Although the need and advantages of microgrids are clear, the resistive nature of the microgrid lines, as well as

the microgrid's low rotating inertia during islanded mode, present control and stability issues that will be discussed later.

RESEARCH DESCRIPTION AND CONTRIBUTIONS

The research presented in this dissertation focuses on the operational constraints, interconnection implications, and stability considerations associated with microgrids. In addition to raising awareness about key microgrid issues, the research intends to address frequency and voltage stability challenges resulting from a combination of limited microgrid inertia and resistive line impedances. Specifically, a methodology for energy storage sizing is developed to aid with primary and secondary frequency control as well as with voltage regulation.

Additionally, this dissertation evaluates the impact of photovoltaic (PV) and electric vehicle (EV) integration on a residential community's electrical distribution system. The study uses a computer model together with real consumption and generation data obtained from the individual residences in order to assess the state of the system and to perform various power system analyses. The findings from this study are valuable in helping to understand how such neighborhoods would fare if retrofitted to a microgrid.

Chapter 2: Grid-Tied Inverters

IEEE STANDARD 1547

The technical issues associated with bidirectional flow of power from active generation and storage at the distribution level have been significant, acting as a barrier to the rapid deployment of distributed generation technologies. In addition to the design of traditional radial feeders being unaccommodating to distributed generation proliferation, the differing interconnection requirements of utilities from state to state, and sometimes within a state, have also been an impediment to this progress. Because of these obstacles, the importance of having a single document of consensus becomes easily recognizable as it prevents compliance with numerous local practices and guidelines.

The anticipated, widespread adoption of distributed generation resources has directly contributed to the establishment of IEEE Standard 1547 [16], which formulates criteria and requirements for their interconnection with electric power systems. This standard, applicable to distributed generation technologies with aggregate capacity of 10 MVA or less at the point of common coupling (PCC), provides requirements relevant to the performance, operation, testing, safety considerations, and maintenance of the interconnection. It includes general requirements, response to abnormal conditions, power quality, islanding, and test specifications and requirements for design, production, installation evaluation, commissioning, and periodic tests.

Since its approval, IEEE Standard 1547 has been generally beneficial for electrical distribution systems. As the only systems-level technical standard of uniform requirements and specifications for interconnection of distributed generation with the grid, IEEE Standard 1547 has promoted deployment of distributed generators, encouraging bidirectional flow of electric energy.

OPERATIONAL CONSTRAINTS OF SYNCHRONOUS GENERATORS

Despite IEEE Standard 1547's intended benefit of providing a uniform standard for interconnection of distributed generation resources with electric power systems, it also imposes important limitations. Specifically, this standard strictly stipulates that grid-tied inverters must not actively regulate voltage at the point of common coupling. Thus, the inverters are designed to operate at unity power factor, which means that they cannot supply reactive power. Consequently, the power factor as seen by the utility would deteriorate since customers would be reducing their active power demand while still imposing their reactance on the grid. This low power factor suggests that the utility provides a service without being paid for it. On the other hand, if PV generators were to supply local reactive power then incentives would need to be provided to the owners of those PV generators, due to costs [17] associated with reactive power supply of PV inverters.

Furthermore, the provisions set forth by IEEE Standard 1547 imply that the synchronous generators in a microgrid would be operating at a lower power factor which would compromise frequency and voltage stability, as will be demonstrated in Chapter IV. For a microgrid comprising m synchronous generators with power output $S_{g,i} = [P_{g,i} \quad Q_{g,i}]^T$, and n grid-tied inverters, the relations in (1) and (2) must be concurrently satisfied. At the system level,

$$S_{total} = \begin{bmatrix} \sum_{i=1}^{m} P_{g,i} \\ \sum_{i=1}^{m} Q_{g,i} \end{bmatrix} = \begin{bmatrix} P_L - \sum_{i=1}^{n} P_{inv,i} \\ Q_L \end{bmatrix} \tag{1}$$

and for each synchronous generator, the following must hold:

$$\begin{bmatrix} \sqrt{\frac{\rho_{rated,i}^2 \cdot Q_{g,i}^2}{1-\rho_{rated,i}^2}} \\ 0 \end{bmatrix} \leq S_{g,i} \leq \begin{bmatrix} \sqrt{S_{rated,i}^2 - Q_{g,i}^2} \\ S_{rated,i}\sqrt{1-\rho_{rated,i}{}^2} \end{bmatrix} \quad (2)$$

where subscripts *g* and *inv* denote the synchronous generators and the inverter-based sources, respectively, S_{rated} represents the rated machine size, ρ_{rated} the rated power factor of the machine, and P_L and Q_L are the active and reactive power, respectively, of the total microgrid load. It is evident that the generator's reactive power is bounded from above by the power factor, whereas its active power is bounded from above and below by the machine size and power factor, respectively.

ADVANCEMENT OF GRID CODES

It is important to note that the ability to supply [18, 19] or consume [20, 21] reactive power is well within the technical capabilities of the inverter power electronics, and all indications are that present interconnection standards in the U.S. will need to be revised in order to increase grid resilience. In fact, Germany, the world leader in installed PV capacity, has already revised its grid codes [22, 23] due to concerns about frequency regulation and voltage rise. The new grid codes, adopted in 2011, require PV systems to be capable of frequency-dependent active power manipulation during abnormal grid conditions as well as reactive power provision during normal grid conditions [24]. The benefits resulting from the new German grid codes have been significant and will certainly act as a precedent in the evolution of upcoming standards.

Frequency Regulation

Prior to 2011, German grid codes pertaining to frequency regulation required PV inverters connected to the low-voltage grid to automatically disconnect active power

output within 200 milliseconds when network frequency deviated from the normal operational range of 47.5-50.2 Hz [24]. However, if such a shutdown were to occur during high power feed-in from numerous PV systems, it could result in sudden, extreme power variation that would inhibit frequency stabilization. Furthermore, simultaneous reconnection of the decentralized generators in the course of a frequency recovery could elevate network frequency above 50.2 Hz, causing the generators to shut down again.

To prevent grid destabilization resulting from the immediate disconnection of generators, the new German grid code requires frequency-dependent active power manipulation by generators instead of automatic shutoff. Specifically, during over-frequency (50.2 Hz < f < 51.5 Hz) situations, generators must decrease (in the event of a rise in f) or increase (in the event of a reduction in f) their instantaneous power output P with a gradient of 40% of P per hertz. In cases of extreme over- or under-frequency ($f \geq$ 51.5 Hz or $f \leq$ 47.5 Hz), generators are required to disconnect from the grid within 100 milliseconds. If f falls below the value of 50.2 Hz again and if the possible generating power at this point in time is greater than P, the rise in the active power supplied to the network must not exceed a gradient of 10% of the maximum active power of the generator per minute [23].

Grid Voltage Support

Due to ohmic resistance along distribution lines, active power feed-in from numerous distributed PV systems can lead to supply voltage magnitudes outside the acceptable range, necessitating additional network voltage regulation by the distribution system operator to preserve power quality. To aid in the regulation of grid voltage, the new German grid code requires generators connected to the low-voltage grid to be capable of supplying reactive power to the network during normal operation [24].

The control requirements for reactive power depend on two factors [25]: 1) the installed system size and 2) the presence of a remote connection to the distribution network operator for receiving reactive power control signals. If any system with an installed capacity of less than 30 kW is *not* remotely connected to the network operator, then it must limit its active power feed-in to 70% of the maximum apparent system power S_{max} regardless of the state of the grid. If the system *is* remotely connected to the network operator, then its reactive power output corresponds to the specified power factor range as follows:

- $\boldsymbol{S_{max} < 3.68}$ **kVA** – The generator should operate with a power factor range of ±0.95.
- **3.68 kVA** $\boldsymbol{\leq S_{max} \leq}$ **13.8 kVA** – The generator will accept any set-point from the network operator within a power factor range of ±0.95.
- $\boldsymbol{S_{max} > 13.8}$ **kVA** – The generator will accept any set-point from the network operator within a power factor range of ±0.90.

Moreover, the network operator determines the reactive power control method from among three primary control methods proposed by the new low-voltage grid codes: fixed power factor, power factor characteristic, and reactive power/voltage characteristic.

With the fixed power factor method, the PV inverter operates at a constant power factor supplied by the network operator. A constant power factor, however, is not the optimal control strategy for intermittent distributed generation and is better suited for systems where the active power output is constant [25, 26].

In the power factor characteristic method, the reactive power provided depends on the active power fed in by the generator at its point of connection to the grid. This variable power factor control has important advantages. For example, network losses are reduced compared to a constant power factor, communication infrastructure is not

needed, and stability issues are nearly impossible because there is no closed-loop control. This control strategy is depicted in Fig. 1, where the power factor *PF* decreases towards 0.9 after the inverter's active power output P_{inv} reaches half of the rated active power of the inverter. The reactive power Q_{inv} supplied by the inverter can be computed from $Q_{inv} = P_{inv} \cdot \tan(\cos^{-1} PF)$.

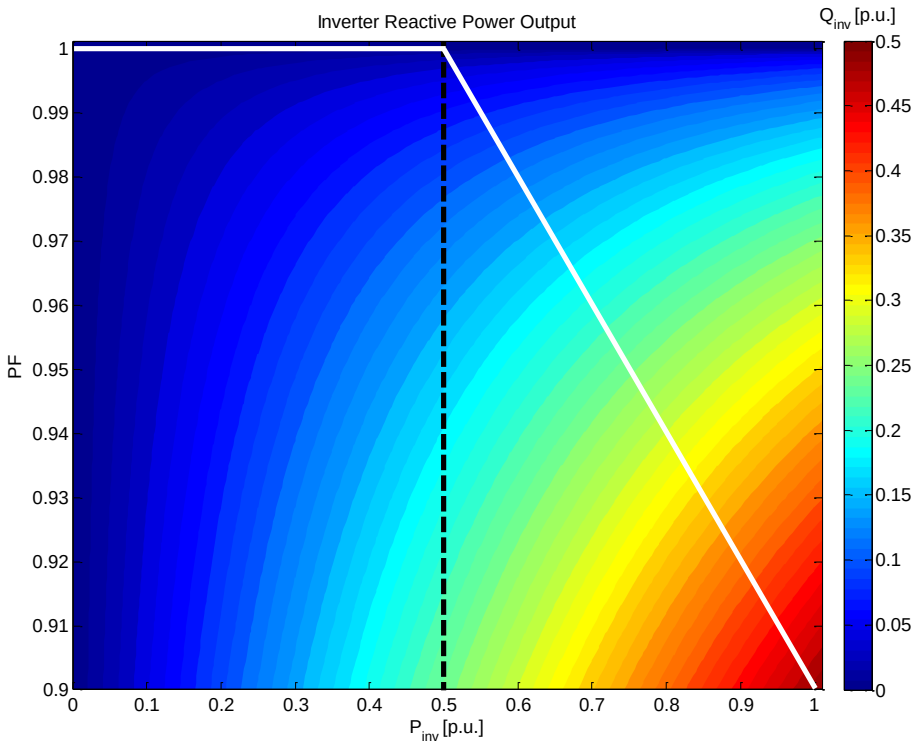

Figure 1: Power factor characteristic method with $0.9 \leq PF \leq 1$.

The reactive power/voltage characteristic method is a closed-loop strategy that relies on local voltage information in the reactive power control process. That is, the reactive power output by a generator's inverter is proportional to the voltage level at the point of interconnection. Reactive power is absorbed (negative power factor) when the

sensed voltage is too high and injected (positive power factor) when the sensed voltage is too low.

Not only are inverters able to supply and consume reactive power during regular feed-in operation, but these devices have advanced to the point where they can also provide reactive power even when feed-in operation is not in progress, e.g., at night. To appreciate the value of this, it is important to understand how German utility companies operate.

Most electric utility companies in Germany provide a free supply of reactive power up to 50% of the active power supplied by the utility. Therefore, if it is desired to install a PV plant to reduce the need to purchase electricity, then the free supply of reactive power would also be reduced even though the loads' need for reactive energy would typically not change. This means that additional costs would be incurred from having to purchase reactive power from a third party or from using a local compensation plant. However, with the inverter capable of feeding pure reactive power into the grid at night, costs associated with the external sourcing of reactive power are eliminated.

Such advancements in inverter functionality facilitate compliance to new grid codes, and allow for more flexible systems that can provide services to promote grid stability and power quality.

Chapter 3: Interconnection and Control

AUTONOMOUS CONTROL

Autonomous control methods are highly desirable for reliable microgrid operation. The lack of a master controller compels distributed energy sources to behave autonomously during transient conditions by taking local data and creating a new operating set-point that will ensure system stability. Control in microgrids is generally approached in a hierarchical manner described by three levels that serve distinct functions [27-29].

The first and most basic level, known as *primary control*, is based on the droop method. This control level is responsible for sharing the load within the electrical network, and, in so doing, ensuring its stability. The next level, aptly termed *secondary control*, restores the deviations produced by the primary control. Lastly, if the microgrid happens to be operating in grid-connected mode, the *tertiary control* manages the power flow between the microgrid and the external grid to which it is connected.

The droop control strategy, ubiquitous in large-scale power systems involving parallel-connected generators, uses locally available information to relate the change in system frequency (resp. voltage) to the active (resp. reactive) power produced by the generators. This method is employed in the *primary control* of microgrids in order to autonomously share the load among microgrid sources without needing a dedicated communications link between them [27, 30-33].

In the case of microgrids, where distributed energy sources are interfaced with a synchronous ac grid via power electronic inverters, droop-based control is often applied to the inverters in order to achieve frequency and voltage control [34-36]. A distinguishing factor between the control of islanded microgrids and that of conventional grids is that the former lacks the inertia that the latter is largely based on. In conventional

grids, when the mechanical input power and electrical output power are different, the rate of change in a generator's rotational speed is related to its rotating inertia. This means that when there is an increase in load, the demanded torque will increase without a corresponding increase in the prime mover supply torque, which translates to a decrease in rotational speed—and correspondingly—frequency.

In contrast, converter-interfaced distributed generation units prevalent in islanded microgrids have no rotating inertia coupled to the grid they serve, which implies that no coupling exists between rotational speed and grid frequency. Therefore, in the case of paralleling inverters in an islanded microgrid, the main motivation for applying the droop method is to enable the inverters to mimic the behavior of synchronous generators, where frequency (resp. voltage) reduces when the active (resp. reactive) power is increased. The active and reactive power supplied to the ac bus are sensed and averaged, and the resulting signals are used to adjust the frequency and amplitude of the inverter output-voltage reference [37]. By subtracting proportional parts of the output average active and reactive powers from the frequency and amplitude, respectively, of each module, the droop method allows for the emulation of virtual inertias [35].

LINE IMPEDANCE EFFECTS

The control of grid-tied inverters is heavily influenced by line impedance parameters and grid stiffness. The linkage between active power and frequency in the *P/f* droop, as well as the linkage between reactive power and voltage in the *Q/V* droop, are based on the power-flow characteristics of inductive lines; yet the assumption of inductive line parameters may not be valid for certain microgrids operating in both grid-connected and islanded modes. Whereas interconnecting impedances are predominantly inductive in highly dispersed networks (e.g., in utility distribution and transmission

systems), small-scale microgrids connected to low-voltage distribution networks are assumed to be mainly resistive due to the high R/X ratio in low-voltage cables. Table 1 lists typical line parameters for different cable types [38]. Additionally, the parameters specific to low-voltage cables are listed in Table 2 [39], where it can be observed that the X/R ratio varies with the size of the cable. This can be attributed to the lower geometric mean distance and higher geometric mean radius that are characteristic of bundled conductors used in microgrids.

Type of Cable	R (Ω/km)	X (Ω/km)	X/R	R/X
Low-Voltage	0.642	0.083	0.129	7.73
Medium-Voltage	0.161	0.190	1.18	0.847
High-Voltage	0.06	0.191	3.18	0.314

Table 1: Typical line impedance parameters

Voltage Class	Size	Amps	R (Ω/mile)	X (Ω/mile)	X/R	R/X
1 kV	6	75	2.5	0.185	0.07	13.51
1 kV	4	98	1.58	0.175	0.11	9.03
1 kV	2	128	0.987	0.165	0.17	5.98
1 kV	1	146	0.786	0.155	0.20	5.07
1 kV	1/0	168	0.622	0.152	0.24	4.09
1 kV	2/0	192	0.495	0.138	0.28	3.59
1 kV	3/0	219	0.392	0.134	0.34	2.93
1 kV	4/0	249	0.31	0.131	0.42	2.37

Table 2: Line impedance parameters for low-voltage cables

To observe the effect of line parameters on power-flow, the complex power $\vec{S}$ transmitted through a line with impedance $\vec{Z}$ is considered in Fig. 2, where $\overrightarrow{V_S}$ and $\overrightarrow{V_R}$ are the sending-end and receiving-end voltage phasors, respectively, and $\vec{I}$ is the current flowing through the line. The complex power $\overrightarrow{S_R}$ flowing into the receiving-end can be calculated as:

$$\vec{S}_R = P_R + jQ_R = \vec{V}_R \cdot \vec{I}^* = \vec{V}_R \cdot \left(\frac{\vec{V}_S - \vec{V}_R}{\vec{Z}}\right)^*$$

$$= \left(V_R e^{j\phi}\right) \cdot \left(\frac{V_S e^{-j\delta} - V_R e^{-j\phi}}{Z e^{-j\theta}}\right)$$

$$= \frac{V_R V_S e^{j(\theta+\phi-\delta)} - V_R^2 e^{j\theta}}{Z} \tag{3}$$

Applying Euler's formula to separate (3) into its real and imaginary components leads to:

$$P_R = \frac{V_R V_S \cos(\theta + \phi - \delta) - V_R^2 \cos\theta}{Z} \tag{4}$$

$$Q_R = \frac{V_R V_S \sin(\theta + \phi - \delta) - V_R^2 \sin\theta}{Z} \tag{5}$$

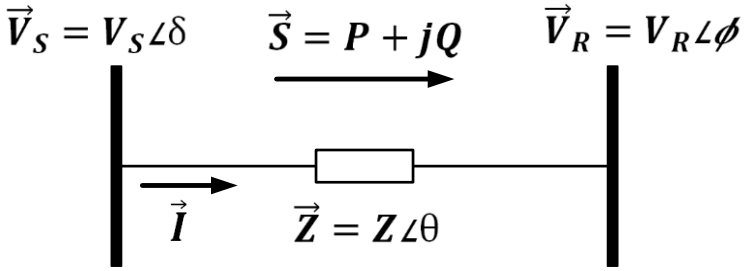

Figure 2: Power flowing through line

By defining $\vec{Z} = R + jX$, (4) and (5) can be expressed as:

$$P_R = \frac{V_R}{R^2 + X^2}[V_S(R\cos(\phi - \delta) - X\sin(\phi - \delta)) - V_R R] \tag{6}$$

$$Q_R = \frac{V_R}{R^2 + X^2}[V_S(X\cos(\phi - \delta) + R\sin(\phi - \delta) - V_R X)] \tag{7}$$

In the situation where the line impedance is assumed to be inductive ($\vec{Z} = jX$, or $\theta = 90^o$), the active and reactive powers are derived as:

$$P_R = -\frac{V_R V_S}{X}\sin(\phi - \delta) \tag{8}$$

$$Q_R = \frac{V_R V_S\cos(\phi - \delta) - V_R^2}{X} \tag{9}$$

Given that the phase angle difference between $\vec{V}_S$ and $\vec{V}_R$ is small, the small angle formula can be used to simplify the expressions and rewrite them as:

$$\phi - \delta \cong -\frac{XP_R}{V_R V_S} \tag{10}$$

$$V_S - V_R \cong \frac{XQ_R}{V_R} \tag{11}$$

It is therefore evident that the active power P_R is heavily dependent on the phase angle difference $\phi - \delta$, whereas the reactive power Q_R is strongly influenced by the amplitude difference $V_S - V_R$. Thus, the conventional *P/f* and *Q/V* droop scheme is often adopted in inductive networks to reproduce the behavior of dynamic ac generators.

Meanwhile, if the impedance is assumed to be resistive ($\vec{Z} = R$, or $\theta = 0^o$), the active and reactive powers delivered to the receiving-end become:

$$P_R = \frac{V_R V_S \cos(\phi - \delta) - V_R^2}{R} \tag{12}$$

$$Q_R = \frac{V_R V_S}{R} \sin(\phi - \delta) \tag{13}$$

Again by applying the small angle formula, the above expressions can be written as:

$$V_S - V_R \cong \frac{R P_R}{V_R} \tag{14}$$

$$\phi - \delta \cong \frac{R Q_R}{V_R V_S} \tag{15}$$

which suggest that the *P/f* and *Q/V* droops exchange their roles since active power is now affected more by amplitude difference, and reactive power is affected more by phase angle difference. Therefore the droop controller is modified accordingly for resistive impedance, obtaining the *P/V* and *Q/f* droops, also known as "reverse droops."

Given that microgrids are capable of operating in both grid-connected and islanded modes, where network impedances can vary from predominantly inductive to predominantly resistive, respectively, the droop control schemes applied to the inverters are also subject to variation—from *P/f* and *Q/V*, to *P/V* and *Q/f*, respectively.

GRID STIFFNESS

As previously noted, grid stiffness also impacts the control of grid-tied inverters. In the case of interconnection with a stiff grid, the grid impedance $\vec{Z}_{grid}$ in Fig. 3 is deemed negligible, suggesting that the load voltage $\vec{V}_L$ is equal to the grid voltage $\vec{V}_{grid}$. In this configuration, the load voltage is not regulated by the inverter; therefore, the active and reactive power at the inverter can be controlled by adjusting the inverter's voltage amplitude V_{inv} and voltage angle δ. An expression for these parameters is obtained below by invoking (6) and (7), and by referring to the variables listed in Table 3.

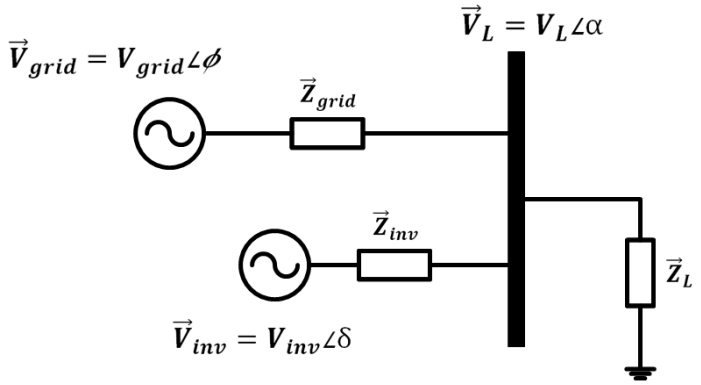

Figure 3: Grid interconnection of an inverter at a point of common coupling

$$\delta = \phi - \tan^{-1}\left(\frac{X - DR}{-R - DX}\right) \tag{16}$$

$$V_{inv} = \frac{A}{G[R\cos(\phi - \delta) - X\sin(\phi - \delta)]} \tag{17}$$

P	$\boldsymbol{P_{inv}}$
Q	$\boldsymbol{Q_{inv}}$
R	$\boldsymbol{R_{inv}}$
X	$\boldsymbol{X_{inv}}$
G	$\boldsymbol{V_{grid}}$
A	$PR^2 + PX^2 + G^2R$
B	$R^2 + X^2$
C	G^2X
D	$\frac{BQ + C}{A}$

Table 3: Substitution of variables

However, if grid interconnection in Fig. 3 is not stiff, a voltage drop is introduced, and the load voltage no longer remains fixed (that is, $\vec{V}_L \neq \vec{V}_{grid}$):

$$\vec{V}_L = \frac{\vec{V}_{inv}\vec{Z}_L\vec{Z}_{grid} + \vec{V}_{grid}\vec{Z}_{inv}\vec{Z}_L}{\vec{Z}_L\vec{Z}_{grid} + \vec{Z}_{inv}\vec{Z}_L + \vec{Z}_{grid}\vec{Z}_{inv}} \tag{18}$$

As a result, the system of equations given by (6), (7), and (18) convey that the control of the inverter becomes much less trivial in the absence of a stiff grid interconnection, particularly since the load impedance would need to be known.

This chapter introduced the effect of line impedance and grid stiffness on the control and flow of active and reactive power. The analysis revealed that the conventional *P/f* and *Q/V* droop strategies may not be suitable for islanded microgrids due to the parameters of low-voltage cables. The discussions were closely related to earlier

considerations regarding power curtailment of grid-tied inverters, since curtailment would be affected by line parameters.

Chapter 4: Energy Storage Sizing

PREFACE

Microgrid control and management require keen attention. As a result, stability issues in microgrids have steadily developed as an important topic of research. It is a point of emphasis, that microgrids operating as stand-alone systems are particularly challenging because, contrary to conventional power grids, the combined inertia of local synchronous generators may not be significant enough to ensure good stability margins and because individual loads may have power ratings comparable to the capacity of power generation units. Therefore, energy storage may be prescribed as a mitigation option toward achieving frequency and voltage stability in low-inertia systems. This chapter considers the electrical frequency dynamics of low-inertia microgrids as well as the voltage regulation implications of associated power electronic interfaces. A design criterion for sizing energy storage systems (ESS) is provided to ensure that frequency and voltage stability margins are not violated in ac microgrids when operating without a direct connection to a stiff grid.

Whether by virtue of natural disasters, physical deterioration, or malice, traditional electricity grids are prone to failure [40-43]. Because of its centralized architecture—one in which bulk power is delivered across long distances—the present-day electric power system is not only vulnerable [2, 8, 12], but also remarkably inefficient in terms of resource use. Specifically, in many power plants, nearly two-thirds of the energy produced by converting fuel into kilowatts escapes as heat, and another 8% dissipates as the electricity travels over transmission lines [44]. Numerous benefits are to be gained by integrating small-scale distributed energy resources into medium- to low-voltage networks and thereby forming localized interconnected grids known as microgrids.

The case for microgrids has been propelled by the steadfast adoption of PV generation technologies, whose price of installation has continued to decline over the years. According to a report by the Department of Energy's Lawrence Berkeley National Lab [45], the installed prices for solar photovoltaic power systems reduced by a range of 6% to 14% ($0.30 per watt to $0.90 per watt) from 2011 to 2012. Between 2008 and 2012, prices reduced by 80% (corresponding to $2.6 per watt) for PV systems generating less than 10 kW. Microgrids are anticipated to make a significant impact by reducing congestion, accommodating rapid changes in load or generation, offsetting the need for new generation, and providing ancillary services. Maximizing uptime for critical loads during extreme weather events [11, 14, 15, 43], complying with environmental standards, and easing the burden of replacing aging infrastructure are additional promises of microgrids.

Even though microgrids are a transcendent alternative to the traditional power grid, their prolific adoption remains contingent upon overcoming several key challenges. Maintaining adequate system inertia in real-time operations is one such challenge confronting reliable microgrid performance [46]; thus, microgrids with inadequate inertia may need to rely on load management, PV power curtailment, or energy storage to operate in a stable manner. Energy storage systems have been proposed extensively in the literature for mitigating power fluctuations associated with intermittent renewable sources [47-50], as well as for providing economic benefits that result from dynamic pricing [51-54]. Due to their fast response time and high ramp rates [55], energy storage systems are a feasible solution for preserving frequency and voltage stability in low-inertia microgrids. These systems can inject (or absorb) power into (or from) the microgrid, thus rendering frequency and voltage dynamics more benign. Therefore, the available response time and the overall robustness of the system can be increased, making

it more immune to perturbations.

Several existing publications have specifically investigated the sizing of energy storage systems. In light of integration challenges related to non-dispatchable wind [56-58] and PV [59] power, the sufficient apportionment of energy storage allows for increased predictability of power output, which equates to decreased reserve requirements. An economic approach for sizing a battery storage system (BSS) is adopted in [60], which proposes an analytical technique based on a cost-worth analysis. The cost of the system is associated with the installation, operation and maintenance of the BSS, whereas the worth is derived from the value of selling more energy to the grid. By treating the worth as a negative cost, the proposed method specifies the optimal sizing of the battery system by minimizing the summation of cost and worth. Optimal energy storage sizing has also been examined in [61] within the realm of dynamic pricing and renewable energy, with the aim of minimizing the long-run average cost of electricity used and investment in storage, if any, while satisfying all the demand. Yet, although significant in their own right, [56-61] do not address how energy storage systems should be sized to aid with frequency and voltage regulation.

More recently [62-65], the applicability of energy storage systems for frequency support in low-inertia microgrids has also been explored. These studies encompass a variety of energy storage technologies, such as supercapacitors [63, 64], batteries [65], and flywheels [62], with special consideration given to the control of such systems. The emphasis on stable microgrid operation has provided impetus for various alternative approaches as well. The use of a battery bank in conjunction with a dump load has been examined in [66] for an autonomous residential microgrid, leading to a hybrid solution for frequency stabilization while ensuring a higher overall efficiency. A more synergetic approach is suggested in [67] by harnessing the energy from plug-in electric vehicle

batteries in order to contribute to voltage balancing and frequency control during islanded microgrid conditions. The control approach is inspired by the existing droop control strategy [35, 68, 69], which involves subtracting proportional parts of the active and reactive powers from the frequency and amplitude, respectively, of a voltage reference. However, although the various technologies in the abovementioned studies are recognized for their ability to improve power quality, their sizing criteria is overlooked.

This chapter, alternatively, does not make a commitment to the *type* of storage technology, but instead formulates a methodology for evaluating the capacity requirement of an energy storage system designed to provide frequency or voltage support.

PROBLEM DESCRIPTION

An essential characteristic of the microgrid is its ability to electrically isolate itself from the utility grid for autonomous operation (known as islanding), as well as to seamlessly recombine to function as a single entity. When in island mode the microgrid must be assured of stable operation, which may prove to be challenging due to the limited inertia available from rotating masses of synchronous generators and turbines. Since the inertia from these rotating masses contributes to transient stability in the moments subsequent to disturbances, microgrids with low levels of rotational inertia will have negative implications on frequency dynamics.

The microgrid inertia is a function of the number of operating generators as well as the individual inertia of each of those generators. Synchronous generators can contribute to the overall system inertia due to the strong coupling between their rotational speed and electrical frequency; however, in islanded microgrids, the number of operating generators will undoubtedly be less than in large interconnected systems, meaning that

the microgrid inertia will also be less. Further aggravating the issue is the fact that replacing conventional generation by PV generation—which is to be expected in microgrids with distributed generation—leads to an even lower microgrid inertia since PV sources are practically inertia-less because of the decoupling through power electronic devices. This notion is validated in [70] and [71], which confirm that the integration of renewable energy sources in the generation mix will cause frequency support to deteriorate since no inertial response is delivered from those sources during a frequency event. Due to lower microgrid inertia, the remaining synchronous generators have less time to react which compromises frequency stability margins. It is vital for deviations from nominal frequency to be kept small in order to prevent damaging vibrations in synchronous machines and to avoid load shedding [46].

Voltage stability is equally crucial to acceptable microgrid performance, as maintaining the grid voltage within a given range is a necessary requirement for the stable operation of any power system. A particular challenge specifically inherent in low-voltage microgrids is attributed to their expected predominantly-resistive line impedances, which render the commonly considered conditions used in traditional grid droop control method inapplicable [28].

IEEE Standard 1547, which stipulates that grid-tied inverters should not actively regulate the voltage at the point of common coupling, presents in the U.S. an impediment to both frequency and voltage stability. Since in the U.S. grid-tied inverters are not currently permitted to supply local reactive power, the microgrid's synchronous generators are tasked with meeting the reactive load demand; consequently, the amount of active power available by the synchronous generators for frequency control is limited. With regard to voltage stability, the absence of reactive power from grid-tied inverters means that voltage regulation must be accomplished by other means such as power

electronic circuits, as demonstrated in the forthcoming analysis.

METHODOLOGY

Frequency Stability

Frequency control in conventional grids is accomplished on three time-dissociated levels (termed *primary*, *secondary*, and *tertiary*), which are deployed in successive order. Recent studies [28] suggest a similar approach for frequency control in microgrids as well by implicating distributed generators, energy storage systems, and active loads.

The inertia-based methodology developed in this work for sizing an energy storage system is depicted in Fig. 4. This methodology describes the energy storage capacity required to arrest the frequency deviation (primary control) and to subsequently restore the deviated frequency (secondary control). The capacity requirement $E_{storage}$ [kWh] is derived from a combination of known and forecasted parameters, where $\bar{f}_1$ [p.u.] and $\bar{f}_2$ [p.u.] are the initial and final frequency, respectively, of the microgrid, $H_{\mu G}$ [s] is the microgrid's equivalent inertia, $\Delta\bar{P}_{\mu G}$ [p.u.] is the generation-load mismatch (defined as generation minus demand) within the microgrid, Δt [s] is the duration of the mismatch, H_{def} [s] is the inertia deficiency of the microgrid otherwise needed to satisfy the frequency control requirement, and $P_{\mu G,g}$ [W] is the generated microgrid power. (Note: overbars will hereinafter indicate per-unit quantities).

The proposed methodology is predicated on the relationship between a generator's rotational energy and its inertia constant H_{gen}. Specifically, the kinetic energy stored in a single generator shaft corresponds to H_{gen} seconds of rated power S_{gen}, at which time the generator will have spun down to zero speed. In order for the speed—analogously, frequency—to be confined within a specified deviation $\Delta\bar{f}_{max}$,

the inertia *deficiency* will be calculated and deemed a key parameter in formulating the design criterion.

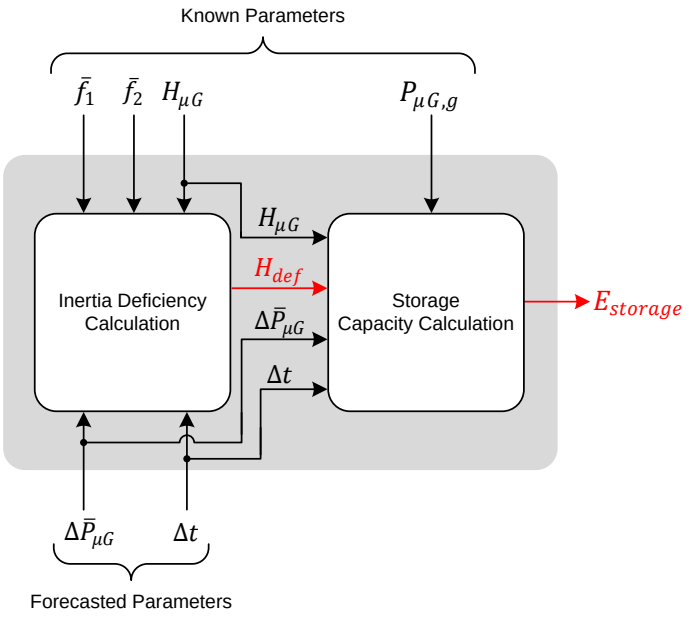

Figure 4: Overview of proposed energy storage sizing methodology

Although the analysis undertaken in this work will consider only under-frequency events (i.e., $\Delta\bar{P}_{\mu G} < 0$), the prescribed methodology is equally applicable to over-frequency situations as well; therefore, energy storage can be commissioned for both charging *and* discharging modes of operation using the proposed approach.

The inertial frequency response of generators describes their ability to absorb or release kinetic energy to arrest frequency deviations. The equation governing rotor motion, related by the torque unbalance acting on the rotor, is given by

$$J\frac{d\omega_m}{dt} = T_a = T_m - T_e \tag{19}$$

where

J = combined moment of inertia of generator and turbine, [kg·m^2]

ω_m = mechanical angular velocity of rotor, [rad/s]

t = time, [s]

T_a = accelerating torque, [N·m]

T_m = mechanical torque, [N·m]

T_e = electromagnetic torque, [N·m]

Furthermore, using ω_{0m} [rad/s] to denote the rated mechanical angular velocity, the inertia constant of the generator H_{gen} [s] is expressed proportional to its power rating as:

$$H_{gen} = \frac{J \cdot \omega_{0m}^2}{2 \cdot S_{gen}} \tag{20}$$

Rearranging (20) and substituting into (19),

$$\frac{2 \cdot H_{gen} \cdot S_{gen}}{\omega_{0m}^2} \cdot \frac{d\omega_m}{dt} = T_m - T_e \tag{21}$$

Observing that $\frac{\omega_{0m}}{S_{gen}} = \frac{1}{T_{rated}}$, and converting per-unit mechanical angular velocity to per-unit electrical angular velocity $\bar{\omega}_e$, (21) can be expressed as

$$2 \cdot H_{gen} \cdot \frac{d\bar{\omega}_e}{dt} = \bar{T}_m - \bar{T}_e \tag{22}$$

An additional conversion of torque to power and of angular velocity to rotational frequency yields an equation describing the rate of change of frequency (ROCOF) for a microgrid:

$$\bar{f}\frac{d\bar{f}}{dt} = \frac{\bar{P}_{\mu G,g} - \bar{P}_{\mu G,d}}{2 \cdot H_{\mu G}} = \frac{\Delta \bar{P}_{\mu G}}{2 \cdot H_{\mu G}} \tag{23}$$

where

$$H_{\mu G} = \sum_{i=1}^{N} \frac{H_{gen,i} \cdot S_{gen,i}}{S_{\mu G}} \tag{24}$$

$\bar{P}_{\mu G,g}$ is the generated microgrid power, $\bar{P}_{\mu G,d}$ is the demanded microgrid power, S_{gen} [VA] is the rated power of each i generator, N is the total number of generators in the microgrid, and $S_{\mu G}$ [VA] is the microgrid power capacity.

As conveyed by Fig. 5, a power imbalance $\Delta \bar{P}_{\mu G}$ during the time interval $\Delta t = t_f - t_i$ causes the angular frequency to change. It is proposed that the incorporation of energy storage may administer remedial action by serving to arrest the frequency deviation during the defined time interval $\Delta t_1 = t^* - t_i$ and to subsequently restore the frequency during the remaining time interval $\Delta t_2 = t_f - t^*$. The time intervals Δt_1 and Δt_2 denote the time period where primary control and secondary control, respectively, occur, and together comprise Δt.

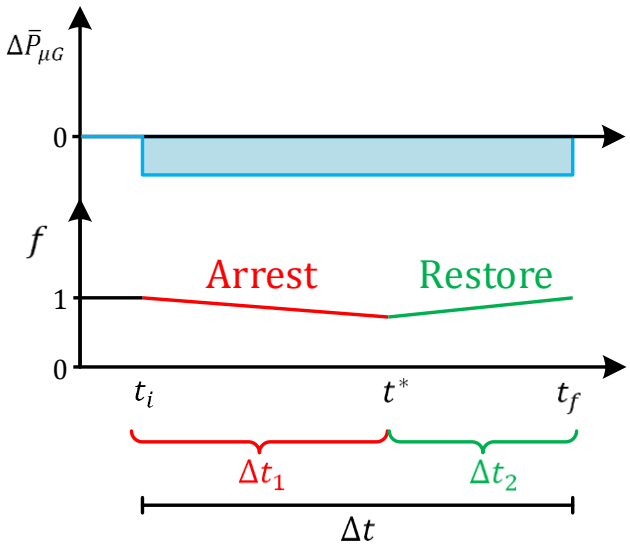

Figure 5: Primary and secondary control, with their associated variables

Given the initial frequency of operation $\bar{f}_1$ at the onset of the power imbalance, an expression for frequency deviation $\Delta\bar{f}$ is obtained by integrating (23):

$$\int_{\bar{f}_1}^{\bar{f}_2} \bar{f}\, d\bar{f} = \int_{t_i}^{t_f} \frac{\Delta\bar{P}_{\mu G}}{2 \cdot H_{\mu G}}\, dt$$

$$\Delta\bar{f} = \bar{f}_2 - \bar{f}_1 = \sqrt{\frac{\Delta\bar{P}_{\mu G} \cdot \Delta t}{H_{\mu G}} + \bar{f}_1^2} - \bar{f}_1 \tag{25}$$

where $\bar{f}_2$ is the resulting frequency of operation at t_f. Since violation of the frequency stability criterion $|\Delta\bar{f}| \leq \Delta\bar{f}_{max}$ can be attributed to insufficient inertia, the inertia deficiency $H_{def,1}$ [s] needed to accomplish primary control within Δt_1 is sought and calculated as

$$H_{def,1} = \frac{\Delta \bar{P}_{\mu G} \cdot \Delta t_1}{\bar{f}_2^2 - \bar{f}_1^2} - H_{\mu G} \tag{26}$$

which is in turn utilized to obtain the energy storage capacity requirement $E_{storage,1}$ [kWh]:

$$E_{storage,1} \geq \frac{H_{def,1} \cdot P_{\mu G,g} \cdot \left|\Delta \bar{P}_{\mu G}\right| \cdot \Delta t_1}{\left(H_{def,1} + H_{\mu G}\right)(3.6 \times 10^6)} \tag{27}$$

Energy storage sizing for secondary control $E_{storage,2}$ takes place during Δt_2 and is derived in a similar fashion with the exception that, now, $\bar{f}_2 > \bar{f}_1$:

$$H_{def,2} = \frac{\Delta \bar{P}_{\mu G} \cdot \Delta t_2}{\bar{f}_2^2 - \bar{f}_1^2} - H_{\mu G} \tag{28}$$

$$E_{storage,2} \geq \frac{H_{def,2} \cdot P_{\mu G,g} \cdot \left|\Delta \bar{P}_{\mu G}\right| \cdot \Delta t_2}{\left(H_{def,2} + H_{\mu G}\right)(3.6 \times 10^6)} \tag{29}$$

The parameter $H_{def,1}$, a positive-valued number, is the amount of *additional* inertia needed to suppress the frequency decay to $\bar{f}_2$ in Δt_1 seconds. Conversely, $H_{def,2}$ is a negative-valued number indicating the *excess* amount of inertia needed to be forgone in order to restore the frequency to $\bar{f}_2$ within a time interval of Δt_2 seconds. Since both $H_{def,1}$ and $H_{def,2}$ are interpreted as *virtual* quantities of time, the expressions in (27) and (29) are required to be scaled by $(H_{def,1} + H_{\mu G})$ and $(H_{def,2} + H_{\mu G})$, respectively. It is a point of emphasis, that the forecasted energy imbalance resulting from the product $\Delta \bar{P}_{\mu G} \cdot \Delta t$ need not be time-invariant. That is, the proposed methodology is valid for *any*

forecasted energy imbalance; although, in this study, a time-invariant load step is considered in order to foster a more intuitive understanding of energy imbalance.

Voltage Stability

The lack of inertia, together with the resistive feeder characteristics of microgrids, invokes ramifications with regard to voltage regulation as well [28]. From the equations of power-flow obtained in (14) and (15), it follows that the effects on the delivered active power P_R and reactive power Q_R are interchanged in the case of a resistive line impedance. That is, the active power is affected by the voltage amplitude difference whereas the reactive power is affected by the phase angle difference (with the caveat that reactive power-flow is from lower phase angle to higher phase angle). If a given power $P_{R,1} + jQ_{R,1}$ [kW, kVar] is delivered to a load whose terminal voltage is at the allowable minimum V_{min}, then the voltage drop ΔV_1 across the line impedance $Z = R + jX$ can be approximated by

$$\Delta V_1 = V_S - V_{min} \cong \frac{P_{R,1}R + Q_{R,1}X}{V_{min}} \tag{30}$$

At this point, any frequency disturbance requiring compensation by an increase in power to a new value of $P_{R,2}$ [kW]—without violating V_{min}—would necessitate *local* reactive power Q_{PE} [kVar] by the power electronic circuit. Thus, in order to not violate the minimum voltage despite the increase in load to $P_{R,2}$,

$$\frac{P_{R,1}R + Q_{R,1}X}{V_{min}} = \frac{P_{R,2}R + Q_{R,2}X}{V_{min}} \tag{31}$$

where $Q_{R,2}$ accounts for the contribution of the power electronic circuit, i.e., $Q_{R,2} = Q_{R,1} - Q_{PE}$. Therefore, by defining the increase in active power as $\Delta P_R = P_{R,2} - P_{R,1}$, the amount of local reactive power provided by the power electronic circuit to prevent further reduction of voltage can be calculated as

$$Q_{PE} = \Delta P_R \frac{R}{X} \tag{32}$$

which suggests that higher values of reactive power injection are required for higher R/X ratios (e.g., microgrids). Given a response time Δt_V [s] needed to ensure the abovementioned voltage regulation performance, the corresponding energy capacity value E_V [kVarh] is obtained as

$$E_V = \frac{Q_{PE} \cdot \Delta t_V}{3600} \tag{33}$$

It should be noted that the preceding analysis is equally relevant to voltage rise scenarios as well, where it is desired that a particular voltage level not be *exceeded* by allowing the power electronic circuit to absorb (rather than inject) reactive power.

The relationships in (7), (8), and (11) imply that the traditional grid droop control method needs to be adapted to microgrids and that the overall control process becomes complicated due to the uncertainty of line impedances and control parameters. It is therefore imperative that a power electronic circuit interfacing an ac microgrid with energy storage be capable of regulating frequency and voltage depending on the characteristics of the microgrid.

MODELING

Modeling of a 480 V, 875 kVA microgrid and its comprising components is undertaken in *MATLAB/Simulink* using the phasor simulation method. The microgrid model, illustrated in Fig. 6, entails generating sources in the form of synchronous generators and PV arrays, a base load to establish the microgrid's nominal frequency, a load step to introduce a frequency disturbance, an energy storage system to provide frequency support, and a power electronic circuit to provide voltage support.

The microgrid generation mix, shown in Table 4, consists of a 200 kW PV system along with various small synchronous generators that together constitute an equivalent microgrid inertia of 0.15s as indicated by (24). Given that the PV system operates at unity power factor, the synchronous generators are required to supply reactive power to the load and therefore contribute, in aggregate, to 800 kW of the 875 kVA microgrid capacity. This implies that any additional active-power demand or any drop in PV power output would exceed the generation capacity and negatively impact the microgrid frequency, thus advocating the case for energy storage.

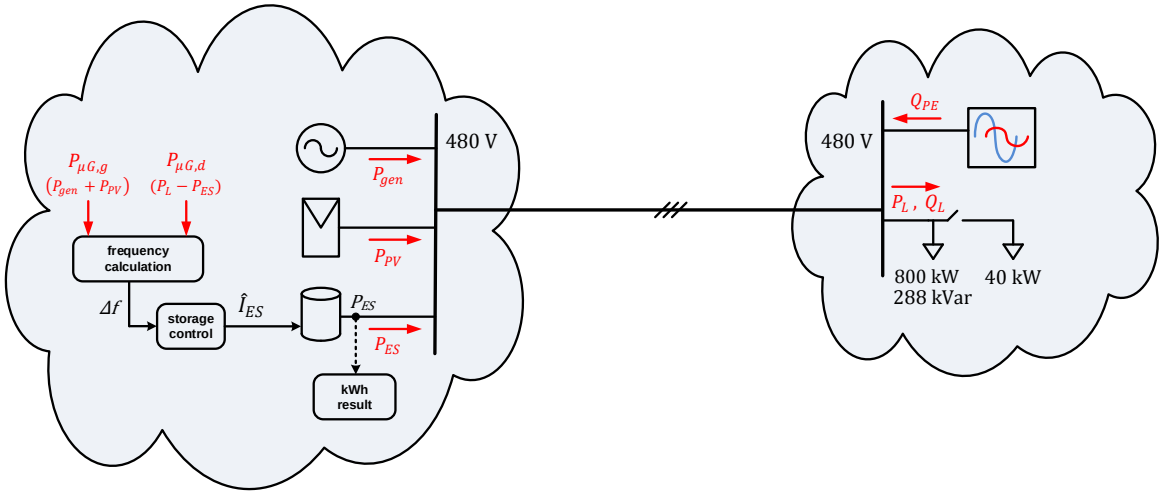

Figure 6: Topology of islanded microgrid under study

Type	S_{gen} [kVA]	H_{gen} [s]	Rated PF	Q_{min} [kVar]	Q_{max} [kVar]	P_{min} [kW]	P_{max} [kW]	P_{gen} [kW]	Q_{gen} [kVar]	PF
SG	69	0.26	0.8	0	41	33	55	55	41	0.80
SG	69	0.26	0.8	0	41	26	61	60	33	0.88
SG	69	0.26	0.8	0	41	18	65	65	22	0.95
SG	156	0.2	0.8	0	94	67	131	130	84	0.84
SG	156	0.2	0.8	0	94	53	141	140	66	0.90
SG	156	0.2	0.8	0	94	34	150	150	42	0.96
PV	200	0	1.0	0	0	0	200	200	0	1.0
	$S_{\mu G}$ = 875	**$H_{\mu G}$ = 0.15**						**$P_{\mu G,g}$ = 800**	**$Q_{\mu G,g}$ = 288**	

Table 4: Generation mix for islanded microgrid under study

Synchronous Generator

The synchronous generator is represented in voltage-behind-reactance form, where the voltages and internal impedance branches are configured in a wye connection. Relevant parameters for small synchronous generators [72] are used to fulfill the modeling requirements. The frequency $\bar{f}$ is calculated from the magnitude of the power imbalance as conveyed by the diagram in Fig. 7, where $\bar{f}^*$ is the nominal frequency.

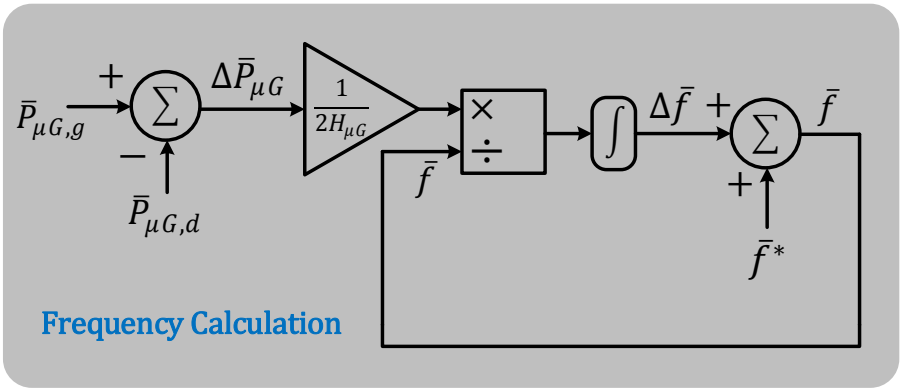

Figure 7: Frequency calculation for islanded microgrid under study

PV Sources, ESS, and Power Electronic Circuit

PV sources are incorporated into the generation mix in order to highlight their detrimental effect on the microgrid's frequency dynamics. The PV sources, energy storage system, and power electronic circuit are modeled similarly. That is, three-phase power (P_{PV}, P_{ES}, or Q_{PE}) is delivered from these devices by employing controlled current sources whose values (complex numbers) are used at the next simulation timestep to inject corresponding complex-valued current in each phase of the distribution system as depicted in Fig. 8.

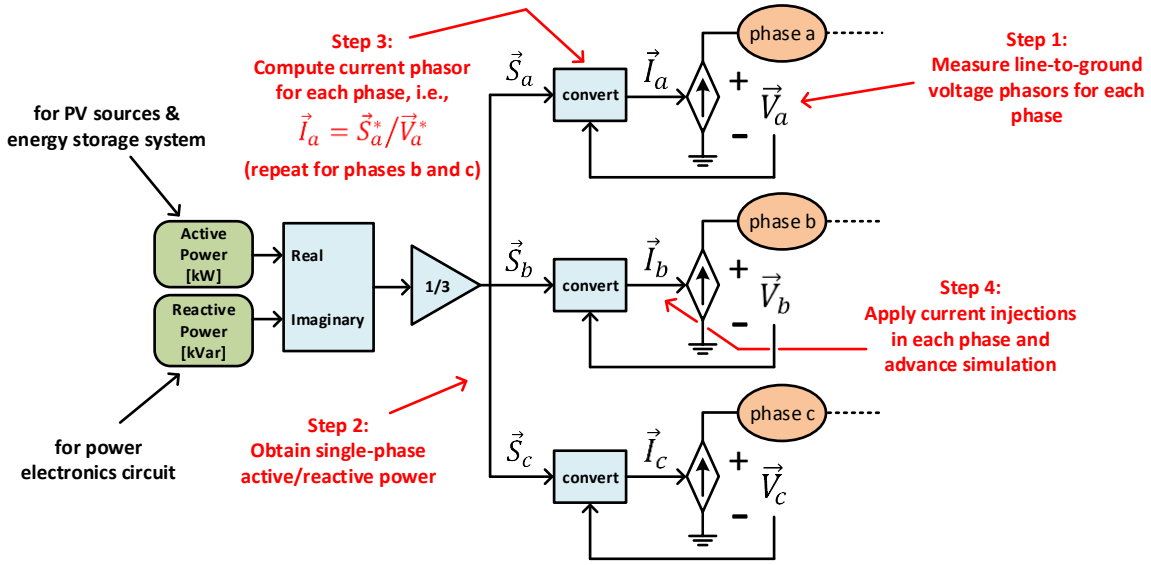

Figure 8: Modeling of PV sources, energy storage system, and power electronic circuit

Control of the ESS, shown in Fig. 6 and Fig. 9, is implemented by using frequency deviation as an indicator for how much power should be injected into the microgrid. The variable $\hat{I}_{ES}$ represents the current signal driving the ESS, and t^* signifies

the transition between primary and secondary control. Primary control is realized via the droop control strategy in order to subdue the frequency deviation, whereas secondary control is achieved by means of a P-I controller in order to restore the frequency. Additionally, P_{ES} is used to calculate the kWh value of energy expended by the storage system, which is to be compared with the proposed method derived in (27) and (29).

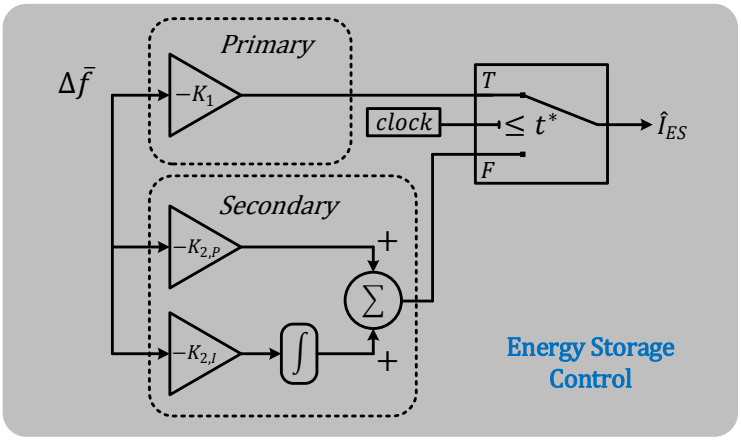

Figure 9: Energy storage control for islanded microgrid under study

Load

The microgrid load is modeled similarly to the sources in Fig. 8, with the exception that the current injections are instead treated as current sinks. The active power component of the base load is chosen equal to $P_{\mu G,g}$ (800 kW) and serves to establish the nominal frequency of the microgrid. The reactive power component of the base load (288 kVar) equals the summation of the maximum allowable reactive power from each synchronous generator. Since this implies that the generators are operating at their full capacity, when a three-phase circuit breaker closes at time t_i a power imbalance within the microgrid is presented in the form of a load step, resulting in a frequency decay. It

should be noted that the load power and the power demand observed by the microgrid are not necessarily equal due to the contribution from the ESS (i.e., $P_{\mu G,d} = P_L - P_{ES}$).

RESULTS AND DISCUSSION

Frequency Stability

With the microgrid initially supporting a load of 800 kW and 288 kVar, a 5% (40 kW) load step is introduced at $t_i = 1$s, lasting for $\Delta t = 14$s. A rapid decay in frequency ensues as shown in Fig. 10, due to a combination of limited microgrid inertia and maximum allowable generator output. Barring remedial action, the frequency violates $\Delta \bar{f}_{max} = 0.05$ within 0.29 seconds and continues to decay until reaching 0 p.u. at $t = 4$ seconds.

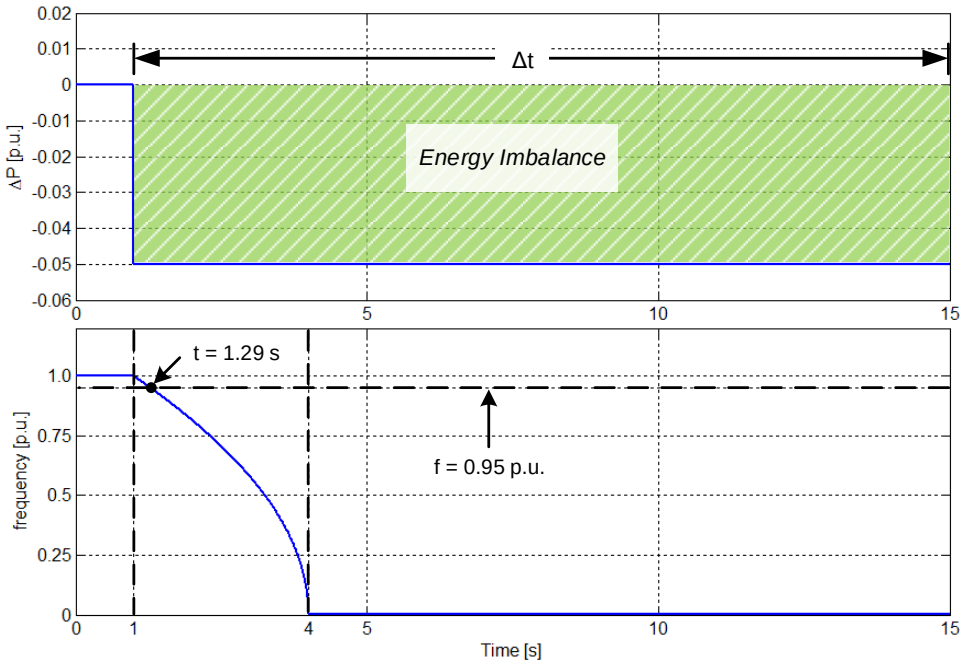

Figure 10: Load step experienced by microgrid during Δt (Top) and resulting frequency decay (Bottom)

Primary Frequency Control

Energy storage sizing for primary frequency control is evaluated for the three different cases tabulated in Table 5. In the first case, it is desired that the frequency deviation be limited to 0.96 p.u. within 2 seconds of the disturbance. The second and third cases have different requirements for the minimum frequency (0.95 p.u. and 0.98 p.u., respectively), but both achieve primary control within 4 seconds of the disturbance. The calculated results obtained from the methodology developed previously are in agreement with the simulated results from the *MATLAB/Simulink* microgrid model which are shown in Fig. 11.

Secondary Frequency Control

Energy storage sizing for secondary frequency control is investigated similarly by utilizing the ESS and observing the energy expenditure needed for frequency restoration. As shown in Table 6 and Fig. 12, deviated frequencies resulting from the previous cases are to be either fully (i.e., $\bar{f_2} = 1.0$) or partially restored.

The frequency in the first case is restored from 0.96 p.u. to 0.99 p.u. within 12 seconds and requires the most energy from the ESS as compared to the other two cases. However, the total energy requirement for *both* primary and secondary control is the least for this case as compared to the other two cases. The deviated frequencies from the second and third cases are fully restored within the same amount of time (10 seconds). As expected, the energy requirement for achieving secondary control in the second case is more than that of the third case because the second case's margin of restoration is also more. Once the energy imbalance concludes, the frequency will remain at $\bar{f_2}$ for $t > t_f$ until the next disturbance.

Δt_1 [s]	Δf_{max} [p.u.]	$-K_1$ [kW/Hz]	$H_{def,1}$ [s]	kWh (calculated)	kWh (simulated)
2	0.04	-16.7	1.13	0.0196	0.0195
4	0.05	-13.3	1.90	0.0412	0.0411
4	0.02	-33.4	4.90	0.0431	0.0431

Table 5: Primary frequency control: Performance indices

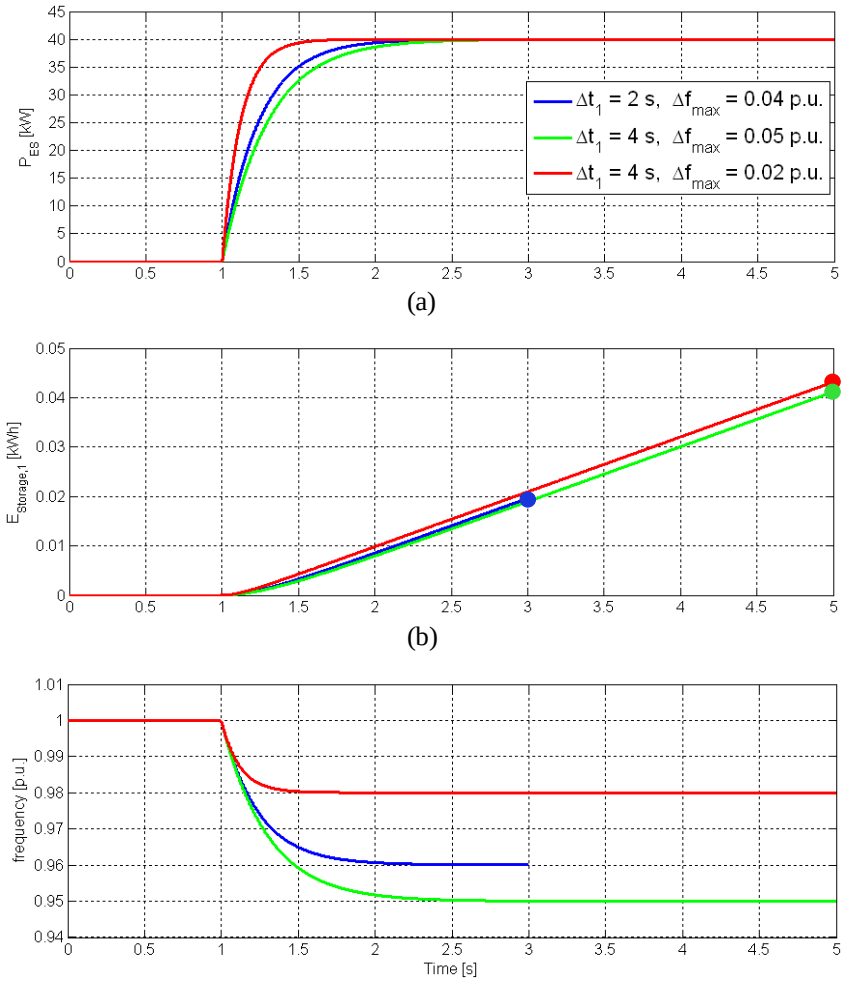

Figure 11: Primary frequency control. (a) ESS power output. (b) Energy expended by ESS. (c) Microgrid frequency.

Δt_2 [s]	f_2 [p.u.]	$-K_{2,P}$ [kW/Hz]	$-K_{2,I}$ [kW/Hz·s]	$H_{def,2}$ [s]	kWh (calculated)	kWh (simulated)
12	0.99	-20.78	-1.65	-10.41	0.1353	0.1354
10	1.0	-8.31	-2.98	-5.28	0.1144	0.1145
10	1.0	-13.86	-6.79	-12.78	0.1124	0.1124

Table 6: Secondary frequency control: Performance indices

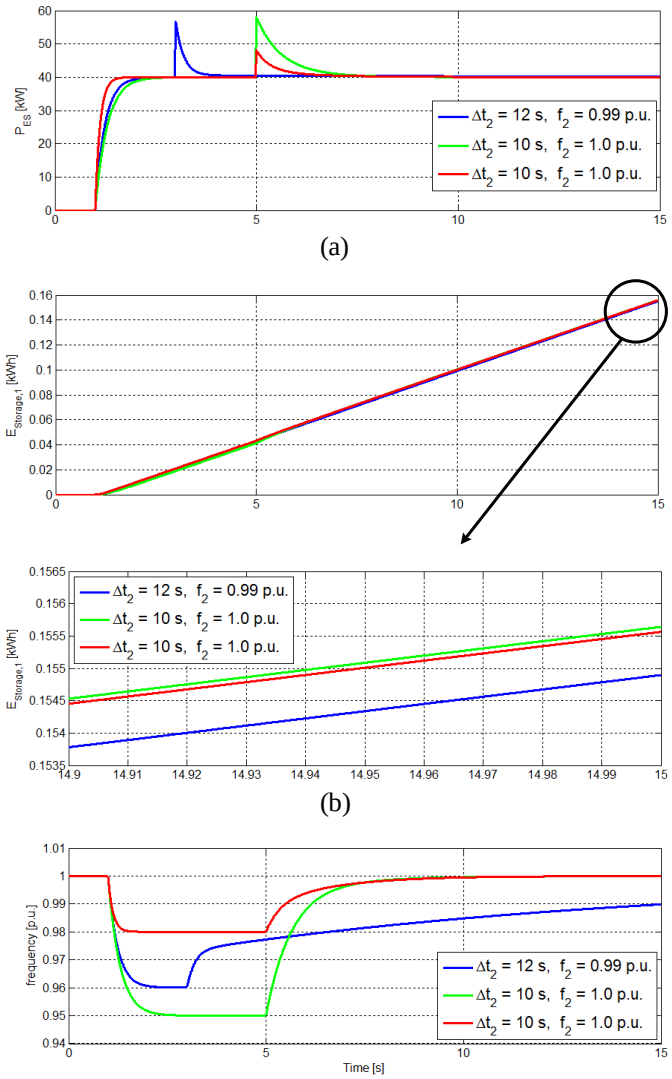

Figure 12: Primary and secondary frequency control. (a) ESS power output. (b) Energy expended by ESS. (c) Microgrid frequency.

The proposed methodology reveals that, given a forecasted energy imbalance during Δt, energy storage can be sized to suppress and subsequently restore frequency deviations. The sizing methodology is described by two degrees of freedom: 1) the sub-time intervals within Δt in which primary and secondary frequency control are desired to occur, and 2) the amount of frequency variation during each level of control.

Voltage Stability

It was previously demonstrated how energy storage can be employed to maintain frequency stability when additional load is introduced at t = 1s. However, although the contribution from energy storage is conducive to frequency stability, the increase in provided power may result in violating the minimum allowable voltage at the receiving-end of a line. It is therefore important to consider the voltage regulation implications of power electronic interfaces so that microgrid stability can be deemed effective.

With the microgrid generators operating at their full capacity to fulfill the load requirement of 800 kW and 288 kVar, the receiving-end voltage V_R is at the minimum allowable value of 456 V (5% lower than nominal). When a load of 40 kW is subsequently introduced, the energy storage system reacts in response to the frequency deviation by injecting additional active power. In order to keep V_R constant at 456 V despite the active power injection, a certain amount of reactive power is needed depending on the line impedance characteristics (i.e., R/X ratio).

The power electronic interface in the abovementioned scenario is set to supply 200 kVar at t = 1s, and the R/X ratio is varied in order to observe the effect on voltage regulation. Consistent with the derivation in (32), Fig. 13 conveys that voltage regulation is accomplished when the R/X ratio is 5. It is noted that more reactive power is required for a higher R/X ratio since V_R is less than 456 V, and less reactive power is required for

a lower R/X ratio since V_R is more than 456 V. This means that power electronic interfaces should be controlled to provide active or reactive power depending on the feeder characteristics, because voltages are less sensitive to reactive power in low-voltage networks such as the one considered in this study.

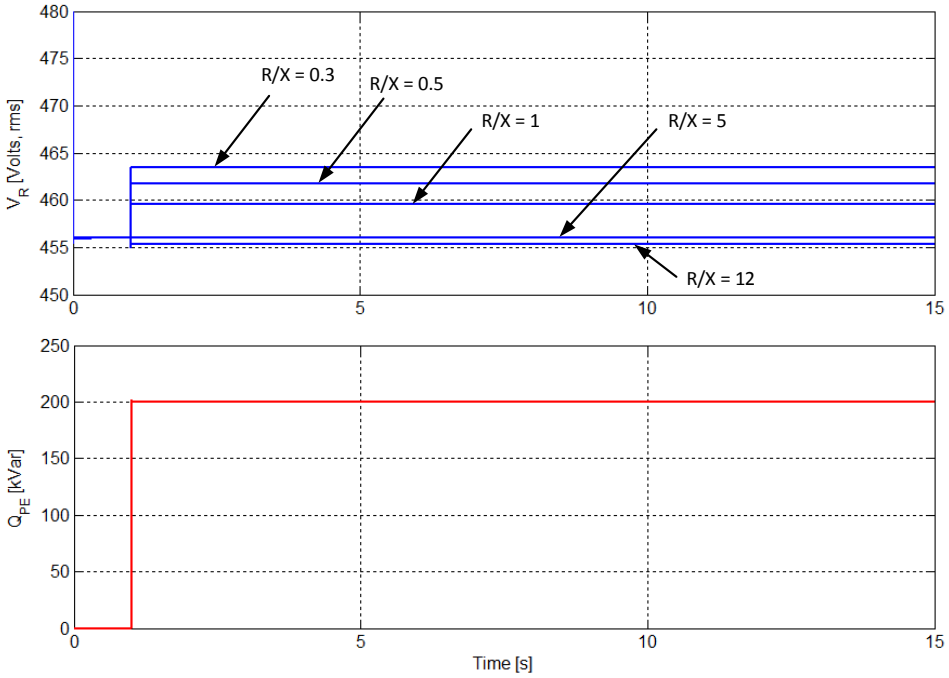

Figure 13: Impact of R/X ratio on receiving-end voltage (Top) when 200 kVar of reactive power is injected at t = 1s (Bottom)

It is observed that reliable microgrid operation can be a challenging proposition particularly for low-inertia systems, because frequency is sensitive to load changes, and power quality must be ensured by means of on-site resources such as distributed generators, energy storage systems, and power electronic interfaces. This paper investigated the impact of energy storage systems on the frequency and voltage stability of low-inertia microgrids. Results indicated that the integration of energy storage can

substantially improve frequency control by reducing the rate of change of frequency and by restoring the deviated frequency. Voltage regulation was shown to be effective through the provision of reactive power, although this approach may be better suited for distribution systems with low R/X values.

Chapter 5: Mueller Neighborhood—A Potential Microgrid with Distributed Generation

This chapter will describe an existing residential community, named Mueller, and evaluate the effects of high penetration levels of PV and EV assets by using actual recorded data. It is important to observe how the growth and addition of such technologies impacts the electrical infrastructure, power quality, and economics of electrical distribution systems. Although Mueller does not presently have the capability to island itself from the electric grid, the analysis will serve to raise awareness regarding the operational implications of this- and similar communities, should they be retrofitted to a microgrid.

THE MUELLER NEIGHBORHOOD

The Mueller neighborhood, a 711-acre mixed-use development in Austin, TX, is a prototypical development model similar to hundreds of it across the United States. This neighborhood is part of a smart grid demonstration project involving original research and commercialization efforts addressing consumer energy use.

Pecan Street Inc., a non-profit organization headquartered at the University of Texas at Austin, is responsible for this project. This organization is a major source of original customer energy use and behavioral research data; it generates an extensive database of electricity usage with good time resolution and spatial resolution to the individual residences. Homes and commercial buildings in Pecan Street's research trials are instrumented with systems that record electricity use from the whole building and individual circuits at intervals ranging from one minute to one second.

Nearly 200 homes at Mueller are instrumented with secondary (second energy meter) and tertiary (inside homes) meters to report electrical data in one-minute and one-

second intervals, and gas data in 15-second intervals. More than 50 homes report 15-second interval water use. Many homes are equipped with PV systems, of which 40% face west (the nation's highest residential concentration of west-facing, load-aligned PV generation). The research trials also include what is likely the nation's highest residential concentration of electric vehicles with Level-2 charging. The Mueller neighborhood showing the high concentration of residential PVs is shown in Fig. 14.

Figure 14: Mueller homes equipped with rooftop PVs (approximately 6 kW each)

Electric Service

A one-line diagram of the Mueller community is shown in Fig. 15. Substation 1 is shown along the top of the figure with its two transformers rated at 30 MVA each. These transformers step down sub-transmission voltage (69 kV) to distribution-level voltage (12.47 kV). Each transformer serves three feeders at 12.47Y/7.2 kV. Each feeder, in turn, serves other urban communities or commercial areas via service laterals [73]. Following

feeder 1 downward from substation 1, along various locations along the feeder are capacitor banks. (This is true of other feeders as well.) These capacitor banks are controlled by diurnal light and are meant to improve service quality in the surrounding areas (e.g., provide power factor correction, reduce feeder voltage drops, and provide voltage and reactive power support).

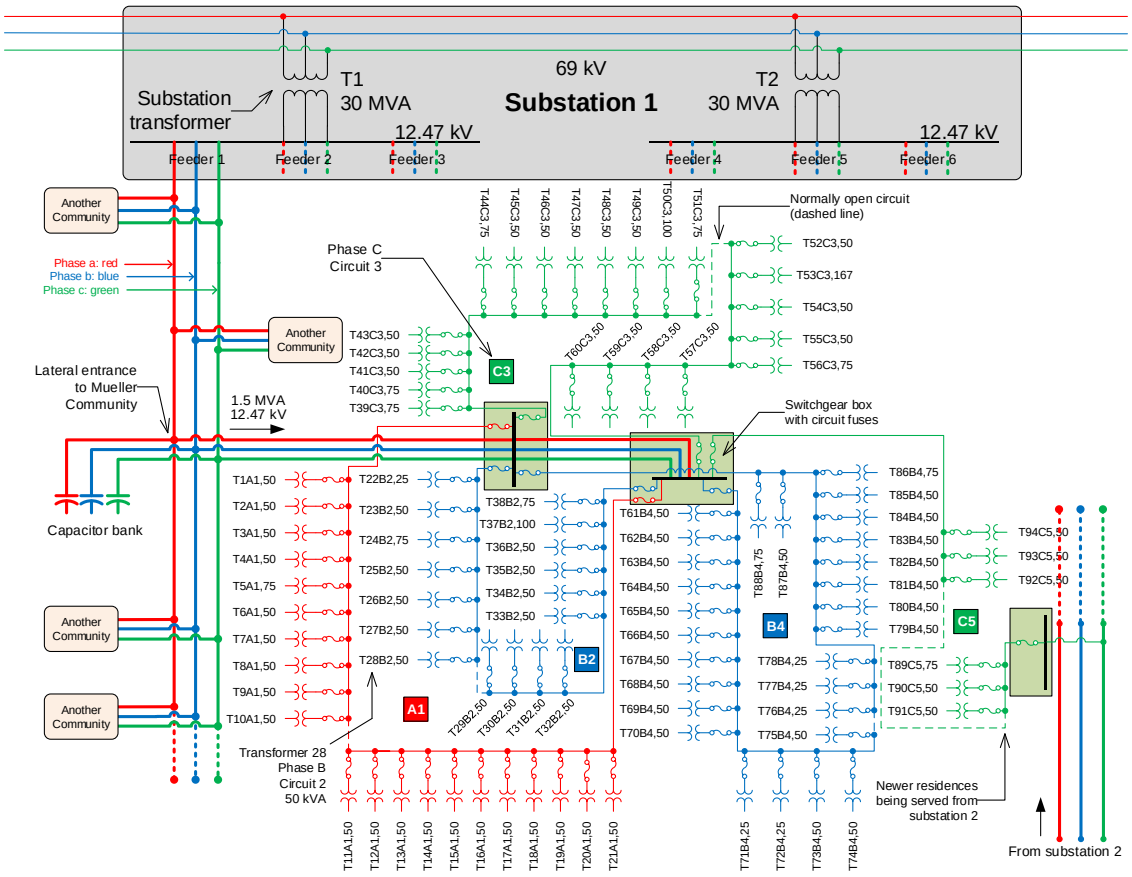

Figure 15: One-line diagram of Mueller's distribution system

Phase *c* from a feeder at substation 2 serves the newer residences in Mueller, although most of the electric service provided from substation 1 is eventually intended to be moved to substation 2. Transformer 2 (T2) at substation 1 is in service, but appears disconnected in the one-line diagram. This is because the focus of this work is the electric service to Mueller, not to the neighboring areas serviced by T2 and substation 2. Shown from left-to-right in Fig. 15 is the lateral service entrance to the Mueller community which has values of 1.5 MVA at 12.47 kV.

The conductor colors (red, blue, green) represent the different electrical phases (*a*, *b*, *c*, respectively). The thicker lines in Fig. 15 represent three-phase overhead lines or underground cables. The thin lines inside the community (in corresponding color) represent single-phase distribution cables. Single-phase cables run from switchgear boxes to each distribution transformer in a circuit. Each phase incoming from the lateral to the first switchgear box is split into sub-circuits. For example, phase *b* splits into circuits 2 and 4. These circuits operate in open-loop configuration, as indicated by the dashed-line segments.

The transformers are identified according to an assigned label, which reflects the transformer number (94 total), the phase that serves the transformer (*a*, *b*, or *c*), the circuit that the transformer belongs to, and the transformer rating. For example, transformer "T28B2,50" represents transformer #28, is served from phase *b*, is on circuit 2, and has a rating of 50 kVA.

Each of the circuits (5 total) is protected by 65 A fuses at the switchgear boxes, and provides electric service to its downstream transformers. The primary-side service voltage to each transformer (7.2 kV, phase to ground) is stepped down to a usage level of 240/120V (split-phase). The distribution transformer types are tabulated in Table 7. The asset count for each transformer is tabulated in Table 8, Table 9, and Table 10.

kVA	Primary Voltage (V)	Secondary Voltage (V)	No load losses (W)	Loaded losses (W)	Z %	Count
25	7,200	240/120	71	228	2.3	6
50	7,200	240/120	105	404	2.3	74
75	7,200	240/120	167	456	2.5	11
100	7,200	240/120	181	683	2.5	2
167	7,200	240/120	248	1234	3.0	1
					Total	94

Table 7: Distribution transformer types

Phase & Circuit	Xfm. #	Xfm. ID	kVA	# Homes	# PVs	# EVs
A1	1	T01A1,50	50	8	1	0
A1	2	T02A1,50	50	10	1	0
A1	3	T03A1,50	50	10	4	2
A1	4	T04A1,50	50	8	3	2
A1	5	T05A1,75	75	11	0	1
A1	6	T06A1,50	50	8	3	2
A1	7	T07A1,50	50	8	2	2
A1	8	T08A1,50	50	10	4	4
A1	9	T09A1,50	50	8	3	2
A1	10	T10A1,50	50	8	2	2
A1	11	T11A1,50	50	9	4	2
A1	12	T12A1,50	50	8	2	0
A1	13	T13A1,50	50	8	2	0
A1	14	T14A1,50	50	9	5	4
A1	15	T15A1,50	50	10	5	2
A1	16	T16A1,50	50	10	1	1
A1	17	T17A1,50	50	7	1	0
A1	18	T18A1,50	50	10	5	1
A1	19	T19A1,50	50	8	6	2
A1	20	T20A1,50	50	10	4	3
A1	21	T21A1,50	50	8	2	1
			Totals	186	60	33

Table 8: Asset count for each distribution transformer on phase *a*

Phase & Circuit	Xfm. #	Xfm. ID	kVA	# Homes	# PVs	# EVs
B2	22	T22B2,25	25	3	0	1
B2	23	T23B2,50	50	7	0	0
B2	24	T24B2,75	75	11	4	4
B2	25	T25B2,50	50	7	3	2
B2	26	T26B2,50	50	8	3	1
B2	27	T27B2,50	50	8	5	3
B2	28	T28B2,50	50	7	1	0
B2	29	T29B2,50	50	7	5	3
B2	30	T30B2,50	50	7	4	3
B2	31	T31B2,50	50	10	6	4
B2	32	T32B2,50	50	8	4	5
B2	33	T33B2,50	50	8	1	0
B2	34	T34B2,50	50	8	1	1
B2	35	T35B2,50	50	5	1	2
B2	36	T36B2,50	50	4	1	0
B2	37	T37B2,100	100	10	1	0
B2	38	T38B2,75	75	9	2	2
			Totals	127	42	31

Phase & Circuit	Xfm. #	Xfm. ID	kVA	# Homes	# PVs	# EVs
B4	39	T61B4,50	50	7	1	1
B4	40	T62B4,50	50	7	1	0
B4	41	T63B4,50	50	6	0	0
B4	42	T64B4,50	50	10	1	1
B4	43	T65B4,50	50	8	0	1
B4	44	T66B4,50	50	6	1	0
B4	45	T67B4,50	50	6	1	0
B4	46	T68B4,50	50	6	3	1
B4	47	T69B4,50	50	7	2	2
B4	48	T70B4,50	50	8	5	1
B4	49	T71B4,25	25	5	2	2
B4	50	T72B4,25	25	4	2	1
B4	51	T73B4,50	50	4	2	0
B4	52	T74B4,50	50	7	3	2
B4	53	T75B4,50	50	10	3	2
B4	54	T76B4,25	25	4	0	0
B4	55	T77B4,25	25	5	2	0
B4	56	T78B4,25	25	1	0	0
B4	57	T79B4,50	50	10	3	0
B4	58	T80B4,50	50	10	3	1
B4	59	T81B4,50	50	10	3	3
B4	60	T82B4,50	50	10	3	1
B4	61	T83B4,50	50	10	1	1
B4	62	T84B4,50	50	8	1	1
B4	63	T85B4,50	50	10	0	0
B4	64	T86B4,75	75	10	0	0
B4	65	T87B4,50	50	6	1	1
B4	66	T88B4,75	75	11	0	1
			Totals	206	44	23

Table 9: Asset count for each distribution transformer on phase *b*

Phase & Circuit	Xfm. #	Xfm. ID	kVA	# Homes	# PVs	# EVs
C3	67	T39C3,75	75	9	1	1
C3	68	T40C3,75	75	11	0	1
C3	69	T41C3,50	50	7	5	1
C3	70	T42C3,50	50	10	3	1
C3	71	T43C3,50	50	8	1	0
C3	72	T44C3,75	75	12	1	1
C3	73	T45C3,50	50	2	0	0
C3	74	T46C3,50	50	11	1	2
C3	75	T47C3,50	50	5	4	2
C3	76	T48C3,50	50	7	1	0
C3	77	T49C3,50	50	4	0	0
C3	78	T50C3,100	100	11	2	0
C3	79	T51C3,75	75	4	0	0
C3	80	T52C3,50	50	3	0	0
C3	81	T53C3,167	167	8	2	1
C3	82	T54C3,50	50	10	2	1
C3	83	T55C3,50	50	10	3	1
C3	84	T56C3,75	75	7	1	0
C3	85	T57C3,50	50	8	1	1
C3	86	T58C3,50	50	7	1	1
C3	87	T59C3,50	50	5	1	1
C3	88	T60C3,50	50	6	1	1
			Totals	165	31	16

Phase & Circuit	Xfm. #	Xfm. ID	kVA	# Homes	# PVs	# EVs
C5	89	T89C5,75	75	10	0	2
C5	90	T90C5,50	50	8	0	1
C5	91	T91C5,50	50	8	0	0
C5	92	T92C5,50	50	9	1	0
C5	93	T93C5,50	50	8	0	0
C5	94	T94C5,50	50	8	0	0
			Totals	51	1	3

Table 10: Asset count for each distribution transformer on phase *c*

Moreover, the *total* assets in Mueller are listed in Table 11. Home and PV data, recorded in 1-minute intervals, are downloaded from Pecan Street's consumer energy data center. Data for EVs is generated by randomizing uncorrelated charging. Cable parameters are estimated based on cable length and type, and distribution transformer parameters are provided by Austin Energy.

Type	Count
Homes	735
Photovoltaic Arrays	178
Electric Vehicles	106
Cables	98
Distribution Transformers	94

Table 11: Total asset count

MATLAB/SIMULINK MODEL

Modeling of Mueller's electrical distribution system was realized via power apparatus models from the *SimPowerSystems* blocket in *MATLAB/Simulink*. Collected data from Pecan Street is combined with the model in order to assess the state of the distribution system under existing conditions. With confidence developed from this effort, predictions of operation under other scenarios can be performed. Use of real data promotes confidence in the results, as it accounts for the effects of un-correlated load behavior and intermittent weather conditions pertinent to the geographical area under consideration.

An example of the data, which is used as inputs to the Mueller distribution system computer model, is shown in Fig. 16. For the day shown, consumption peaks near 6 kW, while generation near 5 kW. The recurring pulses in consumption behavior are attributed

to air conditioning units cycling on and off. Additionally, PV generation is only available during daylight hours and is susceptible to fluctuations due to cloud passages. Since power factor is not recorded by the installed equipment, at each time step of the simulation the power factor is estimated from [74]:

$$PF = \frac{I_1}{I_T}\cos\varphi = \frac{\cos\varphi}{\sqrt{1+THD^2}} \tag{34}$$

where

PF = power factor

I_1 = fundamental current [rms Amps]

I_T = total line current [rms Amps]

THD = total harmonic distortion

φ = displacement angle between 240 V phasor and I_1

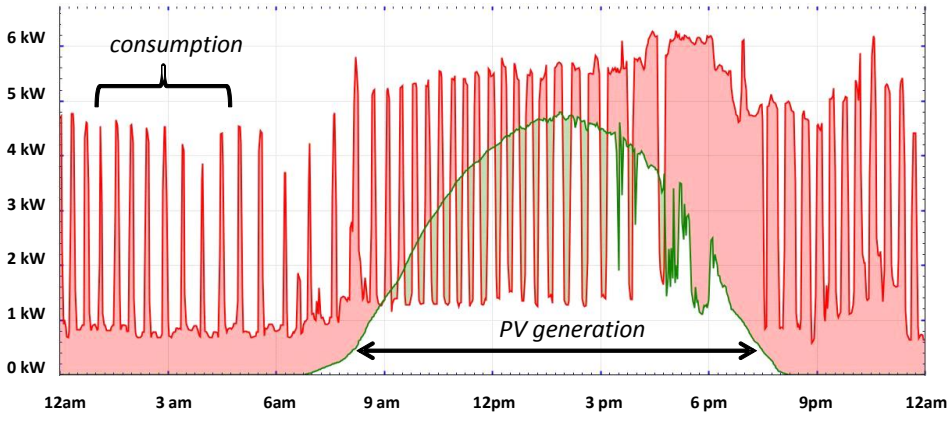

Figure 16: Household power consumption and PV generation in 1-minute intervals for a single home at Mueller. (Source: Pecan Street, Inc.)

The developed computer model, shown in Fig. 17, accepts the above data and estimates voltage, current, power, power factor, and energy usage everywhere else in the network. This model is consistent with one-line diagram in Fig. 15, where three-phase cables emanate from both substations and terminate at the switchgear boxes. Single-phase cables from the switchgear boxes then provide service along the five circuits shown in red (phase *a*), blue (phase *b*), and green (phase *c*).

The secondary network load in the model, which includes all homes, PVs, and EVs behind the respective transformers, is lumped as an aggragate load for each transformer because detailed modeling of the seondary network is of little benefit and would significantly increase computational time. The aggregation of load is accomplished by combining the power profiles provided by Pecan Street; that is, residential consumptions and EV charging are summed, and PV generation is subtracted from this sum.

The effects of the steadfast growth and integration of PV and EV assets can range from changes in voltage profiles [75], to impact on transformer life, to significant changes in power factor. The ensuing discussions will assess the effects of these resources and will consider if their associated topologies can be feasibly retrofitted to a microgrid. By combining actual recorded data from individual field-metered sources and loads with a computer model of the distribution system, it is possible to understand how solar intermittency and load variations affect the distribution system. Fundamentally, this approach takes advantage of the additional timely data available about the distribution system to gain an improved insight into the system from the substation to the loads.

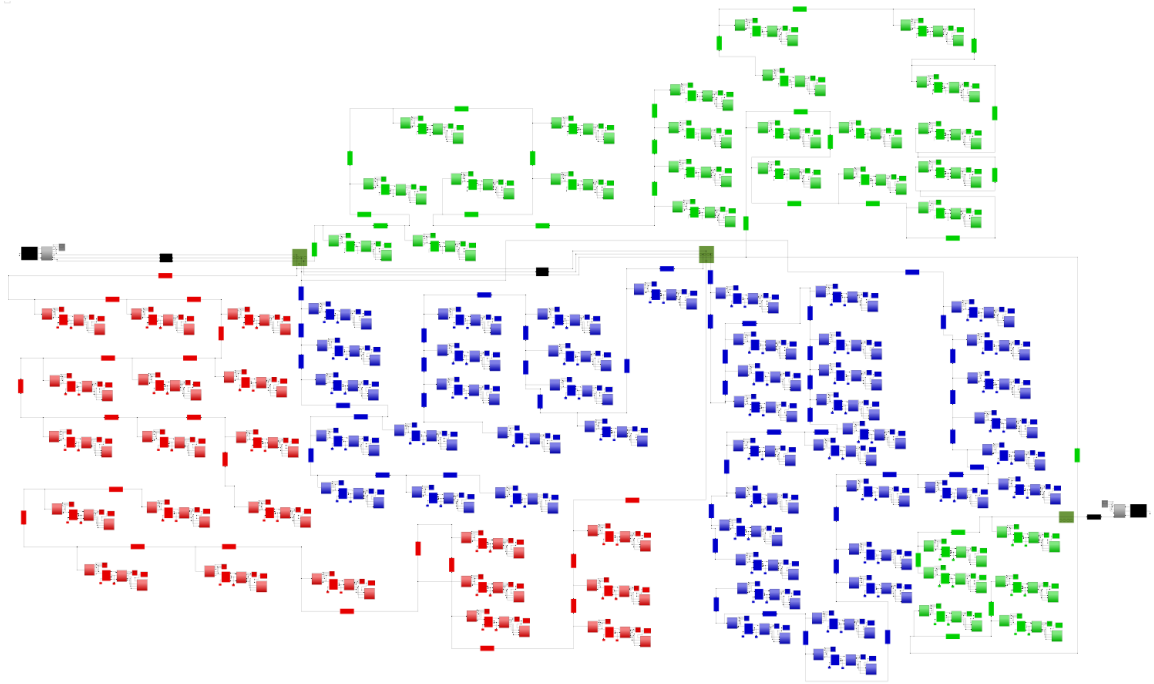

Figure 17: Computer model of the Mueller distribution system created in *MATLAB/Simulink*

ANALYSIS

Residential Load

Figure 18 shows the power consumption profiles of each of the 735 homes. These profiles exclude EV charging and PV generation. Explanations of each view in the figure are as follows:

Figure 18(a) shows the active power consumption (kW) of each of the homes over a 24-hour period. The data is graphed using a mesh grid to produce a 3-D surface plot. The color map corresponding to this surface appears on the right side of the figure, where power consumptions > 10 kW appear in increasingly-dark red color. The advantage of this view is that it permits detecting correlation in consumption behavior by observing the

peaks and the valleys on the surface. For example, in the encircled areas of this view, each area encloses a different group of homes at similar times of the day (~12 PM through 12 AM). The top circle encloses several residences exceeding 10 kW (simultaneously) while the lower circle encompasses other residences going through consumption valley below 4 kW (during the same times of the day). The data highlights the fact that residential loads are heterogeneous and their individual behavior is difficult to predict. However, larger scale averages tend to be consistent.

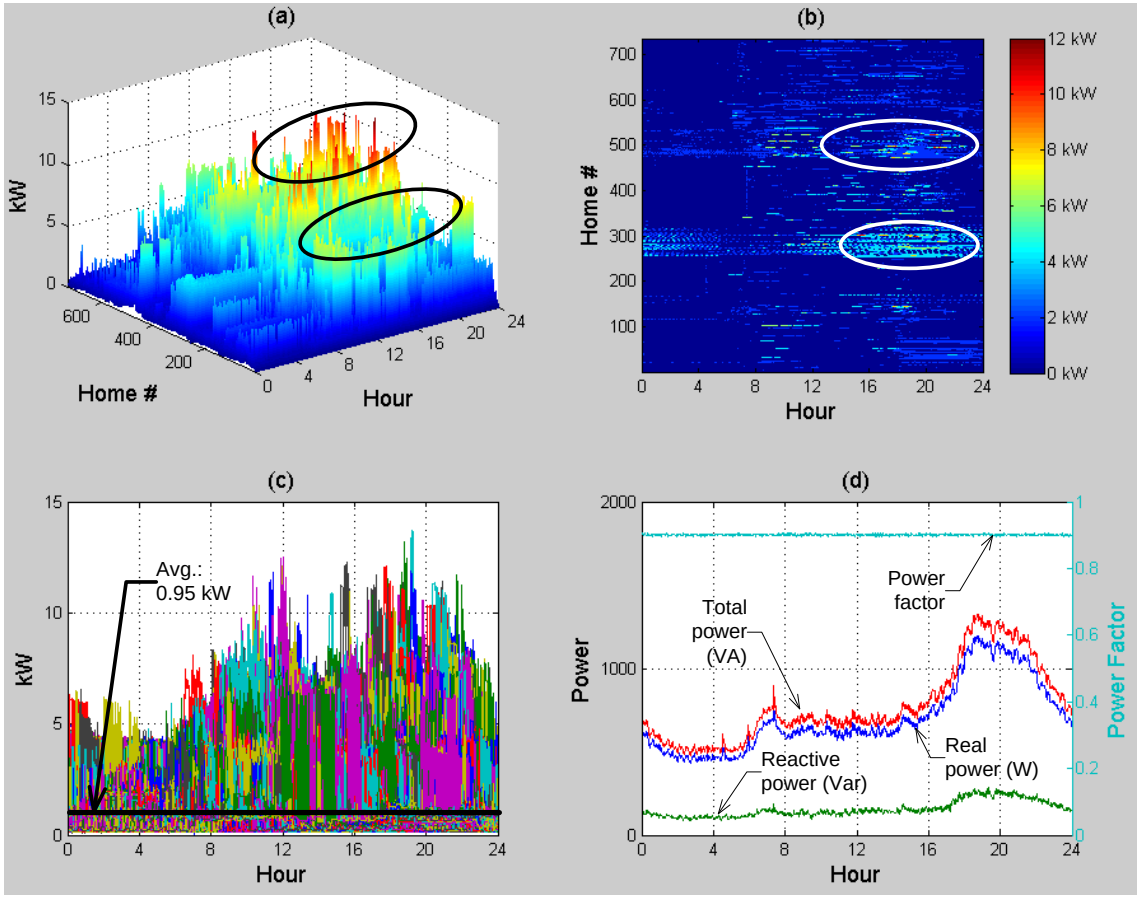

Figure 18: Residential demand for 735 Mueller residences in a 24-hour period

Figure 18(b) is convenient for showing load durations. For example, referring to the encircled areas corresponding to view (a), the 10 kW peaks do not last long. Similarly, the lower encircled area, in this view, shows that the valleys of ~4-5 kW last much longer than the 8-12 kW peaks do. Additionally, not all homes incur such peaks; only some do which is clearly noticeable from this type of view. Also, the dominant color on this contour plot is dark blue which suggests that, most of the time, the residential consumption is near 2 kW.

Figure 18(c) shows the home consumptions as seen from the time-kW plane. Although it is commonly expected that residential loads generally behave in unison in the evening hours, this view of the 735 different load shapes suggests there is little correlation in residential load patterns. It can be observed that the peaks and valleys of different homes are not necessarily aligned. Each home behaves independently of the others, with peak power consumptions occurring in the middle of the day, in the evening, or not occurring at all. This behavior is desirable for electric utilities because transformer loading tends to be closer to an average than to the sum of the peak demands. This shows that any pricing or other signals that tend to correlate demand may result in an adverse effect on transformer life, because it stimulates longer operating times at higher temperatures [76]. It is also interesting to note that the *average* consumption over 24 hours for the 735 homes (computed in time intervals of one minute) is 0.95 kW. This value is not predicted, modeled, made up, or based on the consumption of a few homes. Instead, this value was computed from actual recorded data in one-minute intervals which raises confidence in the results. However, this average value varies by day of the week, time of the year, and is not general.

Figure 18(d) exhibits the aggregated (sum) power consumption of all homes and approximates the total demand (excluding EVs, PV systems, and distribution power

losses) as seen from the lateral service entrance. The power factor, which refers to *displacement* power factor rather than *total* power factor [77], is plotted against the right-side axis which is approximately 0.9. As noticed from the real and total power traces, the peak power demand occurs in the evening (as expected). In contrast to view (c), which is shown at the individual home level, at the lateral level the power consumption profile is repeatable, predictable and—ironically—composed of unpredictable, uncorrelated home consumption profiles. As recognized from the peak total power, the peak load of this community varies between 1 and 1.5 MVA, and also varies by day of the week and time of the year.

PV Generation

Figure 19 shows the generation profiles of roof-mounted, residential PV arrays. These grid-tied residential PV systems only produce active power [78, 79], and not reactive power [16, 80]. This contributes to low power factors as seen from the lateral service entrance. The meaning of each of the PV generation views is explained next:

Figure 19(a) shows the individual real power generation output of all PVs as a 3-D surface. The color map corresponding to this surface appears on the right side of the figure, where generation > 4.5 kW is indicated in increasingly-dark red. This view clearly shows that the peak generation of each residential PV system can be similar, but is not the same. The encircled area shows a group of PV systems with irradiance deficiency. Various PV system characteristics, such as rated power, number of cells, connection method, dimensions, cell technology, irradiance based on the sun's azimuth and zenith angles, system efficiency, dynamic variations in atmospheric and environmental air mass, passing clouds inducing whole or scattered shade, and temperature, all affect PV power output. Therefore, not all PV systems are affected similarly by these characteristics due to

their geographical separation. Unequal irradiance due to geographical dispersion highlights an important fact about distributed generation: not all PV systems are affected *simultaneously* by every cloud event; many PVs retain high power outputs while many others do not. This lack of correlation is advantageous in terms of voltage stability [81] when compared to concentrated PV plants [19, 80].

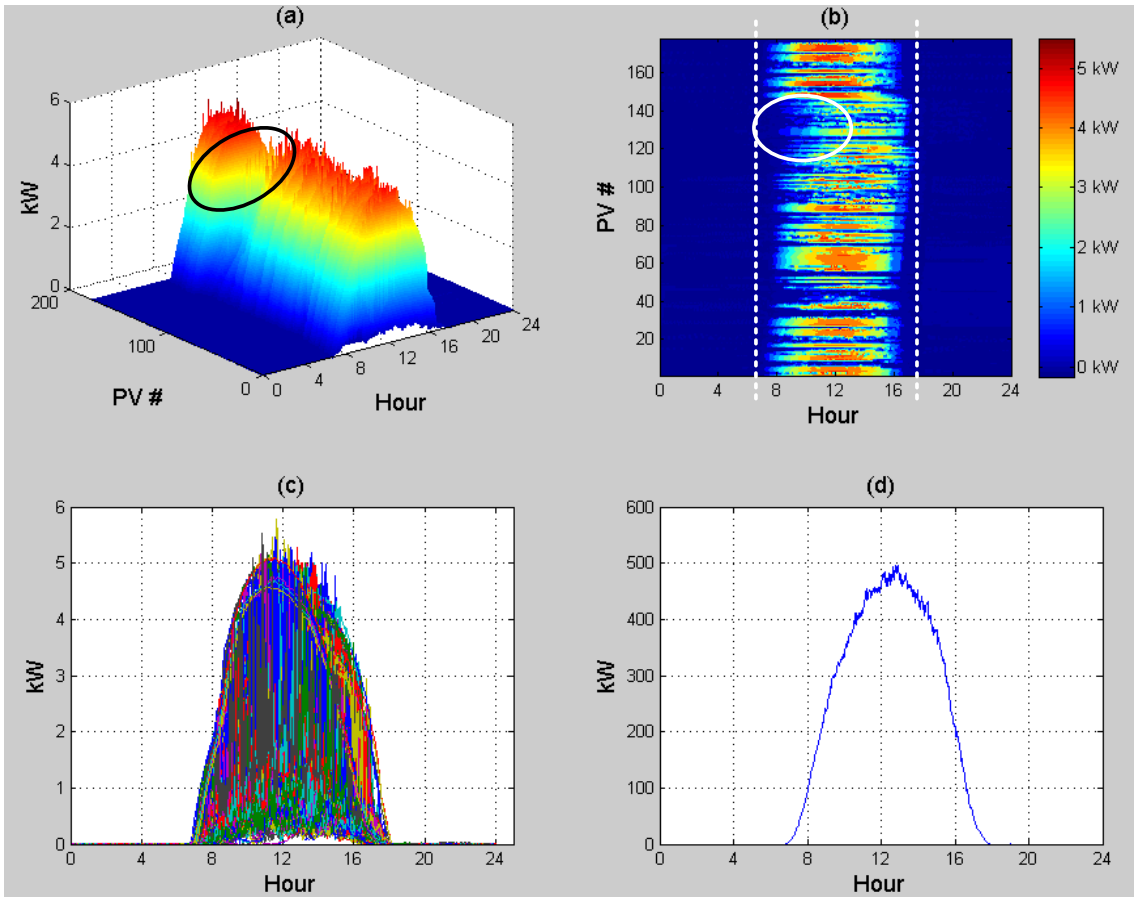

Figure 19: PV generation for all 178 PVs in a 24-hour period

Figure 19(b) shows data in view (a) as seen from the 'top', where the encircled areas show the duration of the aforementioned irradiance deficiencies (6-11 AM). This view also helps in counting the number of PVs affected by this deficiency (PV #120 through #140). Another advantage of this view is that it permits comparing the generation profiles of south-facing and west-facing PV arrays. Necessary irradiance reaches south-facing PVs hours before it reaches west-facing PVs. This is opportune for morning loads powered by south-facing PVs, and also indicates that west-facing PVs are more aligned with the early-afternoon and evening loads. The homes at Mueller have either west- or south-facing PV orientations, or a combination of both. The disadvantage of dividing the orientation is reduced available or excess power and the reduced ability to sell this power to the utility; the advantage, however, is wider temporal coverage for its owner and correspondingly less temporal dependence from the utility. Referring to the color map on the right, the predominant output power of the PVs is closer to 4 kW than it is to 5 kW. This indicates that PV systems spend more time producing power at shoulder output levels rather than at their peak output.

Figure 19(c) shows the lack of correlation in residential PV generation, which is observed even for PVs in close geographic proximity. If the affected PVs are in physical proximity, they will reduce their output in unison to cloud passage. An advantage of having recorded PV data is that intermittency, due to cloud-passage, is not required as part of a model to observe these effects. Instead, these PV power profiles are injected directly into the computer model, which not only elevates confidence, but it also allows examining the voltage profiles in other parts of the network.

Figure 19(d) shows the aggregate residential PV power generation. Although the individual PV power generation is intermittent and uncorrelated (as shown in the previous view), at the aggregate level, the generation follows a predictable smooth

envelope that reaches nearly 0.5 MW per day. The aggregate generation, however, is less than the total residential load shown in Fig. 18(d). This result indicates that, while this community has a high density of PV generation, no excess PV power leaves the community through the lateral service entrance. Instead, the generated PV power remains inside the community and is consumed as billable energy (kWh) by homes not equipped with such arrays.

Electric Vehicles

Figure 20 shows the charging profiles for 106 plug-in Chevy Volts. The charging profiles include a realistic mix of 120 and 240 V charging profiles. These data are for actual charging profiles, but the analysis was done prior to large scale installation at homes. To predict the effect of the full set, the 106 vehicles were assigned to the homes of consumers expecting to acquire an electric vehicle. In addition, the state of charge at the onset of the charging process was randomized, and the starting time for a charge was randomized between 4 and 8 PM. The following analysis is an example of using the model to project the effect of changes in load.

Figure 20(a) demonstrates the load consumption of all EVs using a surface plot. The peaks of the curve indicate groups of vehicles charging at 240 V; the lower peaks represent EVs charging at 120 V. The mix of high and low peaks is a direct result of randomizing the charging profile levels. The vehicles charging at 240 V appear in red, which corresponds to charging levels of 3.3 kW. The lower peaks corresponding to 120 V appear in cyan and indicate a charging level of 1.44 kW. There is also a set of vehicles that charge at 0.96 kW, and appear as light blue peaks. As previously mentioned, the plug-in times were randomized to reflect typical behavior in a residential neighborhood. The starting-charge time was constrained between 4-8 PM for two reasons. First, to

exacerbate evening-time charging and assess the potential impact this has on the distribution transformers. Second, plug-in times after 4 PM reduce electrical overlap with PVs.

Figure 20(b) highlights the assumed EV charging assumptions by showing charge time spans. These time spans indicate how long each vehicle charges from a random level of state-of-charge at plug-in time. Some vehicles charge overnight and into the early morning hours as shown by the encircled area. These vehicles charge at 120 V, at either 0.96 kW or 1.44 kW. The short time spans shown in this view represent both 240 V charging (≤ 3.5 hours) and 120 V charging (≤ 9 hours). In the 120 V case, short time spans represent vehicles with a higher state-of-charge at plug-in time.

Figure 20(c) shows *some* un-correlation in EV charging, but not as much as in the residential consumption or PV generation since the EV charging plug-in time was set between 4-8 PM. Uncorrelated charging is desirable from the utility stand-point as it circumvents sizing transformers linearly with the expected number of EVs. The benefit of uncorrelated power demand is not new; it has been observed for decades in residential air-conditioner usage: many units operate simultaneously, while many do not. The time spans in this view are further annotated with labels showing the three possible charging levels for these EVs, and their maximum (not actual) charging duration. It is noted that 240 V charging requires level-2 chargers with a stand-alone 240 V feeder circuit inside a residence.

Figure 20(d) conveys the total EV charging load at the lateral level based on the assumed charging profile. A noticeable EV impact occurs between 6-8 PM and appears to be < 200 kW for a typical day. This forecast is strongly dependent on the degree of correlation included in the model. The risk of charging too many EVs from a single distribution transformer depends on the assumed transformer sizes, number of EVs per

transformer [82, 83], and charging levels. The transformers at Mueller appear to be sized adequately enough to be able to meet the load incurred by the Chevy Volts.

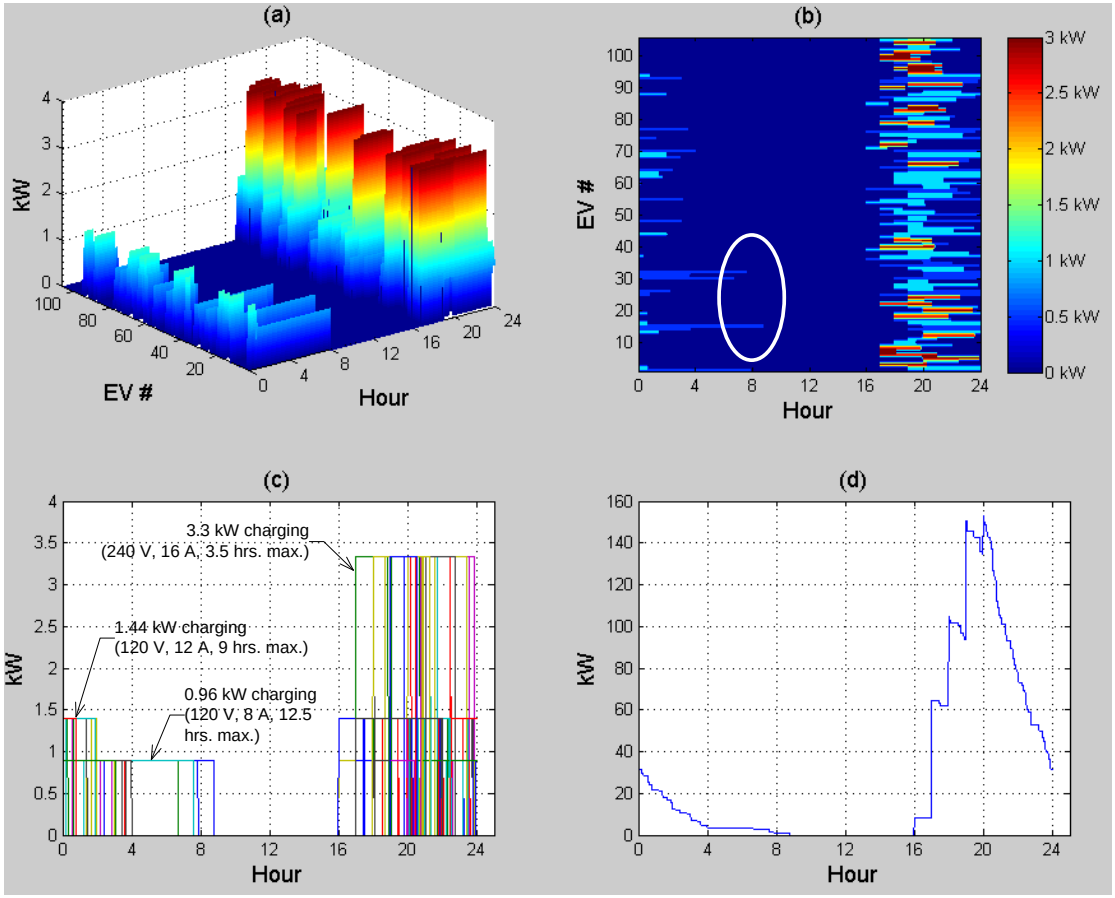

Figure 20: Charging profiles of all 106 electric vehicles (Chevy Volts) in a 24-hour period

Transformer Voltage Profiles

A particular consideration arising from widely deployed PV resources is to ensure that voltage levels are maintained within appropriate limits. The voltage supplied to consumers is an important metric as it indicates the service quality: a satisfactory voltage level is required for equipment such as lights and appliances in order to prevent

inadequate operational characteristics. Higher voltage levels are undesirable because not only may they reduce equipment lifetime, but they may also increase power consumption without providing any noticeable improvement in performance. A voltage rise is to be expected when power is injected into a distribution system from the load side. This occurs because voltage drops along the power lines are reduced. Hence, it is possible that individual residential-scale PV systems adversely affect the voltage levels of other consumers.

The impact that PV arrays have on transformers' primary-side voltage profiles in the Muller distribution system is depicted in Fig. 21(a) and Fig. 21(b). Although a voltage rise noticeably coincides with PV generation, voltage levels nevertheless satisfy the criteria prescribed by [84] in that they are within ±5% of nominal voltage (7.2 kV line-to-ground), and, therefore, do not warrant concern from a utility perspective. Furthermore, it is observed that EVs lower the voltage during evening hours, although the situation appears to be of minimal, if any, significance.

The secondary-side voltage profiles is shown in Figure 21(c) which shows that PVs produce voltage swells above 1.0 pu (on a 240 V base) for several transformers during diurnal hours; however, this voltage swell is minor. The dominant color in this contour representation is yellow, which indicates that most transformers (most of the time) operate at values near 240 V. The encircled regions show the times of the day where the transformer voltages are highest. Voltages greater than 1.0 pu are due to PVs producing localized power, which reduces transformer through current and voltage drops. Similarly, the darker regions in this plot correspond to lower voltages due to EV charging.

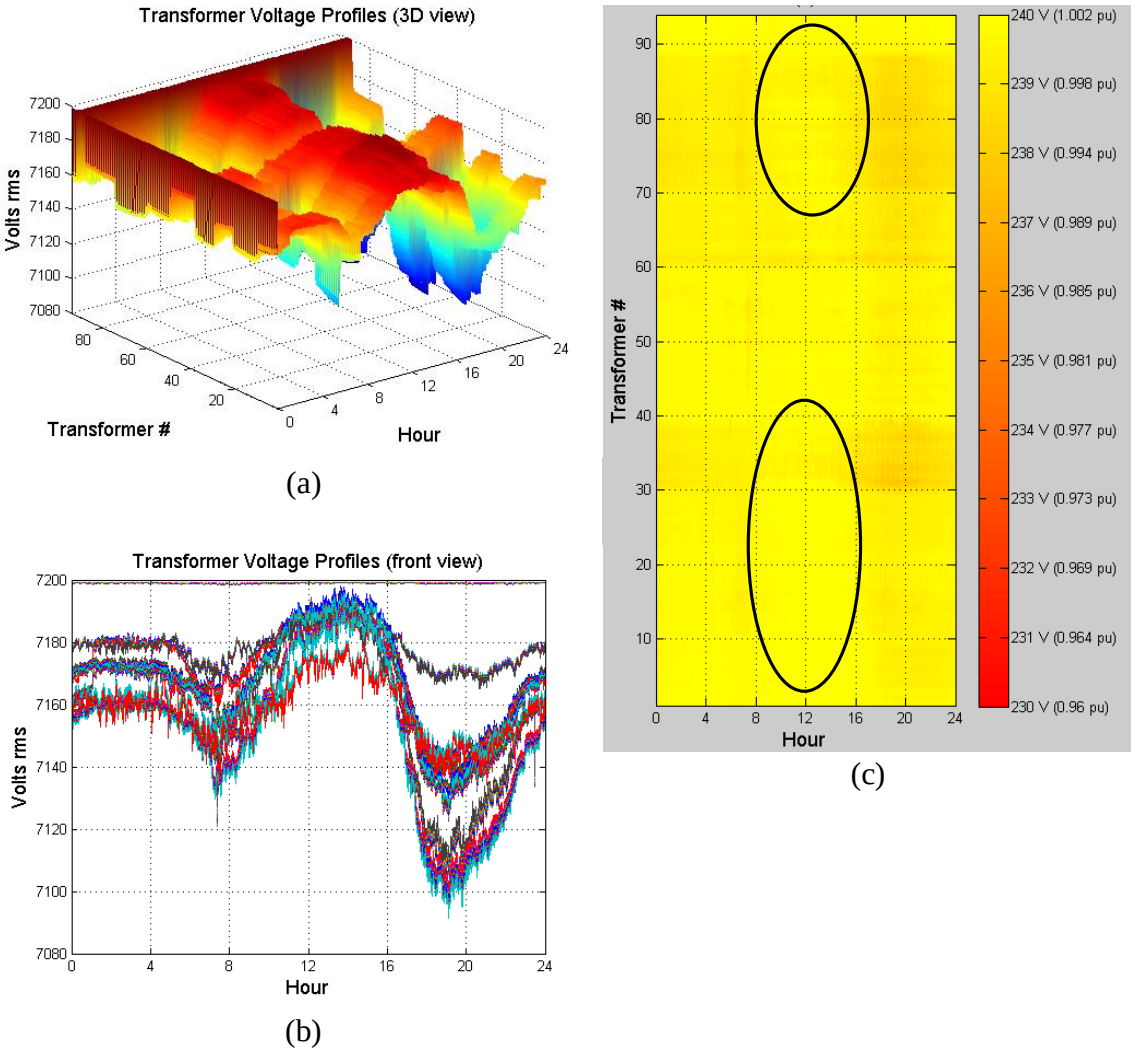

Figure 21: Primary (left) and secondary (right) transformer voltage profiles

Conservation Voltage Reduction

Within recent years, the desire to curtail peak demand and end-use energy consumption has motivated many electric utilities to consider cost-effective practices for electric energy conservation. One commonly used strategy, known as conservation voltage reduction (CVR), operates on the principle that a reduction in substation voltage leads to a reduction in feeder load demand. To achieve this, substation voltage regulating

equipment such as load tap changing (LTC) transformers are calibrated so that distribution system voltages—most critically, the most distant service drop—are maintained at a minimum acceptable voltage level.

The acceptable voltage range depicted in Fig. 22 has upper and lower limits of 126 V and 114 V, respectively, for residential systems [84]. Because violating this voltage range may be harmful to consumer equipment, regulation of end-use service voltage is deemed crucial.

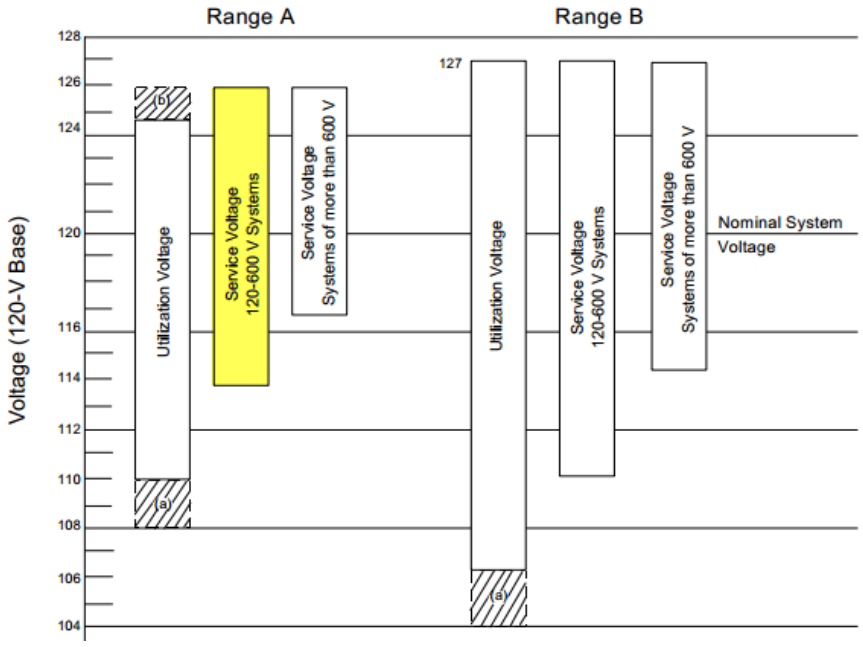

Figure 22: Voltage range for residential systems

Implementation of CVR is typically augmented with line drop compensation (LDC), where the voltage at the last customer location is maintained near the allowable minimum of 114 V, while the rest of the voltages along the feeder are allowed to vary based on load conditions. This opposes the conventional practice of setting the voltage at

the first customer location to a value near the allowable maximum so that, after the effect of voltage drops, the voltage at the last customer location is somewhat less—but not necessarily minimum. The acceptance and adoption of CVR throughout the years has prompted several studies [85-90] to evaluate its implicated benefits.

The Snohomish County public utility district engaged in a pilot project [87] years ago to investigate the benefits of CVR and found that energy savings are indeed achieved, although the savings are highly variable from circuit-to-circuit, depending on factors such as feeder length and voltage level, consumer sector (residential, commercial, industrial), and load type (constant impedance, constant power). The effect of CVR on system losses was also determined to be generally favorable due to improvements in distribution transformer efficiency.

Bonneville Power Administration, which serves approximately 150 utilities, sponsored a study [85, 86] to raise awareness for economically attractive conservation resources, where a methodology was developed to estimate supply curves relating energy savings to implementation costs for a hypothetical region-wide CVR program.

Another study [88, 89] substantiated the benefits of implementing CVR at Commonwealth Edison, where energy savings ranged from (depending on consumer sector) 0.41%-0.99% per each percentage reduction in voltage. Energy savings, it contended, were achieved without causing any undue harm or inconvenience to customers.

Furthermore, the application of capacitors for maximizing the benefits of CVR were analyzed in [90], particularly for circuits that experience a significant voltage drop. Because some circuits may not have a relatively flat voltage profile at full load, the use of capacitors is recommended prior to implementing CVR so that benefits are maximized.

In the wake of increased integration of distributed generation resources, the justification of CVR has been subject to scrutiny. The injection of power from load-side distributed generators results in a voltage rise that seems to interfere with the very notion of the CVR control scheme. This consideration is a topic of growing interest and one that is addressed in [91] via simulations carried out on the IEEE 13-node test feeder using a volt-var control technique. Findings suggest that a 15%-30% penetration level of residential-scale photovoltaic (PV) systems contributes to a voltage rise, but the effect is not significant enough to render CVR impractical.

This work elucidates the effects of distributed PV resources on a hypothetical CVR program in Mueller. It is worth mentioning that this study does not explicitly consider the effect of capacitor banks or of the distribution system upstream and downstream from the Mueller community. That is, although the electrical load at Mueller comprises approximately 5% of the substation transformer's MVA capacity, the analysis presumes a nominal voltage level of 12.47 kV at Mueller's *lateral entrance*. Therefore, the assumption is that LTC operations—and hence voltage adjustments—occur at the lateral entrance rather than at the substation.

The LTC transformer has a total regulation range of $\pm 10\%$ in 32 discrete steps of 5/8%. On a 120 V basis, this translates to a 0.75 V change per step. The end-of-line voltage set point is 114.75 V with a chosen bandwidth of 1.5 V, such that any voltage excursion outside this bandwidth will cause the LTC to take corrective action. Higher bandwidths may be selected if voltage regulation is not critical and there exists a desire to reduce the number of daily tap changes [92]. The analysis will consider the 4 different scenarios presented in Table 12, where 'CVR' corresponds to the aforementioned voltage regulating scheme, and 'no CVR' signifies a 12.47 kV voltage at the lateral entrance.

Case Study	Description
Case 1	no PVs and no CVR
Case 2	PVs and no CVR
Case 3	CVR and no PVs
Case 4	PVs and CVR

Table 12: Case studies for a hypothetical CVR program in Mueller

Significant insight is acquired by visually inspecting the results obtained from the 4 simulated cases listed above. The voltage profiles of all distribution transformers in Mueller, for all 4 cases, are depicted in Fig. 23 in the form of a contour plot, where the data spread is related by a colorbar with range 113-120 V. Figure 23(a) and Fig. 23(b) show that voltage levels in the absence of CVR tend to be near the colorbar's upper limit, i.e., 117-120 V. Figure 23(b) offers contrast to Fig. 23(a) as it shows higher voltage levels during daylight hours due to PV generation. Meanwhile, Figs. 23(c) and 23(d) are represented by entirely different hues, suggesting that voltages are in the 114-116 V range of the colorbar. Again, the impact of PV generation is made obvious in Fig. 23(d) due to the associated voltage rise. Additionally, in Figs. 23(c) and 23(d) LTC operations are detected by taking note of the narrow, vertically-oriented line segments that signify abrupt changes in voltage.

An alternate representation of the voltage profiles is seen in Fig. 24, and similar observations are made. Despite significantly lower voltage levels due to CVR, ANSI limits are not violated, and the end-of-line voltage is regulated successfully.

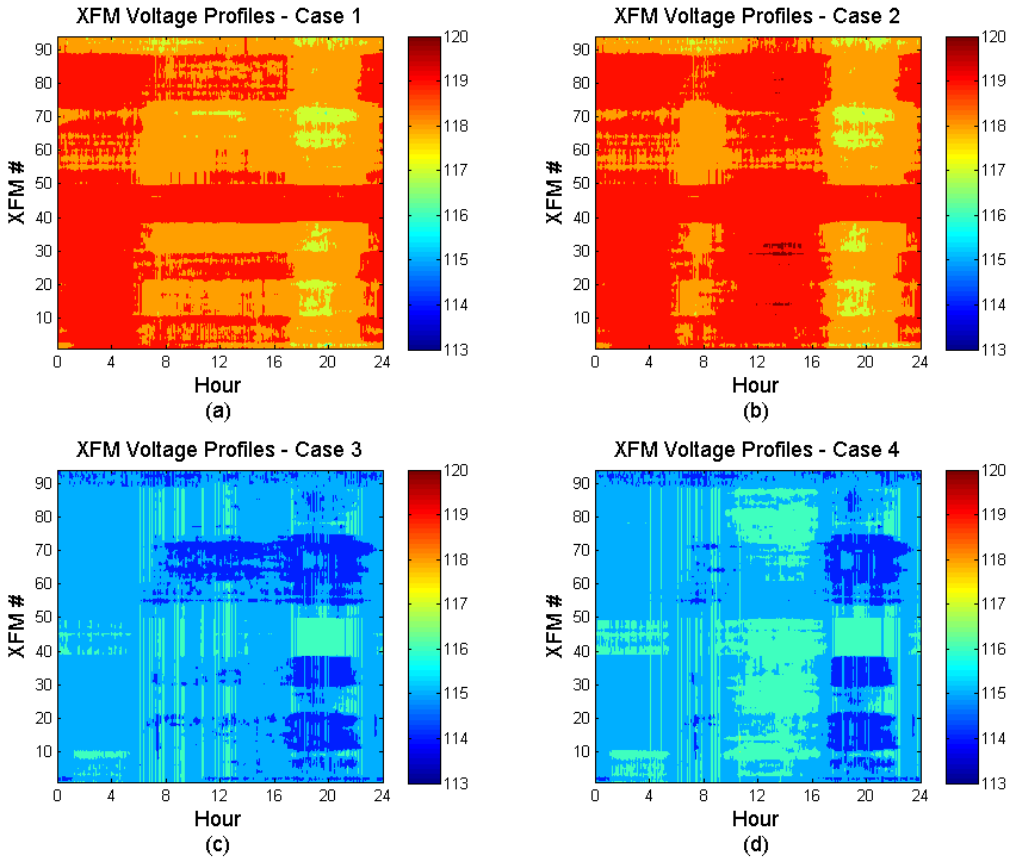

Figure 23: Voltage profiles (top view) of all transformers in Mueller

During times when load demand is high, the LTC takes necessary action to raise the voltage, as seen in Figs. 24(c) and 24(d), with tap change counts of 144 and 130, respectively. Since the load factor of Mueller is somewhat high (i.e., power usage is relatively constant), the number of LTC operations—being as it is a function of load factor and voltage bandwidth—is reasonably low. Furthermore, the effect of PV generation is apparent in Figs. 24(b) and 24(d), with voltage levels peaking at mid-day. The resulting voltage rise of Fig. 24(d) counteracts the underlying intention of CVR,

although, upon first glance, the voltage rise does not appear substantial enough to raise concern or offset potential benefits.

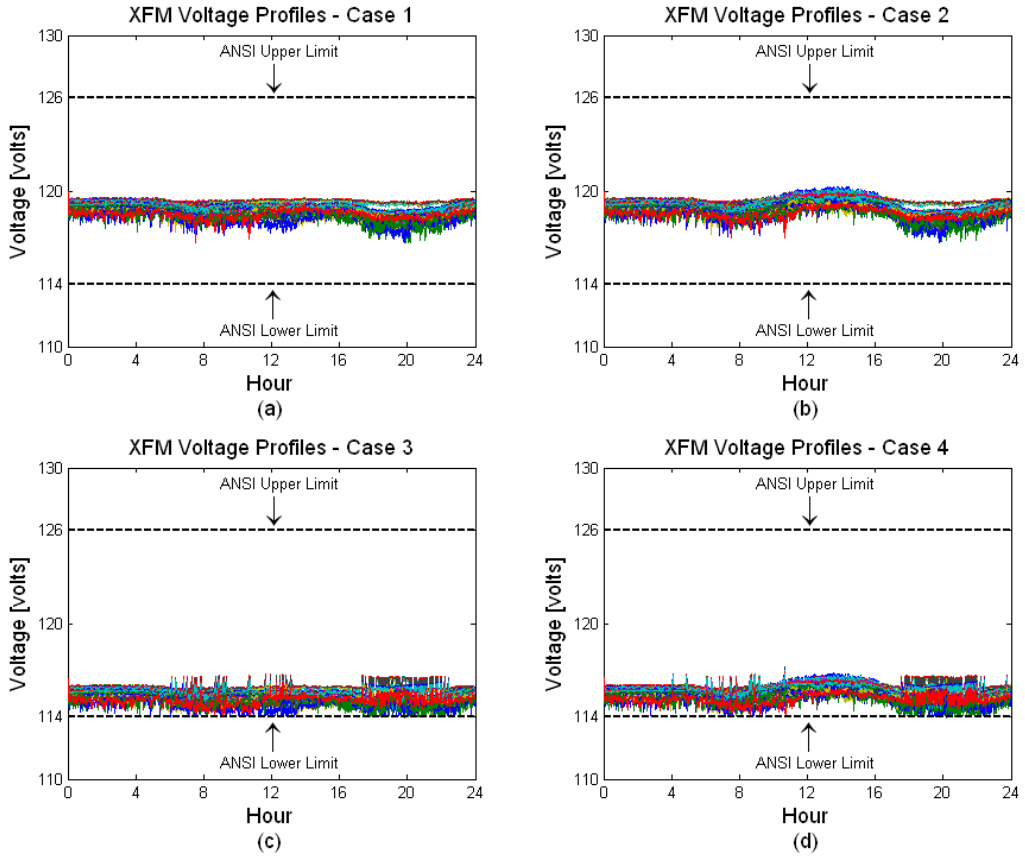

Figure 24: Voltage profiles (front view) of all transformers in Mueller

The active power flow in the Mueller lateral is plotted in Fig. 25 for all 4 cases, in per-unit of 'Case 1'. One immediate observation is that the effect PV generation has on power reduction is much more appreciable than the effect CVR has. That is, in an instantaneous sense, CVR contributes to a power reduction of approximately 3% (Case 1 vs. Case 3) whereas PV generation may reduce power consumption by as much as 80%

(Case 1 vs. Case 2). The most telling observation relates to the impact that load-side PV generation has on CVR (Case 2 vs. Case 4), as savings in power are reduced after sunrise and increased after sunset. Figure 25 effectively reveals that savings in power are reduced since the disparity between Case 2 and Case 4 is minimized during the daylight hours. This interdependence is directly attributed to the voltage rise on the distribution circuits: as the voltage increases, the effectiveness of CVR diminishes.

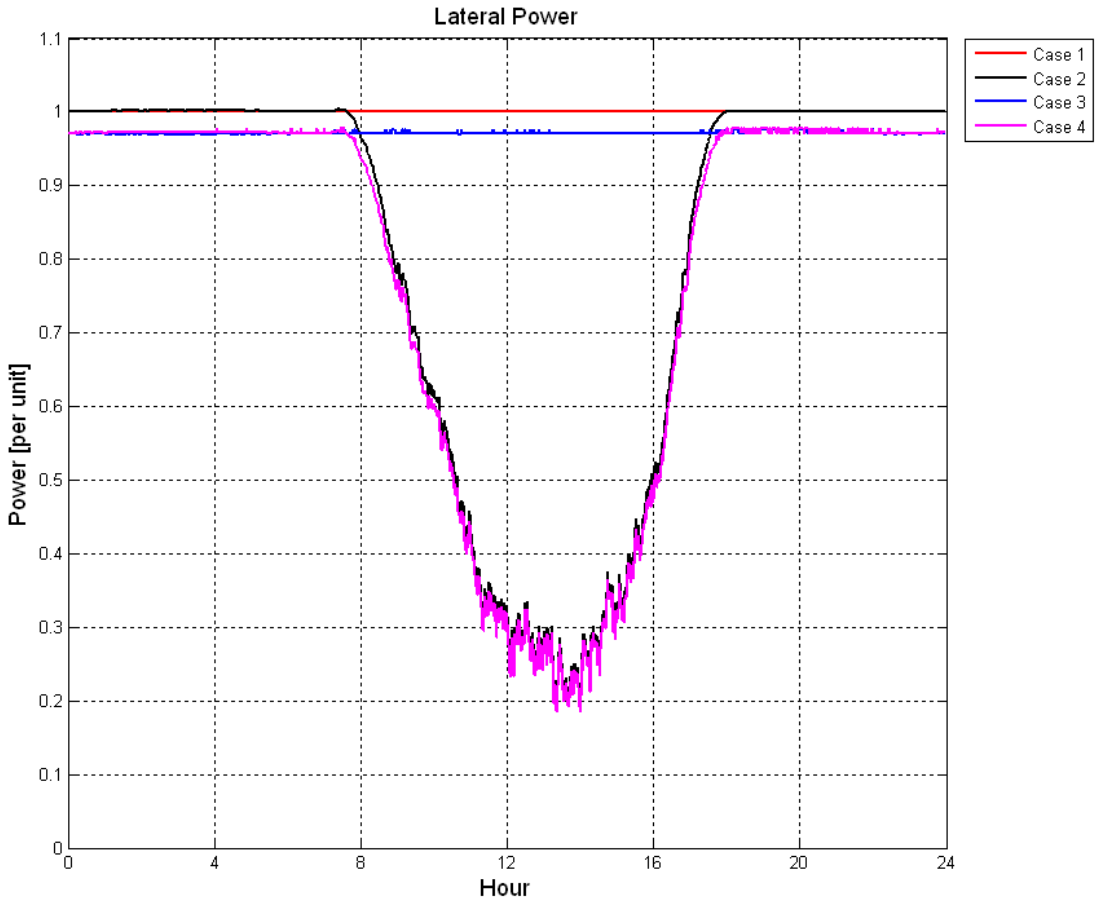

Figure 25: Per-unitized active power in Muller lateral

The abovementioned power, this time in kW and averaged over 24 hours, is depicted in Fig. 26 for each case. It is evident that both PV generation and CVR cause a decrease in lateral power demand, although the impact of the former is greater than that of the latter. In the absence of PV generation, results suggest that an average of 18 kW is saved due to CVR, whereas the savings decline to 14 kW when PV generation is present. Again, this is to be expected as a result of PV power being injected into the distribution system from the load side, causing voltages to swell.

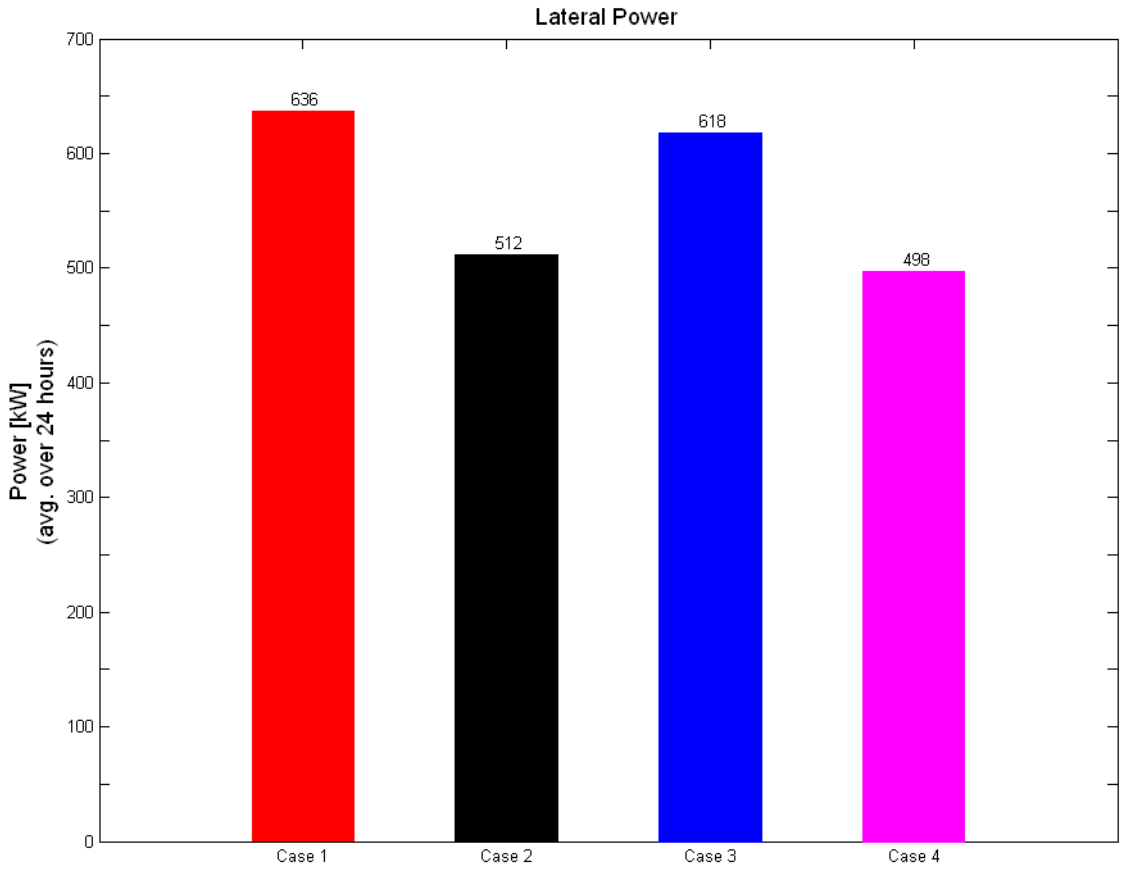

Figure 26: Active power in Mueller lateral averaged over 24 hours

Savings in power and energy between the various cases are compared and plotted in Fig. 27 to gain an understanding of how CVR and PV generation contribute to savings. Savings in power (in kilowatts) are plotted on the left y-axis, while savings in energy (in kilowatt-hours) are plotted on the right y-axis.

The effect of PV generation is revealed in Figs. 27(a) and 27(b) for the non-CVR and CVR scenarios, respectively, and a difference of nearly 90 kWh is observed between them. The benefits of PV generation therefore appear to be *better extracted* when CVR is not implemented; this does not mean, however, that the system would be in a less desirable state if a CVR program were to be implemented together with PVs—or at least in Mueller's case, and given its current penetration level of PV resources. (In fact, from Fig. 25 and Fig. 26 it is apparent that the presence of PV generation together with a CVR program results in the least amount of lateral power.)

In Fig. 27(c), the impact of CVR is illustrated in the absence of PVs, and savings are shown to exceed those of Fig. 27(d), where CVR is implemented together with PV generation. It is observed that PVs appears to interfere with how effectively the benefits of CVR are extracted. Results from Fig. 27(d) indicate that even when PV power generation is at its highest around mid-day, a power reduction of at least 4 kW can still be realized.

It is no surprise that the highest savings are achieved from the condition in Fig. 27(e), as this is the situation where the distribution system evolves from operating at 12.47 kV and without PV generation, to operating at lower voltages with PV generation present.

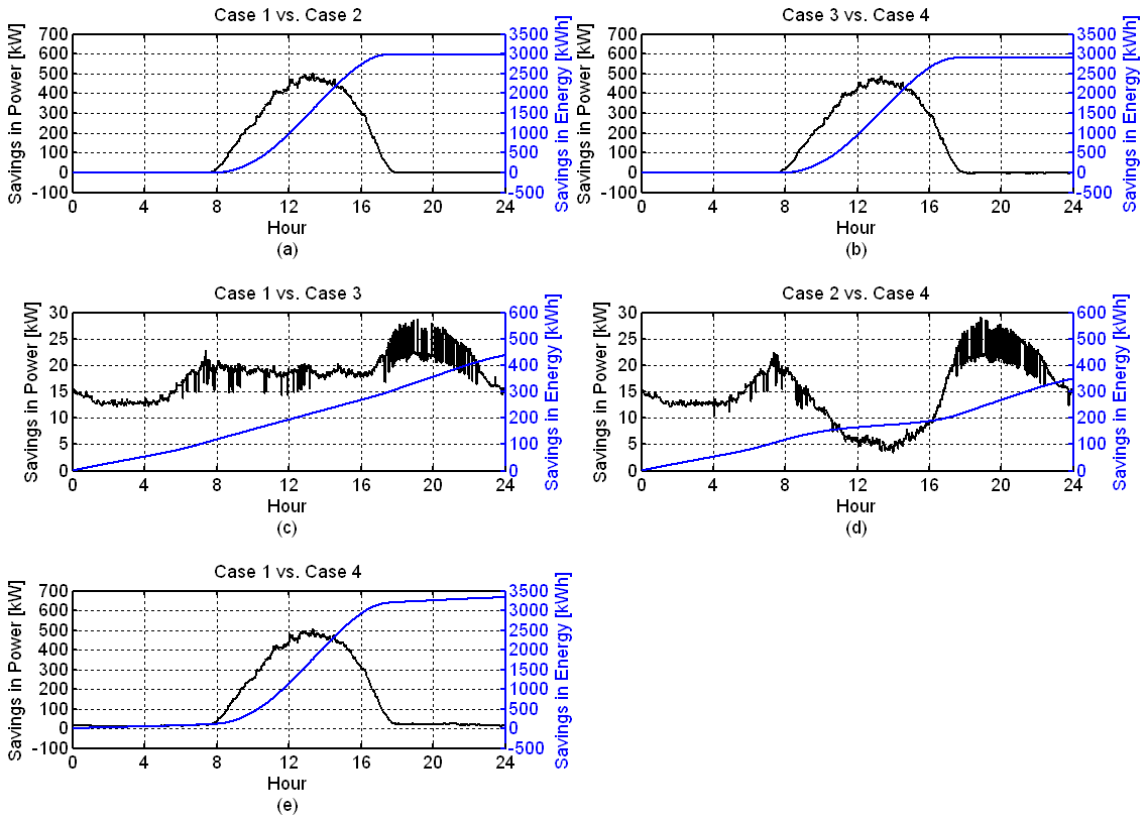

Figure 27: Savings in power and energy

This study assessed the impact of a hypothetical CVR program in the Mueller community, and suggested that a combination of CVR *and* PV generation can lead to the highest reduction of energy consumption; more so than either one of CVR or PV generation alone would. Despite uncertainty about how load-side generation due to distributed PV resources would affect the advantages offered by CVR, this study showed that, for Mueller, even at maximum voltage rise, a 4 kW reduction in power can still be realized. However, the *effectiveness* of CVR is slightly compromised due to PV generation. It is emphasized that the responsiveness of different distribution systems to CVR can vary greatly. If penetration levels of PV resources were higher, not only would

benefits of CVR become increasingly neutralized, but a case could also be made for increased line losses due to excessive reverse power flow. Findings indicated that a sub-nominal operating voltage in Mueller can lead to an average power reduction of 14 kW per hour, which, depending on cost of implementation, may or may not be enticing enough to justify a CVR program.

Voltage Unbalance

An issue deserving attention is the condition wherein the line voltages of a polyphase system are not equal, commonly referred to as a voltage unbalance. Voltage unbalance is primarily caused by the presence of single-phase loads on a three-phase system, particularly when the loads are distributed unevenly among the three phases. Since PV resources generate power on only one phase, they too can affect the balance between the three-phase voltages. Therefore, the combination of existing voltage unbalance in the system due to uneven single-phase load distribution, as well as uneven single-phase PV generation, may contribute to an unacceptably high unbalance: a level specified as 2.5% to 3% or greater per [16] and [84]. The unbalance in voltage is obtained as the maximum deviation from the average of the three-phase line-to-ground voltages divided by the average of the three-phase voltages:

$$V_{unb} = 100 \times \frac{max(dV_a, dV_b, dV_c)}{V_{avg}}\% \tag{35}$$

where

V_{unb} = voltage unbalance

dV_a = deviation of phase *a* voltage from average voltage

dV_b = deviation of phase *b* voltage from average voltage

dV_c = deviation of phase *c* voltage from average voltage

V_{avg} = average of three-phase line-to-ground voltages

In order to prevent problems caused by unbalanced voltages, single-phase loads should be connected evenly across all three phases, i.e., future loads from the highest loaded phase should be planned for the other two phases. Furthermore, PV resources should—ideally—be interconnected to the highest loaded phase; however, utilities do not have the authority over residents to dictate this.

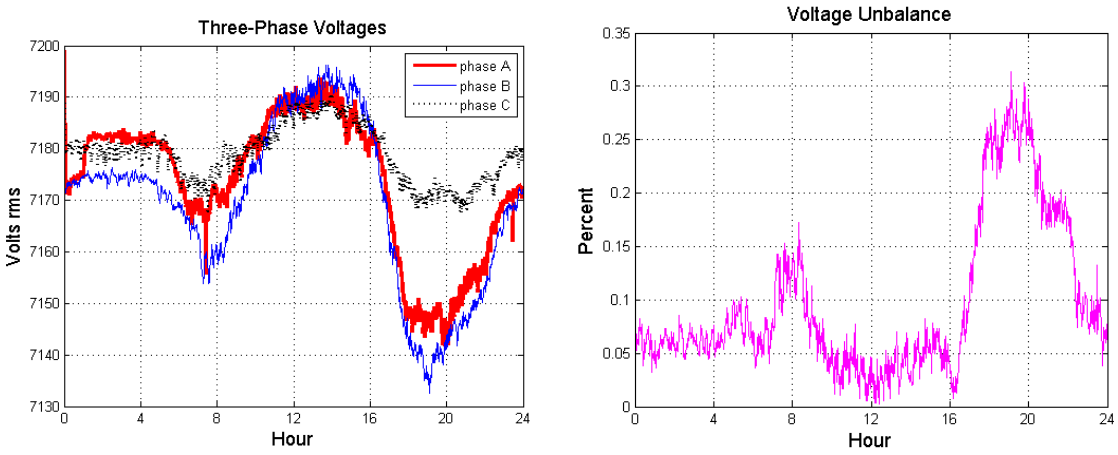

(a) (b)

Figure 28: Voltage unbalance. (a) Three-phase rms voltage at the lateral service entrance. (b) Percent voltage unbalance using ANSI C84.1 definition.

The voltage unbalance observed in the Mueller community is plotted in Fig. 28, which conveys that the unbalance is well within the recommended range despite the high penetration of residential PV generation. This is an observation based on PV systems' relatively low impact on voltage in this neighborhood. (Voltage variations and phase unbalance effects may be more noticeable in "weak" power distribution areas such as in rural communities at the end of long feeders.) Furthermore, it is observed that PVs have a

tendency to *re*-balance the voltages—but not by virtue of active control, but by virtue of decreasing the unbalanced demand instead. That is, the presence of PVs reduces the diurnal unbalance.

Lateral Power Demand

Figure 29 shows the total power consumption of the community, including distribution losses in cables and transformers. As found during the diurnal hours, the power factor experienced by the utility at the lateral serving this community can be reduced to ~0.6 as real power is generated locally by the PV units in the neighborhood. Consistent with this observation is that the reactive power is still provided from the grid. That is, residences rely on the utility for providing reactive power although the utility cannot bill for this service. This has three implications: first, residences cannot become grid-independent unless they can overcome their dependence on reactive power; second, the utility must schedule generation to provide reactive power even though the utility cannot bill the customer for it; third, loads cannot be powered during grid outages—e.g., after natural disasters.

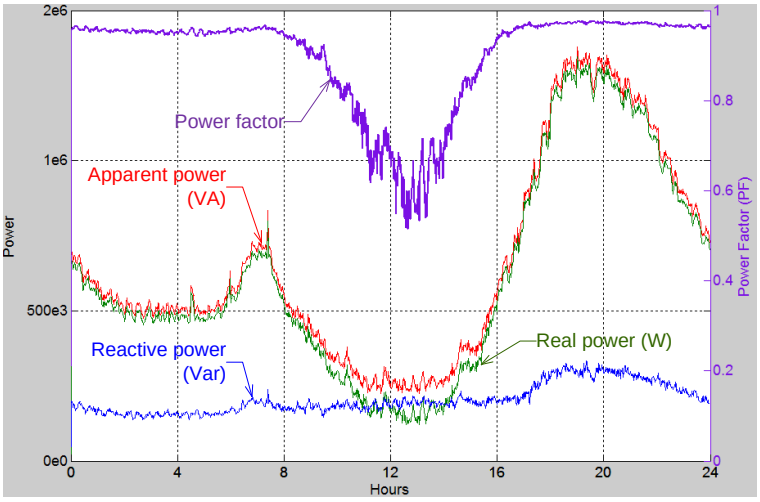

Figure 29: Total power demand as seen from the lateral service entrance

It should also be mentioned that the total PV generation, when observed from the lateral service entrance, is *less* than the power demand. This means that PV generation is *trapped* inside the community and does not leave into the feeder lines. Thus, the impact of PVs is localized to transformers rather than manifested at the circuit, lateral, feeder, or substation levels.

Conversely, at the distribution transformer level, reverse power flow can be experienced by several distribution transformers. When the ratio of PV-to-load is substantial, as observed in Fig. 30, the power generated by the PV arrays exceeds the demanded power; this causes real power to flow in the reverse direction between 10:57 and 14:17 up to a maximum value of 4.45 kW.

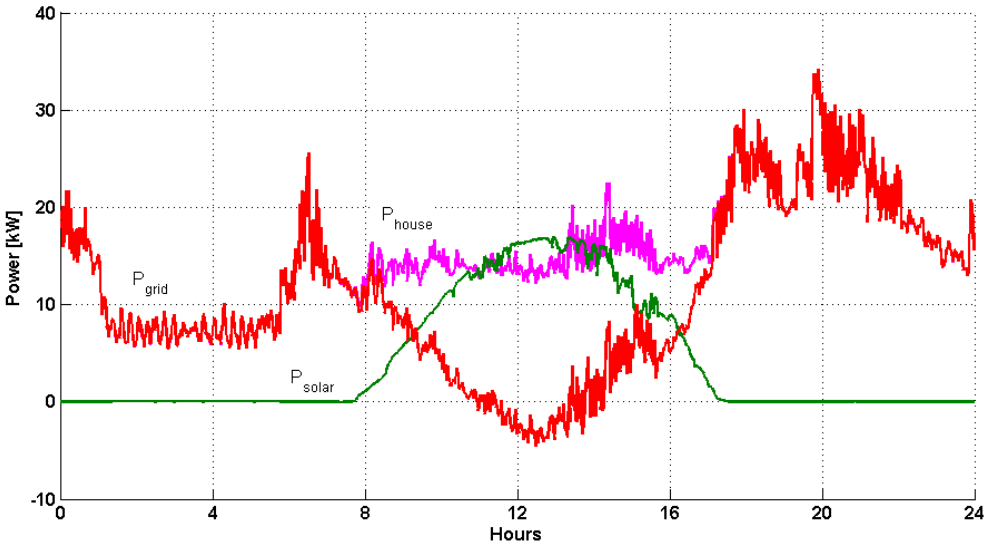

Figure 30: Reverse power flow experienced by a 75 kVA distribution transformer in Mueller serving 10 homes (4 homes with PV arrays)

Transformers

Local utilities often express concern about the fast growth and impact of high penetration levels of PVs and EVs on a single feeder. This concern stems from PV systems' output power dependency on weather conditions and from uncontrolled distributed generation growth and placement, both in terms of electric phase and geographical distribution. The utility's concern also stems from asset management of all grid components, although, in this work, the focus is on the operational state of the distribution transformers. This concern has led to uncertainty in whether transformers were operating at capacity before the installation of PVs and EVs and whether or not replacement or energy storage action is needed in the near term. To address the uncertainty, the following analysis estimates, using the collected data, real power flow experienced by the transformers and reports their estimated operating conditions.

Transformer Net Power Flow

Following the conventions used earlier, Fig. 31 shows the net real-power flow (i.e., forward or reversed) through each of the 94 distribution transformers.

Figure 31(a) shows the net power flow through each transformer, measured looking into the primary-side terminals (in the forward or step-down direction). The transformers are enumerated 1 through 94 in accordance with Tables 8 through 10. As observed from the larger lower encircled area, many transformers experience diurnal reverse (negative) real power flows of -12 kW due to higher PV-to-load ratios. Power reversal is observed on several transformers, but not all; additionally, it depends on the time of day, weather conditions, and number of residents with unused PV capacity. Similarly, the smaller encircled area shows transformers experiencing peak loads of ~40 kW in the evening hours. This view, similar to view (a) of the residential consumption, helps identify similar behavior in transformers via swells and sags in the surface.

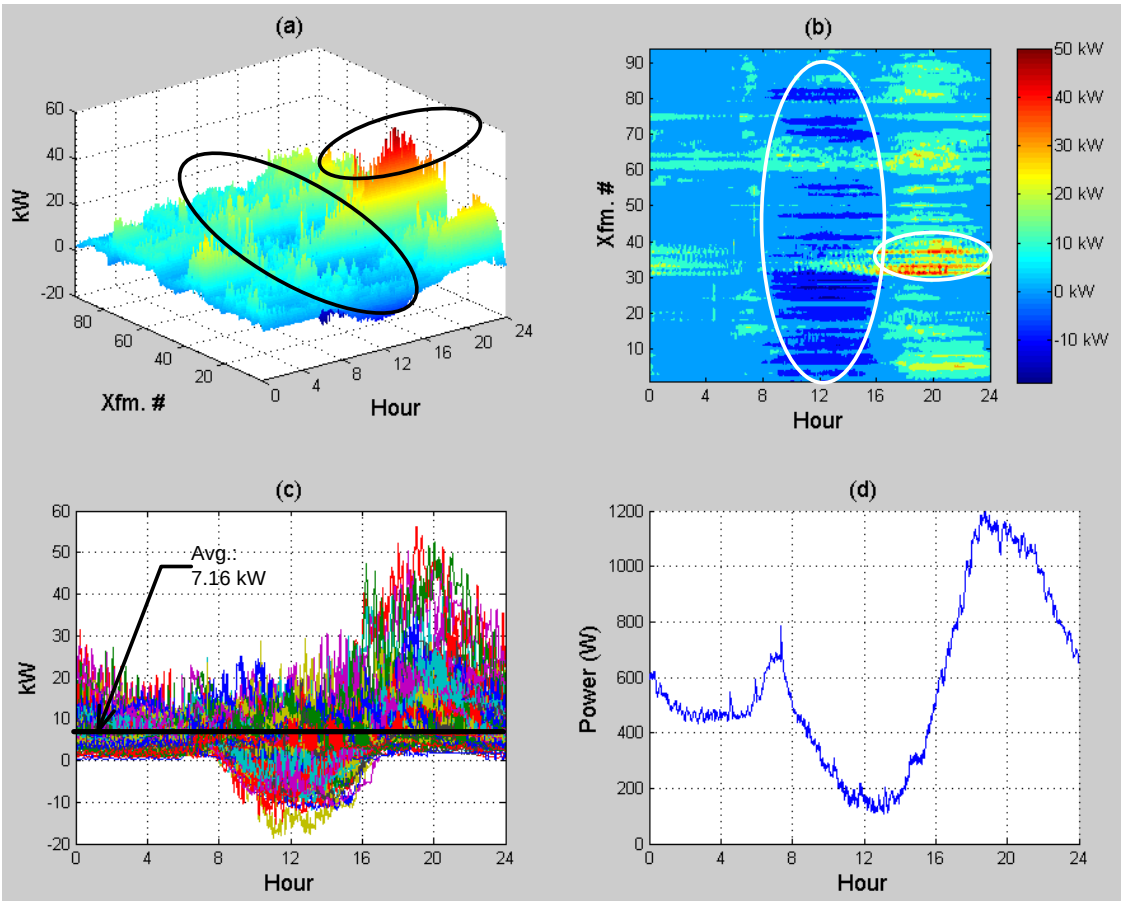

Figure 31: Real power through all distribution transformers

Figure 31(b) highlights times when transformers experience reverse flows. Referring to the darker blue regions (vertical circle), it is inferred that reverse flows occur on many transformers between 8 AM and 4 PM. These flows are aligned with diurnal PV output, but vary by transformer. The horizontal circle shows some transformers loaded at ~40 kW. These transformers correspond to T31B2,50 through T37B2,100 and show that, although loaded higher in comparison to other transformers and other times of day, they nonetheless operate below capacity. The dominant color on this contour plot is cyan, which suggests that the typical transformer usage at Mueller is about 7 kW.

Figure 31(c) shows the load profiles for all transformers, which includes residential load, PV generation, and EV charging. It is evident from this view that several transformers act as step-up transformers due to the excess PV generation. This excess power flows back into the grid and is consumed by neighboring transformers on the same phase. As shown by the solid line, the average transformer load (for 94 transformers over 24 hours) is about 7 kW.

Figure 31(d) depicts the aggregate transformer load; that is, the load-sum of all 94 distribution transformers as seen from the lateral service entrance. This load includes the residential load, PV generation, and EV charging from all transformers. As expected, peak consumptions occur during breakfast and dinner times. Interestingly, these peaks are separated by a significantly low diurnal demand when PVs are mostly active. This low demand is a direct result of having a high concentration of PVs on the same service lateral.

Transformer Percent Utilization

Although Fig. 31 shows the direction of real power flow through each transformer, it does not convey transformer-utilization information. Figure 32, on the other hand, shows the utilization (in %-kVA) of each transformer.

Figure 32(a) reveals that although some transformers are about 90% utilized, they do not experience sustained loads at these levels. Instead, this loading condition is intermittent. It should be noted that the diurnal %-utilization accounts for the PV real power throughput in the reverse direction (if any) and the reactive power demanded by the residences.

Figure 32(b) shows the duration of the high-load conditions and confirms that this loading is intermittent. The dominant color in this view is dark blue, which indicates that most of the time the transformers operate between 10-30% of their rated capacity.

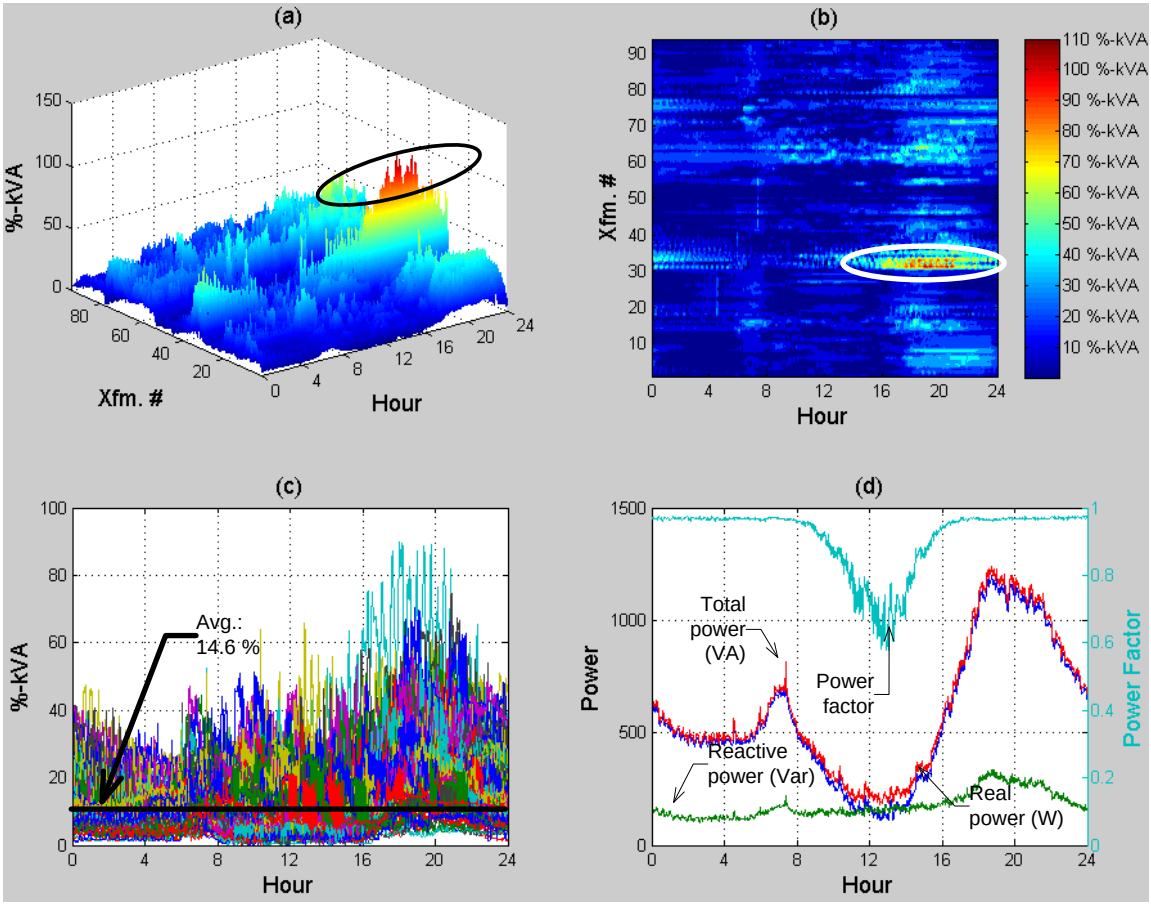

Figure 32: Percent-utilization of all distribution transformers

Figure 32(c) conveys the load profiles (VA) of all transformers. The average transformer consumption over the 24-hour period analyzed in this work is 14.6%. This percent-utilization is consistent with the surface level in view (a) and dominant color in view (b). Additionally, this view also shows that there is an uncorrelated transformer

load. It should be noted that this view is different from Fig. 31(c) in that transformer utilization, in %-VA, is always positive.

Figure 32(d) shows the aggregate transformer throughput (W, Var, and VA) as seen from the lateral service entrance. This power throughput includes transformer losses, residential load, PV generation, and EV charging. This figure shows a trace for power factor against the right-side axis. The power factor trace shows poor diurnal power conditions due to excess PV generation in this community. It should be acknowledged that this poor power factor condition is not a byproduct of high reactive load, but instead a byproduct of a significant decrease in real power demand consumed. Between 11 AM and 2 PM, the utility supplies nearly the same amount of reactive power as it does real power. During these times, the utility experiences power factor conditions as low as ~0.6. This power factor condition, however, is only observed from the lateral service entrance and is not necessarily the case as seen from the feeder head or substation transformer.

Transformer Loss of Life

The proliferation of distributed, controlled power electronic sources is impacting the lifetime of utility-owned assets. Residential PV generation is a sensible approach for delivering clean and renewable power, and provides several widely-recognized benefits. A non-traditional benefit is the savings associated with the potential deferment of distribution transformer upgrades, as PV installations in most commonly found configurations can reduce transformer loading during peak conditions. This benefit is investigated herein via the collected data from Mueller.

The increased deployment of residential distributed generation (e.g., PV systems) has stimulated a substantial amount of research on their interactions with the electric grid, which is already influencing discussions to modify IEEE Standard 1547 and, thus, the

control requirements for grid-tied PV inverters. These systems have been recognized for offering a variety of benefits in utility applications in addition to their energy and capacity values. Prior studies have considered the relationship between distribution transformer aging and the impact from rooftop PV arrays [93-95], electric vehicles [96, 97], or a combination of both [98], albeit the studies are subject to deterministic and stochastic methods for constructing the domestic daily load profiles. Instead, this work utilizes *real* electrical data from Mueller in order to assess the effects of distributed generation on distribution transformer aging.

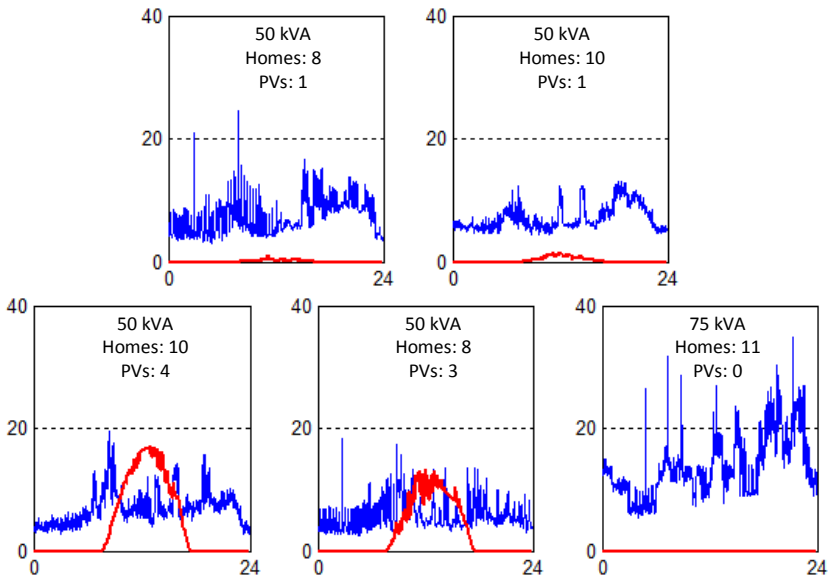

Figure 33: Typical daily load profile (blue trace) and PV generation (red trace) of 5 randomly selected transformers. (Vertical axis: Power [kW]; horizontal axis: Time [Hour].)

The collected data is used in conjunction with the computer model introduced previously. A total of 94 single-phase pad-mount distribution transformers ranging between 25, 50, 75, 100, and 167 kVA are present at Mueller. The number of houses each

transformer serves ranges between 1 and 12, where the number of PV-bearing houses ranges between 0 and 6. Typical power profiles ascribed to the transformers are observed in Fig. 33, where it is discernable that PV power generation at unity power factor as required by IEEE Standard 1547 may exceed the load in some cases.

The IEC 60076-7 [99] thermal model was used to estimate the top-oil and hot-spot temperatures, with and without the interconnection of PV sources. The computer model along with the recorded data was used to predict the loss of life for each of the 94 transformers. The top-oil and hot-spot temperatures for all transformers, with and without PV contributions, are shown in Fig. 34.

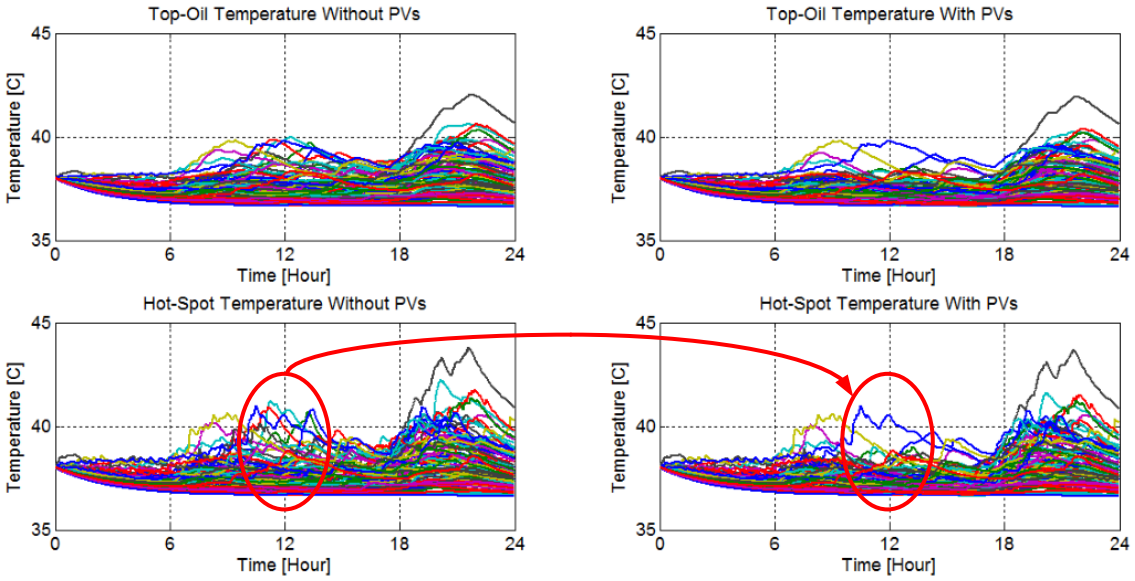

Figure 34: Effect of PVs on top-oil and hot-spot temperatures. (Encircled: diurnal rise reduction).

The temperatures above reveal that the transformers under study are relatively lightly loaded because normal loss of life for operation is rated at a hot-spot temperature of 110^{o} C for 24 hours [100]. The fact that the transformers are lightly loaded explains the minimal difference between top-oil and hot-spot temperatures. Moreover, it is observed that the diurnal temperature rise of the transformers (encircled area) is reduced as a result of normally configured systems with balanced PV generation and load, thus suggesting that in normal configurations PVs lead to increased transformer lifetime. This increase in lifetime would theoretically (and later proven evident) be more significant should the transformers be subject to heavier loading.

Histograms (Fig. 35, top) are used to analyze the contribution of PVs on transformer life for a 24-hour period. The loss of life, in percent, is shown for the cases with and without PV generation, and the ratio between the two is normalized and also shown. The histogram reveals that the normalized loss of life (bottom subplot) tends to be < 1, which means that transformer life is generally *improved* with the presence of PV generation and in most commonly found load configurations. Referring to the pie chart (Fig. 35, bottom), it is apparent that the majority of transformers are affected positively by PV generation, and about a third of them are not affected at all. One transformer is affected negatively, due to an uncommonly found combination of light loading and the presence of substantial PV assets at the transformer.

It is befitting to consider scenarios in which the distribution transformers are subject to heavier loading. An increase in loading is accomplished by de-rating the transformers, where the per-unit current used for the thermal model is obtained as

$$I_{p.u.} = \frac{I_{amps}}{\left(\frac{kVA}{D}\right)/kV} \tag{36}$$

where D is the de-rating factor (i.e., $D = 1$ represents actual loading, $D = 2$ represents 2 x loading, etc.).

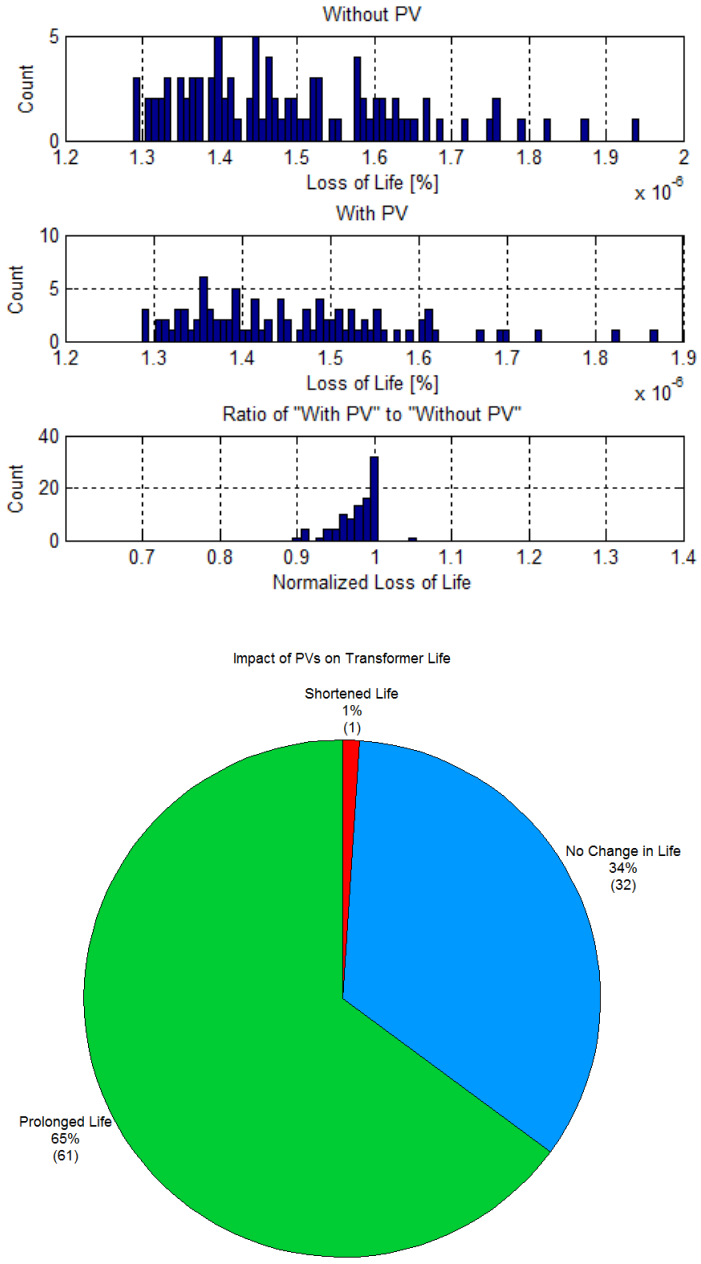

Figure 35: Impact of PVs on distribution transformer life

The top-oil and hot-spot temperatures, with and without PV contributions, are shown in Fig. 36 for the situation where transformer loading is increased by a factor of 3. This situation results in an accelerated aging rate due to higher hot-spot temperatures and also accounts for a more pronounced difference between top-oil and hot-spot temperatures. It is interesting to note that the sheer *impact* of the PVs in this case (conveyed in Fig. 37) is more prominent than in the previous case (Fig. 35). That is, the positively-affected transformers in the previous case are affected even more favorably in this case, whereas the far less numerous negatively-affected transformers in the previous case are affected more unfavorably in this case.

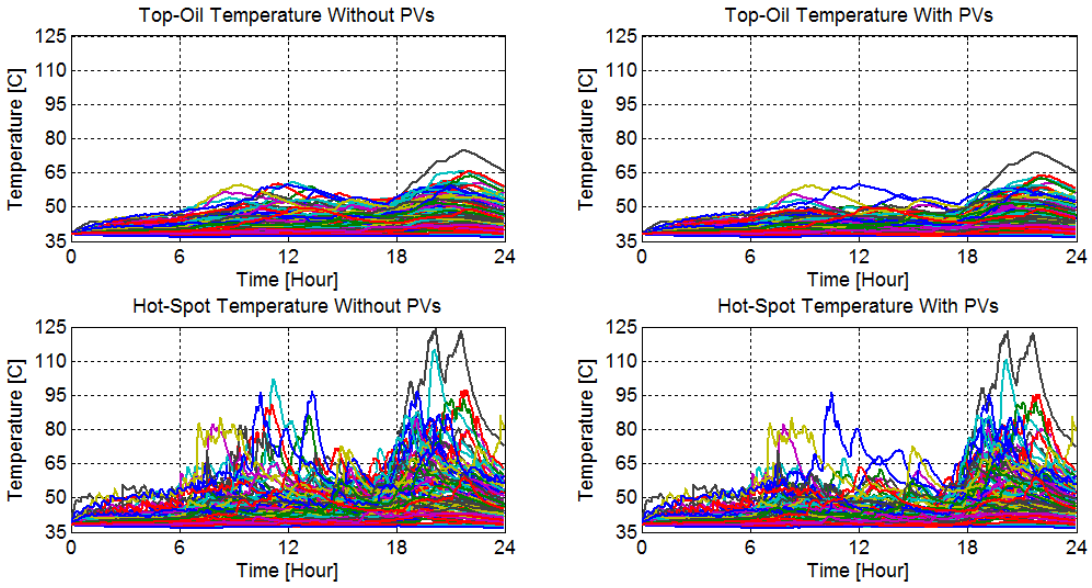

Figure 36: Effect of PVs on top-oil and hot-spot temperatures during 3x loading of transformers

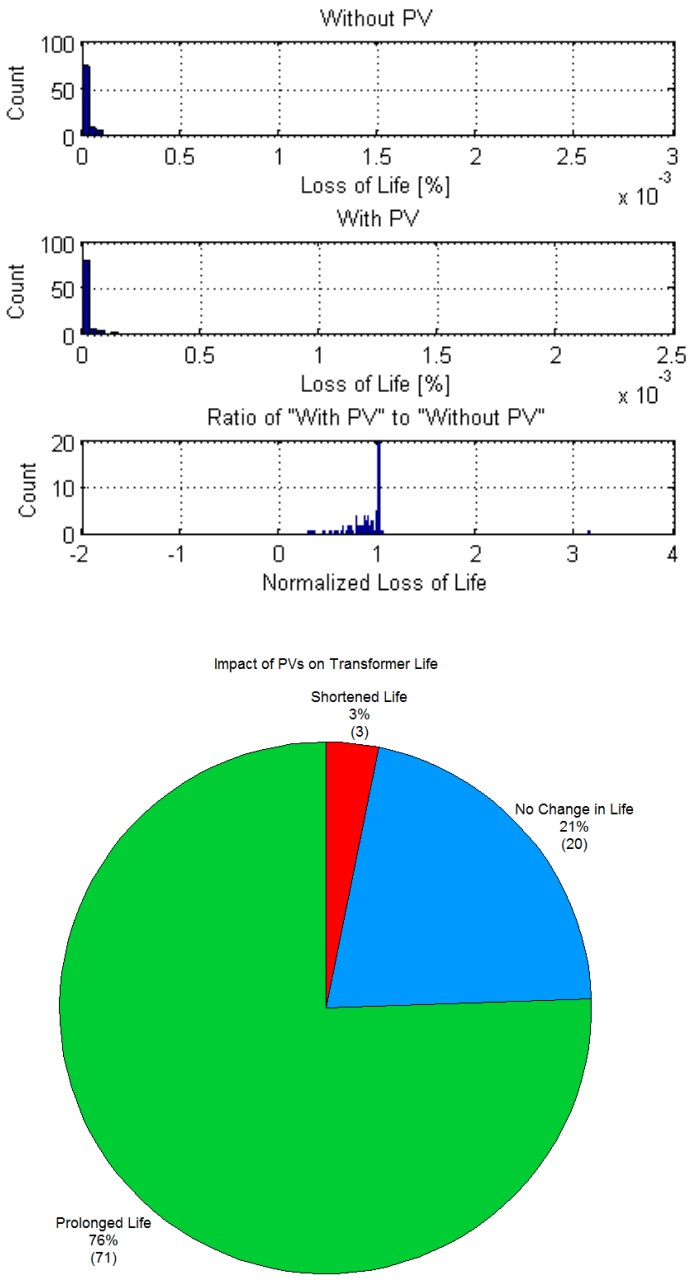

Figure 37: Impact of PVs on distribution transformer life during 3x loading of transformers

A similar trend is also observed in Fig. 38, where the normalized loss of life is compared against various degrees of transformer loading and various quantities of PV assets. It is apparent that as transformer loading increases, the normalized loss of life diverges further away from 1 (in both directions). In addition, the data points suggest that *too much* PV generation may be detrimental to transformer aging, and, rather, there exists an optimal PV number per transformer, which for this particular residential community tends to be 3 or 4. However, in the most commonly found cases in which PV systems are sized somewhat balanced with respect to the existing load, presence of grid-tied PV generation has a generally positive impact on transformer life.

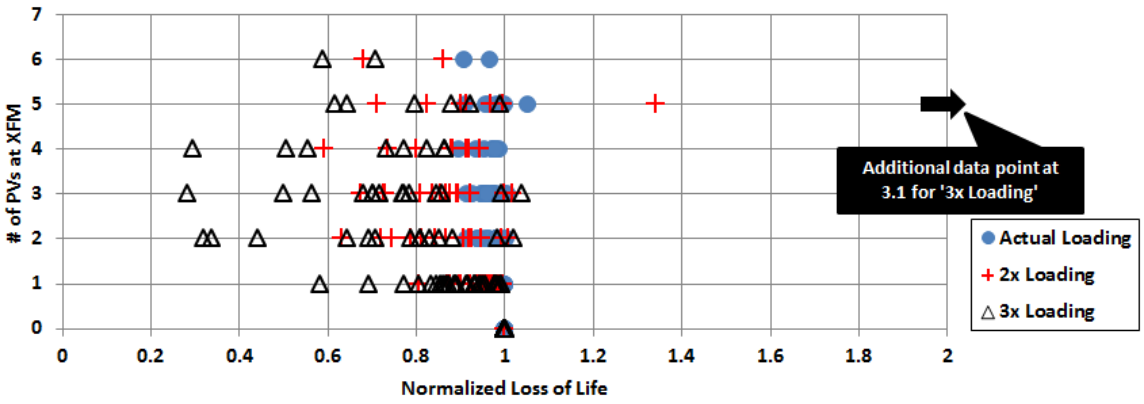

Figure 38: Loss of life as a function of transformer loading and PV quantity

LESSONS LEARNED

The use of recorded residential data not only elevates confidence in the results, but also avoids the need to develop computer models for mimicing uncorrelated residential load and daily PV fluctuations consistent with the city of interest. The efforts undertaken in this work reveal that Mueller's network-wide voltages, currents, and power flow profiles are close to what is observed by the local utility.

The distribution transformers at Mueller appear to be sized appropriately for meeting diverse EV charging levels and durations during the evening hours. Merit is given to the utility for their foresight to deploying 50 kVA transformers at this community in anticipation of high concentrations of emerging technologies.

Most of the electrical footprint observed in this work stemmed from PVs rather than from EVs. This footprint was perceived as reversed power flows in transformers, diurnal voltage swells (> 240 V), poor power factor conditions through transformers and at the lateral, a reduction of voltage unbalance, and reduced lateral power demand.

Furthermore, it is noted that the PV generation at Mueller does not leave the community; it is instead consumed by residents not having PVs. Presently, the utility buys the excess PV-generated power and sells it at the same price to other residents in the community. Although there is no profit in doing so, the distribution losses involved in buying and selling power closer to where it is needed rather than transmitting it over longer distances is less.

Bidirectional power flow in networks designed for flow in one direction (from source to load) improves distribution efficiency, provides voltage support, and reduces utility-side generation demand; however, it also introduces protection and control complexities not present before.

The voltage profiles at the transformers are within acceptable levels under the conditions studied. This result suggests that residents are not affected by the high concentration of PVs and EVs at this community and at this time.

The lateral power demand significantly changed with the inclusion of PVs and EVs. The most appreciable change was the reduction in real (active) power demand. After the inclusion of PVs, the power demand reduced from ~600 kW to ~200 kW. This

difference accounts for power that is no longer sold by the utility; instead, it is power produced locally by residents.

Local real (active) power generation results in poor power factor conditions experienced by the utility. It was shown that power factor can reduce to ~0.6. Nonetheless, reactive power demand is unchanged and its availability still the responsibility of the utility. That is, residences are allowed to rely on the utility to provide reactive power, but the utility cannot bill for this service. This has, at least, three implications: first, residences cannot become grid-independent unless they can overcome their dependence on reactive power; second, the utility must schedule generation to provide reactive power even though the utility cannot bill the customer for it; third, loads cannot be powered during grid outages—e.g., after natural disasters.

The voltage unbalance in Mueller is well within the acceptable range; furthermore, PV generation was shown to *re*-balance line voltages by decreasing the unbalanced demand. It was observed that phase *b* carries most of the residential load and also most PVs and EVs.

The impact of PV generation on distribution transformer life tends to be generally favorable. However, this observation is dependent on the PV-to-load ratio of distribution transformers in Mueller. Thus, too much PV generation may potentially be detrimental to transformer aging.

Chapter 6: Conclusion

This dissertation discussed the operational constraints, interconnection implications, and stability considerations associated with microgrids. Several key microgrid issues were raised, such as the operation of grid-tied inverters and the limitations imposed by IEEE Standard 1547. These limitations compromise frequency and voltage stability by constraining the operation of synchronous generators. German grid codes, recognized to be precedential because of their ability to aid with frequency and voltage support, were introduced as a contrast to US interconnection requirements.

Furthermore, the effect of line impedances was considered, and the respective power flow characteristics were derived. It was shown that microgrid lines can be described by a variety of X/R ratios that would affect the control and flow of active and reactive power. Grid stiffness was also studied, since it presents control challenges for grid-tied inverters due to the inverters' tendency to regulate the voltage at the point of common coupling.

In addition to raising awareness about key microgrid issues, the research addressed frequency and voltage stability challenges resulting from a combination of limited microgrid inertia and resistive line impedances. Specifically, a methodology for energy storage sizing was developed to aid with primary and secondary frequency control as well as with voltage regulation.

Additionally, this dissertation evaluated the impact of photovoltaic (PV) and electric vehicle (EV) integration on a residential community's electrical distribution system. The study used a computer model together with real consumption and generation data obtained from the individual residences in order to assess the state of the system and to perform various power system analyses such as: power profile assessments of

residential load, PV generation, and EV charging; transformer voltage profiles, including voltage sags/swells, voltage unbalance, and the effects of conservation voltage reduction; lateral power demand and power factor evaluation; as well as transformer net power flow, transformer percent utilization, and transformer loss of life. The findings from this study are valuable in helping to understand how neighborhoods such as Muller—where concentration of emerging technologies is high—would fare if retrofitted to a microgrid.

References

[1] J. E. Chadwick, "How a smarter grid could have prevented the 2003 U.S. cascading blackout," in *2013 IEEE Power and Energy Conference at Illinois (PECI)*, 2013, pp. 65-71.

[2] A. Kwasinski, P. Chapman, P. Krein, and W. Weaver, *Hurricane Katrina: Damage Assessment of Power Infrastructure for Distribution, Telecommunication, and Backup*: University of Illinois, Department of Electrical and Computer Engineering, 2006.

[3] G. S. Vassell, "Northeast Blackout of 1965," *IEEE Power Engineering Review,* vol. 11, p. 4, 1991.

[4] V. Venkatasubramanian and Y. Li, "Analysis of 1996 Western American electric blackouts," *Bulk Power System Dynamics and Control-VI, Cortina d'Ampezzo, Italy,* 2004.

[5] G. Pepermans, J. Driesen, D. Haeseldonckx, R. Belmans, and W. D'haeseleer, "Distributed generation: definition, benefits and issues," *Energy policy,* vol. 33, pp. 787-798, 2005.

[6] D. Lineweber and S. McNulty, *The cost of power disturbances to industrial & digital economy companies*: EPRI, 2001.

[7] U.S. Department of Energy, "The potential benefits of distributed generation and the rate-related issues that may impede its expansion," ed: Report Pursuant to Section, 1817.

[8] A. Kwasinski, V. Krishnamurthy, S. Junseok, and R. Sharma, "Availability Evaluation of Micro-Grids for Resistant Power Supply During Natural Disasters," *IEEE Transactions on Smart Grid,* vol. 3, pp. 2007-2018, 2012.

[9] S. Van Broekhoven, N. Judson, S. Nguyen, and W. Ross, "Microgrid Study: Energy Security for DoD Installations," DTIC Document 2012.

[10] M. Shahidehpour and M. Khodayar, "Cutting Campus Energy Costs with Hierarchical Control: The Economical and Reliable Operation of a Microgrid," *IEEE Electrification Magazine,* vol. 1, pp. 40-56, 2013.

[11] A. Kwasinski, "Technology Planning for Electric Power Supply in Critical Events Considering a Bulk Grid, Backup Power Plants, and Micro-Grids," *IEEE Systems Journal,* vol. 4, pp. 167-178, 2010.

[12] A. Kwasinski, "Technological assessment of distributed generation systems operation during extreme events," in *2012 3rd IEEE International Symposium on Power Electronics for Distributed Generation Systems (PEDG)*, 2012, pp. 534-541.

[13] A. Kwasinski, W. W. Weaver, P. L. Chapman, and P. T. Krein, "Telecommunications Power Plant Damage Assessment Caused by Hurricane Katrina - Site Survey and Follow-Up Results," in *28th Annual International Telecommunications Energy Conference*, 2006, pp. 1-8.

[14] Y. Yue, W. Lei, S. Weiwei, and J. Zhihui, "Collaborative control of microgrid for emergency response and disaster relief," in *International Conference on Sustainable Power Generation and Supply*, 2009, pp. 1-5.
[15] K. Hirose, J. Reilly, and H. Irie, "The sendai microgrid operational experience in the aftermath of the tohoku earthquake: a case study," *New Energy and Industrial Technology Development Organization,* vol. 308, 2013.
[16] IEEE Std. 1547, "IEEE Standard for Interconnecting Distributed Resources With Electric Power Systems," 2003.
[17] M. Braun, "Reactive Power supplied by PV Inverters–Cost-Benefit-Analysis," in *22nd European Photovoltaic Solar Energy Conference (EU PVSEC 2007), Milan (Italy)*, 2007.
[18] A. Cagnano, E. De Tuglie, M. Liserre, and R. A. Mastromauro, "Online Optimal Reactive Power Control Strategy of PV Inverters," *IEEE Transactions on Industrial Electronics,* vol. 58, pp. 4549-4558, 2011.
[19] Y. Ruifeng and T. K. Saha, "Investigation of Voltage Stability for Residential Customers Due to High Photovoltaic Penetrations," *IEEE Transactions on Power Systems,* vol. 27, pp. 651-662, 2012.
[20] P. M. S. Carvalho, P. F. Correia, and L. A. F. Ferreira, "Distributed Reactive Power Generation Control for Voltage Rise Mitigation in Distribution Networks," *IEEE Transactions on Power Systems,* vol. 23, pp. 766-772, 2008.
[21] E. Demirok, G. Casado, x, P. lez, K. H. B. Frederiksen, D. Sera*, et al.*, "Local Reactive Power Control Methods for Overvoltage Prevention of Distributed Solar Inverters in Low-Voltage Grids," *IEEE Journal of Photovoltaics,* vol. 1, pp. 174-182, 2011.
[22] W. Bartels, F. Ehlers, K. Heidenreich, R. Huttner, H. Kuhn, T. Meyer*, et al.*, "Generating plants connected to the medium-voltage network," *Technical Guideline of BDEW,* 2008.
[23] V. V. d. E. E. Informationstechnik, "eV: VDE-AR-N 4105: 2011-08: Power generation systems connected to the low-voltage distribution network Technical minimum requirements for the connection to and parallel operation with low-voltage distribution networks," *English translation of the VDE application rule VDEAR-N-4105*.
[24] T. Beach, A. Kozinda, and V. Rao, "Advanced Inverters for Distributed PV: Latent Opportunities for Localized Reactive Power Compensation," *Cal x Clean Coalition Energy C226,* 2013.
[25] E. A. Man, *Control of Grid Connected PV Systems with Grid Support Functions*: GlobeEdit, 2014.
[26] P. Esslinger and R. Witzmann, "Evaluation of reactive power control concepts for PV inverters in low-voltage grids," in *Integration of Renewables into the Distribution Grid, CIRED 2012 Workshop*, 2012, pp. 1-4.
[27] M. C. Chandorkar and D. M. Divan, "Decentralized operation of distributed UPS systems," in *Proceedings of the 1996 International Conference on Power*

Electronics, Drives and Energy Systems for Industrial Growth, 1996, pp. 565-571.

[28] J. M. Guerrero, J. C. Vasquez, J. Matas, V. de, x00F, L. G. a*, et al.*, "Hierarchical Control of Droop-Controlled AC and DC Microgrids—A General Approach Toward Standardization," *IEEE Transactions on Industrial Electronics,* vol. 58, pp. 158-172, 2011.

[29] J. W. Simpson-Porco, F. Dorfler, F. Bullo, Q. Shafiee, and J. M. Guerrero, "Stability, power sharing, and distributed secondary control in droop-controlled microgrids," in *2013 IEEE International Conference on Smart Grid Communications (SmartGridComm)*, 2013, pp. 672-677.

[30] F. Katiraei and M. R. Iravani, "Power Management Strategies for a Microgrid With Multiple Distributed Generation Units," *IEEE Transactions on Power Systems,* vol. 21, pp. 1821-1831, 2006.

[31] M. N. Marwali, J. Jin-Woo, and A. Keyhani, "Control of distributed generation systems - Part II: Load sharing control," *IEEE Transactions on Power Electronics,* vol. 19, pp. 1551-1561, 2004.

[32] A. Mehrizi-Sani and R. Iravani, "Potential-Function Based Control of a Microgrid in Islanded and Grid-Connected Modes," *IEEE Transactions on Power Systems,* vol. 25, pp. 1883-1891, 2010.

[33] M. Prodanovic and T. C. Green, "High-Quality Power Generation Through Distributed Control of a Power Park Microgrid," *IEEE Transactions on Industrial Electronics,* vol. 53, pp. 1471-1482, 2006.

[34] A. M. Bollman, "An experimental study of frequency droop control in a low-inertia microgrid," M.S. Thesis, Electrical and Computer Engineering, University of Illinois, 2009.

[35] J. M. Guerrero, M. Chandorkar, T. Lee, and P. C. Loh, "Advanced Control Architectures for Intelligent Microgrids—Part I: Decentralized and Hierarchical Control," *IEEE Transactions on Industrial Electronics,* vol. 60, pp. 1254-1262, 2013.

[36] T. L. Vandoorn, B. Meersman, J. D. M. De Kooning, and L. Vandevelde, "Analogy Between Conventional Grid Control and Islanded Microgrid Control Based on a Global DC-Link Voltage Droop," *IEEE Transactions on Power Delivery,* vol. 27, pp. 1405-1414, 2012.

[37] T. Kawabata and S. Higashino, "Parallel operation of voltage source inverters," *IEEE Transactions on Industry Applications,* vol. 24, pp. 281-287, 1988.

[38] A. Engler and N. Soultanis, "Droop control in LV-grids," in *2005 International Conference on Future Power Systems*, 2005.

[39] Westinghouse Electric Corporation, *Electrical transmission and distribution reference book*: Westinghouse Electric Corporation, 1943.

[40] A. Kwasinski, "Telecommunications outside plant power infrastructure: Past performance and technological alternatives for improved resilience to hurricanes," in *31st International Telecommunications Energy Conference INTELEC 2009*, 2009, pp. 1-6.

[41] A. Kwasinski, "Effects of notable natural disasters from 2005 to 2011 on telecommunications infrastructure: Lessons from on-site damage assessments," in *2011 IEEE 33rd International Telecommunications Energy Conference (INTELEC)*, 2011, pp. 1-9.

[42] A. Kwasinski, "Effects of Hurricanes Isaac and Sandy on Data and Communications Power Infrastructure," in *Proceedings of 2013 35th International Telecommunications Energy Conference 'Smart Power and Efficiency' (INTELEC)*, 2013, pp. 1-6.

[43] A. Kwasinski, W. W. Weaver, P. L. Chapman, and P. T. Krein, "Telecommunications Power Plant Damage Assessment for Hurricane Katrina--Site Survey and Follow-Up Results," *IEEE Systems Journal,* vol. 3, pp. 277-287, 2009.

[44] D. Tapscott and A. D. Williams. (September 2010) The Smart Grid is Wikinomics on a Macro Scale. *Harvard Business Review*.

[45] G. Barbose, N. Darghouth, S. Weaver, and R. Wiser, "Tracking the Sun VI: An Historical Summary of the Installed Price of Photovoltaics in the United States from 1998 to 2012," Lawrence Berkeley National Laboratory, Berkeley2013.

[46] A. Ulbig, T. S. Borsche, and G. Andersson, "Impact of low rotational inertia on power system stability and operation," in *Proceedings of the 19th IFAC World Congress*, 2014, pp. 7290-7297.

[47] M. P. Antonishen, H. Hai Yue, T. K. A. Brekken, A. von Jouanne, A. Yokochi, D. A. Halamay*, et al.*, "A methodology to enable wind farm participation in automatic generation control using energy storage devices," in *Power and Energy Society General Meeting, 2012 IEEE*, 2012, pp. 1-7.

[48] C. Hill and C. Dongmei, "Development of a real-time testing environment for battery energy storage systems in renewable energy applications," in *2011 IEEE Power and Energy Society General Meeting*, 2011, pp. 1-8.

[49] C. A. Hill, M. C. Such, C. Dongmei, J. Gonzalez, and W. M. Grady, "Battery Energy Storage for Enabling Integration of Distributed Solar Power Generation," *IEEE Transactions on Smart Grid,* vol. 3, pp. 850-857, 2012.

[50] M. K. Hossain and M. H. Ali, "Small scale energy storage for power fluctuation minimization with spatially diverged PV plants," in *2013 Proceedings of IEEE Southeastcon*, 2013, pp. 1-6.

[51] A. Faghih, M. Roozbehani, and M. A. Dahleh, "Optimal utilization of storage and the induced price elasticity of demand in the presence of ramp constraints," in *2011 50th IEEE Conference on Decision and Control and European Control Conference (CDC-ECC)*, 2011, pp. 842-847.

[52] P. Harsha and M. Dahleh, "Optimal sizing of energy storage for efficient integration of renewable energy," in *2011 50th IEEE Conference on Decision and Control and European Control Conference (CDC-ECC)*, 2011, pp. 5813-5819.

[53] Y. Wang, X. Lin, and M. Pedram, "Accurate Component Model Based Optimal Control for Energy Storage Systems in Households with Photovoltaic Modules," in *2013 IEEE Green Technologies Conference*, 2013, pp. 28-34.

[54] Y. Wang, X. Lin, M. Pedram, S. Park, and N. Chang, "Optimal control of a grid-connected hybrid electrical energy storage system for homes," in *2013 Design, Automation & Test in Europe Conference & Exhibition (DATE)*, 2013, pp. 881-886.

[55] T. Borsche, A. Ulbig, M. Koller, and G. Andersson, "Power and energy capacity requirements of storages providing frequency control reserves," in *Power and Energy Society General Meeting (PES), 2013 IEEE*, 2013, pp. 1-5.

[56] T. K. A. Brekken, A. Yokochi, A. Von Jouanne, Z. Z. Yen, H. M. Hapke, and D. A. Halamay, "Optimal Energy Storage Sizing and Control for Wind Power Applications," *IEEE Transactions on Sustainable Energy,* vol. 2, pp. 69-77, 2011.

[57] W. Z. Chen, Q. B. Li, L. Shi, Y. Luo, D. D. Zhan, N. Shi*, et al.*, "Energy storage sizing for dispatchability of wind farm," in *2012 11th International Conference on Environment and Electrical Engineering (EEEIC)*, 2012, pp. 382-387.

[58] Q. Zian, M. Liserre, F. Blaabjerg, and L. Poh Chiang, "Reliability-oriented energy storage sizing in wind power systems," in *2014 International Power Electronics Conference (IPEC-Hiroshima 2014 - ECCE-ASIA)*, 2014, pp. 857-862.

[59] D. I. Doukas, K. Papastergiou, P. Bakas, and A. Marinopoulos, "Energy storage sizing for large scale PV power plants base-load operation - comparative study & results," in *2012 38th IEEE Photovoltaic Specialists Conference (PVSC)*, 2012, pp. 000570-000574.

[60] Z. Y. Gao, P. Wang, L. Bertling, and J. H. Wang, "Sizing of energy storage for power systems with wind farms based on reliability cost and worth analysis," in *2011 IEEE Power and Energy Society General Meeting*, 2011, pp. 1-7.

[61] P. Harsha and M. Dahleh, "Optimal Management and Sizing of Energy Storage Under Dynamic Pricing for the Efficient Integration of Renewable Energy," *IEEE Transactions on Power Systems,* vol. PP, pp. 1-18, 2014.

[62] J. Braid, "Conceptual design of a liquid-based variable inertia flywheel for microgrid applications," in *2014 IEEE International Energy Conference (ENERGYCON)*, 2014, pp. 1291-1296.

[63] R. Crispo and T. K. A. Brekken, "A motor-generator and supercapacitor based system for microgrid frequency stabilization," in *2013 1st IEEE Conference on Technologies for Sustainability (SusTech)*, 2013, pp. 162-166.

[64] F. A. Inthamoussou, J. Pegueroles-Queralt, and F. D. Bianchi, "Control of a Supercapacitor Energy Storage System for Microgrid Applications," *IEEE Transactions on Energy Conversion,* vol. 28, pp. 690-697, 2013.

[65] I. Serban and C. Marinescu, "Control Strategy of Three-Phase Battery Energy Storage Systems for Frequency Support in Microgrids and with Uninterrupted Supply of Local Loads," *IEEE Transactions on Power Electronics,* vol. 29, pp. 5010-5020, 2014.

[66] C. Marinescu and I. Serban, "Analysis of frequency stability in a residential autonomous microgrid based on a wind turbine and a Microhydro power plant," in *IEEE Power Electronics and Machines in Wind Applications*, 2009, pp. 1-5.

[67] J. A. Peças Lopes, S. A. Polenz, C. L. Moreira, and R. Cherkaoui, "Identification of control and management strategies for LV unbalanced microgrids with plugged-in electric vehicles," *Electric Power Systems Research,* vol. 80, pp. 898-906, 8// 2010.
[68] F. Katiraei, R. Iravani, N. Hatziargyriou, and A. Dimeas, "Microgrids management," *IEEE Power and Energy Magazine,* vol. 6, pp. 54-65, 2008.
[69] J. A. Peças Lopes, C. L. Moreira, and A. G. Madureira, "Defining control strategies for MicroGrids islanded operation," *IEEE Transactions on Power Systems,* vol. 21, pp. 916-924, 2006.
[70] S. Sharma, H. Shun-Hsien, and N. D. R. Sarma, "System Inertial Frequency Response estimation and impact of renewable resources in ERCOT interconnection," in *2011 IEEE Power and Energy Society General Meeting*, 2011, pp. 1-6.
[71] P. Tielens and D. Van Hertem, "Grid Inertia and Frequency Control in Power Systems with High Penetration of Renewables," *Young Researchers Symposium in Electrical Power Engineering,* vol. 6, April 2012.
[72] W. B. Gish, "Small Induction Generator and Synchronous Generator Constants for DSG Isolation Studies," *IEEE Transactions on Power Delivery,* vol. 1, pp. 231-239, 1986.
[73] F. M. Uriarte, A. Toliyat, A. Kwasinski, and R. E. Hebner, "Consumer-data approach to assess the effect of residential grid-tied photovoltaic systems and electric vehicles on distribution transformers," in *2014 IEEE 5th International Symposium on Power Electronics for Distributed Generation Systems (PEDG)*, 2014, pp. 1-8.
[74] N. Mohan *et al*, "Review of basic electrical and magnetic circuit concepts," in *Power Electronics*, 2nd ed New York: Wiley, 1995, p. 43.
[75] J. R. Aguero, P. Chongfuangprinya, S. Shengnan, X. Le, F. Jahanbakhsh, and H. L. Willis, "Integration of Plug-in Electric Vehicles and distributed energy resources on power distribution systems," in *2012 IEEE International Electric Vehicle Conference (IEVC)*, 2012, pp. 1-7.
[76] G. Kerber and R. Witzmann, "Loading capacity of standard oil transformers on photovoltaic load profiles," in *World Renewable Energy Congress (WRECX)*, 2008, pp. 1198-1203.
[77] J. C. Whitaker, *AC power systems handbook*, 3rd ed. Boca Raton, FL: CRC/Taylor & Francis, 2007.
[78] H. Jimenez, H. Calleja, R. González, J. Huacuz, and J. Lagunas, "The impact of photovoltaic systems on distribution transformer: a case study," *Energy conversion and management,* vol. 47, pp. 311-321, 2006.
[79] A. Toliyat, A. Kwasinski, and F. M. Uriarte, "Effects of high penetration levels of residential photovoltaic generation: Observations from field data," in *2012 International Conference on Renewable Energy Research and Applications (ICRERA)*, 2012, pp. 1-6.

[80] A. Omole, "Voltage stability impact of grid-tied photovoltaic systems utilizing dynamic reactive power control," Dissertation, Department of Electrical Engineering, University of South Florida, 2010.
[81] P. Kundur, *Power System Stability Analysis*, 5th ed.: McGraw-Hill, 1994.
[82] S. Shengnan, M. Pipattanasomporn, and S. Rahman, "Demand Response as a Load Shaping Tool in an Intelligent Grid With Electric Vehicles," *IEEE Transactions on Smart Grid,* vol. 2, pp. 624-631, 2011.
[83] S. Shengnan, M. Pipattanasomporn, and S. Rahman, "Grid Integration of Electric Vehicles and Demand Response With Customer Choice," *IEEE Transactions on Smart Grid,* vol. 3, pp. 543-550, 2012.
[84] ANSI C84.1-2006, "American National Standard for Electric Power Systems and Equipment—Voltage Ratings (60 Hertz)."
[85] J. G. De Steese, J. E. Englin, and R. D. Sands, "Conservation Voltage Reduction Potential In The Pacific Northwest," in *Proceedings of the 25th Intersociety Energy Conversion Engineering Conference*, 1990, pp. 43-47.
[86] J. G. De Steese, S. B. Merrick, and B. W. Kennedy, "Estimating methodology for a large regional application of conservation voltage reduction," *IEEE Transactions on Power Systems,* vol. 5, pp. 862-870, 1990.
[87] B. W. Kennedy and R. H. Fletcher, "Conservation voltage reduction (CVR) at Snohomish County PUD," *IEEE Transactions on Power Systems,* vol. 6, pp. 986-998, 1991.
[88] D. Kirshner, "Implementation of conservation voltage reduction at Commonwealth Edison," *IEEE Transactions on Power Systems,* vol. 5, pp. 1178-1182, 1990.
[89] D. Kirshner and P. Giorsetto, "Statistical Test of Energy Saving Due to Voltage Reduction," *IEEE Transactions on Power Apparatus and Systems,* vol. PAS-103, pp. 1205-1210, 1984.
[90] C. A. McCarthy and J. Josken, "Applying capacitors to maximize benefits of conservation voltage reduction," in *Rural Electric Power Conference*, 2003, pp. C4-1-C4-5.
[91] R. Singh, F. Tuffner, J. Fuller, and K. Schneider, "Effects of distributed energy resources on conservation voltage reduction (CVR)," in *2011 IEEE Power and Energy Society General Meeting*, 2011, pp. 1-7.
[92] J. H. Harlow, *Electric Power Transformer Engineering*, 3rd ed. Florida: CRC Press, 2012.
[93] M. M. El-Gasseir, M. A. Sayer, K. P. Alteneder, G. A. McCulla, and J. Bigger, "Enhancing transformer dynamic rating through grid application of photovoltaic arrays," in *Twenty Third IEEE Photovoltaic Specialists Conference*, 1993, pp. 1279-1284.
[94] D. Martin, S. Goodwin, O. Krause, and T. Saha, "The effect of PV on transformer ageing: University of Queensland's experience," in *2014 Australasian Universities Power Engineering Conference (AUPEC)*, 2014, pp. 1-6.

[95] H. Pezeshki, P. J. Wolfs, and G. Ledwich, "Impact of High PV Penetration on Distribution Transformer Insulation Life," *IEEE Transactions on Power Delivery,* vol. 29, pp. 1212-1220, 2014.
[96] G. Qiuming, S. Midlam-Mohler, V. Marano, and G. Rizzoni, "Study of PEV Charging on Residential Distribution Transformer Life," *IEEE Transactions on Smart Grid,* vol. 3, pp. 404-412, 2012.
[97] H. Turker, S. Bacha, D. Chatroux, and A. Hably, "Low-Voltage Transformer Loss-of-Life Assessments for a High Penetration of Plug-In Hybrid Electric Vehicles (PHEVs)," *IEEE Transactions on Power Delivery,* vol. 27, pp. 1323-1331, 2012.
[98] T. J. Geiles and S. Islam, "Impact of PEV charging and rooftop PV penetration on distribution transformer life," in *2013 IEEE Power and Energy Society General Meeting (PES)*, 2013, pp. 1-5.
[99] IEC Std. 60076-7, "IEC Loading Guide for Oil Immersed Power Transformers," 2005.
[100] IEEE Std. C57.91-1995, "IEEE Guide for Loading Mineral Oil Immersed Transformers," 1995.

Vita

Amir Toliyat received his B.S. and M.S. degrees, both in electrical engineering, from Texas A&M University and The University of Texas at Austin, respectively. His past industry experience includes working as a Facilities Engineer for Chevron Energy Technology Company (ETC) in Houston, Texas, where he spent a summer with the Machinery and Electrical Power Systems (MEPS) team. Mr. Toliyat is presently employed at Electric Power Engineers, Inc. as a Power Systems Engineer II.

Email: toliyat@utexas.edu

This dissertation was typed by the author.